

540477

**Analysis Report
AP-111
Culebra Water Level Monitoring Network Design**

**(AP-111: Analysis Plan for Optimization and Minimization of the
Culebra Monitoring Network for the WIPP)**

Task Number 1.4.1.1

Report Date: October 28th, 2004

Author:



Sean A. McKenna
Geohydrology Department (6115)

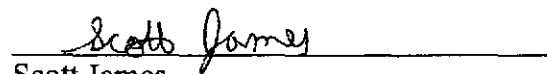
Date: 10/28/04

Technical Review:



Rick Beauheim
Repository Performance Department (6822)

Date: 11/3/04



Scott James
Geohydrology Department (6115)

Date: 11/1/04

QA Review:



Mario J. Chavez
Carlsbad Programs Group (6820)

Date: 11/3/04

Management Review



Mark Rigali
Manager, Repository Performance Department (6822)

Date: 11/3/04

WIPP:1.4.1.1:TD:QA-L:DRP1:Culebra Water Level Monitoring Network Design

Information Only

Acknowledgements

The author is indebted to David Hart for his work on the calibration of the transmissivity fields and development and testing of the **vlsap** software, Arun Wahi for his work on local gradient estimators and Dave Rudeen and Amy Gilkey for their work on testing the local gradient estimator approaches.

Table of Contents

Acknowledgements.....	2
Table of Contents.....	3
List of Figures.....	5
List of Tables.....	8
1.0 Introduction.....	9
1.0 Introduction.....	9
1.1 Background.....	9
1.2 Purpose.....	10
1.3 Outline.....	10
1.4 Calculation Domain.....	12
1.5 Observed Data.....	13
2.0 Geostatistical Variance Reduction.....	17
2.1 Trend Fitting and Residual Calculations.....	17
2.2 Variogram Calculation and Modeling.....	20
2.3 Kriging.....	21
2.4 Estimation Variance Calculations.....	23
2.5 Calculation Details.....	29
3.0 Local Gradient Estimation.....	31
3.1 Background.....	31
3.2 Estimation of the Gradient.....	33
3.3 Local Gradient Estimator Error Analysis.....	34
3.3.1 Relative Measurement Error.....	34
3.3.2 Estimator Shape and Gradient Orientation.....	35
3.3.3 Choosing Acceptable Three-Point Estimators.....	40
3.4 Application 1: Monitoring Temporal Changes.....	41
3.5 Application 2: Long-Term Monitoring Network Design.....	50
3.5.1 Removal of Existing Monitoring Wells.....	50
3.5.2 Addition of New Monitoring Wells.....	54
3.6 Local Gradient Estimation Summary.....	55
3.7 Assumption of Homogeneity.....	57
3.8 Calculation Details.....	66
4.0 Spatial Sensitivity-Based Monitoring.....	68
4.1 Background.....	68
4.2 Derivative-Based Sensitivity Coefficients.....	69
4.3 Sampling-Based Sensitivity Coefficients.....	69
4.4 Application to Culebra Calculations.....	71
4.5 Results.....	75
4.6 Summary.....	80
4.7 Calculation Details.....	80
5.0 Combining Monitoring Approaches.....	82
5.1 Results.....	83
5.2 Summary.....	91
5.3 Calculation Details.....	91

6.0	Additional Monitoring Wells.....	93
6.1	Expanded Data Set.....	93
6.2	Variogram Calculation.....	93
6.3	Estimation Variance Calculations.....	95
6.4	Addition of New Monitoring Wells Using Three-Point Estimators.....	96
6.5	Combining Monitoring Approaches.....	97
6.6	Calculation Details.....	102
7.0	Conclusions.....	103
7.1	Summary of Calculations.....	103
7.2	Reexamination of Monitoring Goals.....	106
8.0	References.....	108

List of Figures

Figure 1. Locations of the monitoring wells with head observations (Table 3) used in this study.	15
Figure 2. Scatterplot showing the relationship between the heads measured in August 2000 and August 2003.	16
Figure 3. Scatterplot showing the relationship between the measured heads and those estimated with the best-fit plane for the August 2003 sampling period.....	19
Figure 4. Experimental omnidirectional variogram (points) and Gaussian model variogram (line) fit to it.	21
Figure 5. Kriging variance (m^2) for estimation of the residuals between the estimated and measured heads.	24
Figure 6. Box and whisker plots of the distribution of the ratio of the estimated to true magnitude (left graph) and the estimated to true orientation (right graph) as a function of the RHME. The boxes define the 25 th and 75 th percentiles. The whiskers define the 5 th and 95 th percentiles and the circles beyond the ends of the whiskers are individual results. All distributions contain 5000 results.	35
Figure 7. Shapes of the different triangles examined in this study. Each triangle is defined by the size of the two equal angles and the base to height ratio. All triangles have the same area.	37
Figure 8. The 95 th percentile error values for gradient magnitude (upper graph) and orientation (lower graph) for the 41 degree estimator as a function of groundwater flow direction and RHME. The different levels of RHME are shown in the legend.....	38
Figure 9. The median 95 th percentile errors in magnitude (upper graph) and orientation (lower graph) as a function of estimator shape and RHME. The different RHME values are shown by the different symbols and the legend. Each median value is calculated across the results for the 24 different flow directions for a given estimator shape (e.g., the results in Figure 8).	39
Figure 10. Estimated magnitude of the hydraulic gradient across all three-point estimators as a function of estimator size for the 2000 and 2003 head data. The upper graph shows all estimators, the middle graph shows results for those estimators meeting the shape criterion, and the lower graph shows results for estimators meeting the shape and RHME criteria....	43
Figure 11. Estimated orientation of the hydraulic gradient across all three-point estimators as a function of estimator size for the 2000 and 2003 head data. The upper graph shows results for all estimators, the middle graph shows results for those estimators meeting the shape criterion, and the lower graph shows results for estimators meeting the shape and RHME criteria.	45
Figure 12. Estimated orientation of the hydraulic gradient as a function of estimated magnitude for the 2000 and 2003 head data. The upper graph shows results for all estimators, the middle graph shows results for those estimators meeting the shape criterion, and the lower graph shows results for estimators meeting the shape and RHME criteria.	47
Figure 13. Cumulative distributions of absolute differences of the magnitude (top) and orientation (bottom) of the hydraulic gradient between the 2000 and 2003 measurements as calculated using the three sets of local gradient estimators.	49
Figure 14. Number of acceptable local gradient estimators for a single new well placed at any location within the domain. The current network produces 1879 acceptable local gradient	

estimators. The black crosses show the existing 30-well monitoring network. The contour is 25 estimators and the contour levels correspond to the levels identified in the color scale.

.....	55
Figure 15. Polar coordinate plots comparing the estimated orientation and magnitude of the hydraulic gradient based on field measurements (left image) and model-generated heads (right image). The magnitudes are shown on log10 scale.	58
Figure 16. Example of discretizing a large triangle defined by wells with a number of smaller isosceles triangles defined using the underlying 100-meter grid spacing.....	59
Figure 17. Estimates of the magnitude of the hydraulic gradient from the observed head values at the wells and as unweighted (top) and flux-weighted averages (bottom) of the grid triangles within each well triangle. The results are sorted by the mean values (not shown) and are arranged from high to low magnitude and then each result is assigned an index for plotting.	60
Figure 18. Estimates of the orientation of the hydraulic gradient from the observed heads values at the wells and as unweighted (top) and flux-weighted (bottom) averages of the grid triangles within each well triangle. The different estimators are assigned indices for plotting.	61
Figure 19. Difference between the magnitude of the hydraulic gradient as estimated from the well observations and the median average estimated magnitude across 100 realizations as a function of estimator size. The results of the unweighted averaging are shown in the top image and the flux-weighted averaging results are shown in the lower image.	63
Figure 20. Difference between the orientation of the hydraulic gradient as estimated from the well observations and the median average estimated orientation across 100 realizations as a function of estimator size. The results of the unweighted averaging are shown in the top image and the flux-weighted averaging results are shown in the lower image.	64
Figure 21. Comparison of sampling-based sensitivity coefficients to the median of the analytically calculated sensitivity coefficients. Both sets of coefficients define the sensitivity to the overall model calibration with respect to the estimated head at 99 different locations.	72
Figure 22. Sampling-based sensitivity of the overall steady-state and transient calibration to the simulated head values.	74
Figure 23. Sampling-based sensitivity of the overall steady-state and transient calibration to the calibrated transmissivity values.	75
Figure 24. Sampling-based sensitivity of travel time to the WIPP boundary with respect to simulated heads.	77
Figure 25. Sampling-based sensitivity of the travel time to the WIPP boundary with respect to calibrated transmissivity values.	78
Figure 26. Locations of the 100 flowpaths along which travel time to the boundary of the WIPP site is calculated.	79
Figure 27. Rescaled [0,1] estimation variance map. The wells in the historic monitoring network are shown as plus signs; the new well locations are shown by diamonds.	85
Figure 28. Rescaled [0,1] number of acceptable three-point estimators map. The wells in the historic monitoring network are shown as plus signs; the new well locations are shown by diamonds.	86
Figure 29. Rescaled [0,1] absolute value of the sensitivity of the travel time to the WIPP boundary with respect to the estimated head at every point. The wells in the historic	

monitoring network are shown as plus signs; the new well locations are shown by diamonds.....	87
Figure 30. Rescaled [0,1] absolute value of the sensitivity of the travel time to the WIPP boundary with respect to the transmissivity at every point. The wells in the historic monitoring network are shown as plus signs; the new well locations are shown by diamonds.....	88
Figure 31. Combined score values map including estimation variance, number of three-point estimators and sensitivity of travel time to head. The wells in the historic monitoring network are shown as plus signs; the new well locations are shown by diamonds.....	89
Figure 32. Combined score values map including estimation variance, number of three-point estimators and sensitivity of travel time to transmissivity. The wells in the historic monitoring network are shown as plus signs; the new well locations are shown by diamonds.....	90
Figure 33. Experimental omnidirectional variogram (points) and analytical model variogram (line) fit to it. This variogram is for the actual measured and estimated heads.....	94
Figure 34. Kriging variance (m^2) for estimation of the heads using the 38-well monitoring network.....	95
Figure 35. Number of acceptable local gradient estimators for a single new well placed at any location within the domain. Addition of a single well to the original 30-well network produces, on average, 2100 estimators.....	97
Figure 36. Rescaled [0,1] estimation variance map. The wells in the expanded monitoring network and the WIPP site boundary are shown.....	98
Figure 37. Rescaled [0,1] number of acceptable three-point estimators map. The wells in the expanded monitoring network and the WIPP site boundary are shown.....	99
Figure 38. Combined score values map including estimation variance, number of three-point estimators and sensitivity of travel time to head. The wells in the expanded monitoring network are shown as plus signs.....	100
Figure 39. Combined score values map including estimation variance, number of three-point estimators and sensitivity of travel time to transmissivity. The wells in the expanded monitoring network are shown as plus signs.....	102

List of Tables

Table 1. The UTM (NAD27) coordinates of the corners of the numerical model domain.....	12
Table 2. The UTM (NAD27) coordinates of the WIPP site boundary.	13
Table 3. Results of Monthly Head Monitoring Program for August 2000 and 2003.	14
Table 4. August 2003 head data and estimates of the head data from a best-fit plane. The residuals in the right column are calculated as the estimated – measured head.	18
Table 5. Results of estimation variance changes for the removal of one well from the current head-monitoring network.....	26
Table 6. Results of estimation variance changes for the removal of one well from the head-monitoring network after wells WIPP-12 and WIPP-22 have been removed.	27
Table 7. Results of estimation variance changes for the removal of one well from the head-monitoring network after wells WIPP-12, WIPP-22, H-12, and P-17 have been removed.	28
Table 8. Magnitude and orientation of the regional gradient as determined through the best-fit plane technique for the 2000 and 2003 time periods.	41
Table 9. Decrease in the number of acceptable local gradient estimators due to removing one well at a time from the full (30-well) monitoring network.....	51
Table 10. Decrease in the number of acceptable local gradient estimators due to removing one well at a time from the 28-well monitoring network where WIPP-12 and WIPP-22 have already been removed.	52
Table 11. Decrease in the number of acceptable local gradient estimators due to removing one well at a time from the 26-well monitoring network where WIPP-12, WIPP-22, H-12, and P-17 have already been removed.	53
Table 12. Names and location of new monitoring network wells.....	83
Table 13. New monitoring wells and estimated heads.....	93
Table 14. Relative importance of existing wells in the monitoring network. X = least important, O = most important. Blank boxes indicate moderate importance. Wells removed for the starting case are denoted “NA”.....	105

1.0 Introduction

This document presents the methods, supporting data, and results of calculations done in support of Culebra head and hydraulic gradient network monitoring design. Three different approaches to monitoring network design are examined and results for the Culebra are obtained for each. These results include optimal locations for additional monitoring wells and identification of wells in the current monitoring network that could be removed with minimal effect on meeting the monitoring objectives. The three different sets of results are then combined into a final set of maps indicating areas for the installation of new monitoring wells. Additionally, several wells in the existing network could be removed with minimal effect on the ability of the monitoring network to predict heads at unmonitored locations and to detect changes in the hydraulic gradient.

1.1 Background

The Waste Isolation Pilot Plant (WIPP) is located in southeastern New Mexico and has been developed by the U.S. Department of Energy (DOE) for the geologic (deep underground) disposal of transuranic (TRU) waste. Containment of TRU waste at the WIPP is regulated by the U.S. Environmental Protection Agency (EPA) according to the regulations set forth at Title 40 of the Code of Federal Regulations, Parts 191 and 194. The DOE demonstrates compliance with the containment requirements in the regulations by means of a performance assessment (PA), which estimates releases from the repository for the regulatory period of 10,000 years after closure.

In October 1996, DOE submitted the Compliance Certification Application (CCA; U.S. DOE, 1996) to the EPA, which included the results of extensive PA analyses and modeling. After an extensive review, in May 1998 the EPA certified that the WIPP met the criteria in the regulations and was approved for disposal of transuranic waste. The first shipment of waste arrived at the site in March 1999.

The results of the PA conducted for the CCA were subsequently summarized in a Sandia National Laboratories (SNL) report (Helton et al., 1998) and in refereed journal articles (see Helton and Marietta, 2000).

Groundwater-monitoring and modeling activities at the WIPP are an integral part of the DOE's broader requirements to demonstrate that WIPP operations are performed in a manner that ensures protection of the environment, the health and safety of workers and the public, proper characterization of the disposal system, and compliance of the WIPP with applicable regulations. Continued compliance with regulations must be demonstrated every five years during the operational phase of the WIPP. The monitoring requirements apply not only for the current operational phase (~35 years), but extend through the post-closure phase of the facility to meet applicable regulations. Because of these long-term requirements, DOE's Carlsbad Field Office (CBFO) has developed a *Strategic Plan For Groundwater Monitoring at the Waste Isolation Pilot Plant* (DOE, 2003) that describes: relevant regulatory (EPA and NMED) drivers; the current groundwater-monitoring network and how it has evolved over time; current groundwater program elements; strategies for maintaining compliance; methods for implementing the strategies; and roles and responsibilities of monitoring program participants.

1.2 Purpose

The purpose of these calculations is to identify optimal locations for new Culebra monitoring wells. Additionally, it is necessary to examine the current monitoring network to determine if redundant information with respect to the monitoring goals is being collected. If so, it may be possible to remove some of the existing wells from the network without compromising the ability of the network to predict heads at unmonitored locations or to detect changes in the magnitude and direction of the hydraulic gradient. The calculations herein will be focused on meeting the goals of:

1. The monitoring network must allow the determination of the direction and rate of groundwater flow across the WIPP site. This is a NMED and EPA requirement (NMAC, 2000 incorporating 40 CFR Part 194 §264.98(e) EPA, 1996);
2. The monitoring network must provide data needed to infer causes of changes in water levels that might be observed. This is an EPA requirement, 40 CFR Part 194, Subpart C §194.42 (EPA, 1996); and
3. The monitoring network must provide spatially distributed head data adequate to allow both defensible boundary conditions to be inferred for Culebra flow models and defensible calibration of those models (PA requirements).

The degree to which these objectives can be reduced to quantitative measures is evaluated as part of the work reported in this Analysis Report.

The optimized and minimized monitoring network will be created using available information including existing wells and up to date understanding of the hydrology of the Culebra. The optimization and minimization process must take the following factors into consideration:

1. Optimize around (i.e., preserve) existing locations of fiberglass-cased wells
2. Preserve existing locations of steel-cased wells where feasible to minimize pad/road construction, permitting, and survey costs
3. Identify existing well locations that are not needed
4. Known T variations and geologic boundaries
5. Where feasible, locate new wells in areas where questions have arisen concerning the geologic and/or hydrologic conceptual models
6. Where feasible, locate new wells in areas of high groundwater flow and/or particle travel time model sensitivity

1.3 Outline

This report documents the data, methods, and summary results of the work completed under Analysis Plan 111 (Beauheim and McKenna, 2003). The sections of this report and a brief description of each subsection are:

1.0 Introduction

- 1.1 Background: A brief background of the WIPP certification and recertification process
 - 1.2 Purpose: A concise statement of the purpose of this work
 - 1.3 Outline
 - 1.4 Calculation Domain: Definition of the spatial domain of the model and changes from the CRA model
 - 1.5 Observed Data: A description of the measured head and drawdown data used for the calibration of the base transmissivity fields and the references from which these measurements were obtained
- 2.0 Geostatistical Variance Reduction
- 2.1 Trend Fitting and Residual Calculations: A planar trend is fit to the 2000 and 2003 head data sets and residuals between the trend and the measurements are calculated
 - 2.2 Variogram Calculation and Modeling: Variograms of the residuals are calculated and modeled
 - 2.3 Kriging: The residuals are kriged to get estimates of residuals and estimation variance at all locations without wells
 - 2.4 Estimation Variance Calculations: The average estimation variance in the model domain and in the WIPP site is calculated
 - 2.5 Calculation Details: Details of the calculations, directory names and file names and locations are provided for the work done in this chapter
- 3.0 Local Gradient Estimation
- 3.1 Background: Literature review of previous work on local gradient estimation
 - 3.2 Estimation of the Gradient: The equations for three-point estimation
 - 3.3 Local Gradient Estimator Error Analysis: Summary of numerical analysis of the effects of measurement error on local gradient estimation
 - 3.3.1 Relative Measurement Error: The definition of the relative head measurement error
 - 3.3.2 Estimator Shape and Gradient Orientation: Summary of numerical experiments conducted to determine the effect of estimator shape and orientation on the accuracy of the estimates
 - 3.3.3 Choosing Acceptable Three-Point Estimators: Summary of the rules developed for necessary estimator shape and relative head measurement error to achieve accurate estimates
 - 3.4 Application 1: Monitoring Temporal Changes: Use of local gradient estimators to identify changes in the Culebra gradient from August 2000 to August 2003
 - 3.5 Application 2: Long-Term Monitoring Network Design: Use of local gradient estimators to optimize existing well removal and addition of wells to the network.
 - 3.5.1 Removal of Existing Monitoring Wells
 - 3.5.2 Addition of New Monitoring Wells
 - 3.6 Local Gradient Estimation Summary
 - 3.7 Assumption of Homogeneity: Discussion of numerical calculations done to examine the effects of assuming a homogeneous aquifer within each three-point estimator
 - 3.8 Calculation Details: Details of the calculations, directory names and file names and locations are provided for the work done in this chapter
- 4.0 Spatial Sensitivity-Based Monitoring

- 4.1 Background: Literature review on other efforts
- 4.2 Derivative-Based Sensitivity Coefficients: Definition of the more traditional derivative-based sensitivity coefficients
- 4.3 Sampling-Based Sensitivity Coefficients: Definition of sampling-based sensitivity coefficients
- 4.4 Application to Culebra Calculations: Comparison of derivative and sampling-based sensitivity coefficients
- 4.5 Results: Sensitivity of travel time to WIPP boundary with respect to head and transmissivity
- 4.6 Summary
- 4.7 Calculation Details: Details of the calculations, directory names and file names and locations are provided for the work done in this chapter

5.0 Combining Monitoring Approaches

- 5.1 Results: final maps of the sum of the rescaled maps of the different approaches
- 5.2 Summary
- 5.3 Calculation Details: Details of the calculations, directory names and file names and locations are provided for the work done in this chapter

6.0 Conclusions

7.0 References: Other work cited in this report

1.4 Calculation Domain

The spatial domain used for the different calculations in support of monitoring network design is the same as the model domain used in the stochastic inverse calibration of the Culebra T fields to steady-state and transient data (McKenna and Hart, 2003) for the CRA (DOE, 2004). This model domain is oriented with the compass directions and is 30.6 km in the north-south direction and 22.3 km in the east-west direction. The corners of the WIPP model domain are given in Table 1. These coordinates define the center of 100×100-m² model cells at the four corners of the model domain. All monitoring calculations that produce results on a spatial grid employ the same grid as used for the stochastic inverse calibrations.

Table 1. The UTM (NAD27) coordinates of the corners of the numerical model domain.

Domain Corner	X Coordinate (meters)	Y Coordinate (meters)
Northeast	624,000	3,597,100
Northwest	601,700	3,597,100
Southeast	624,000	3,566,500
Southwest	601,700	3,566,500

The WIPP land-withdrawal boundary, or the “WIPP site boundary”, is an approximately 6.4 X 6.4 km area near the center of the model domain. The boundary of the WIPP site is defined by the coordinates shown in Table 2. For the calculations described in this report, the coordinates

shown in Table 2 are used to determine different measures of the effectiveness of the monitoring network.

Table 2. The UTM (NAD27) coordinates of the WIPP site boundary.

Domain Corner	X Coordinate (meters)	Y Coordinate (meters)
Northeast	616,941	3,585,109
Northwest	610,495	3,585,068
Southeast	617,015	3,578,681
Southwest	610,567	3,578,623

1.5 Observed Data

The approaches developed in this report can be applied to any set of simultaneous head measurements. Additionally, the monitoring network optimization techniques developed herein can also be applied to sets of heads measured at different times and the differences in the results will provide an indication of changes in the heads and gradient over time. For comparison across different times, the wells in which the heads are measured must remain constant. To develop and demonstrate the monitoring network optimization approaches in this report, two different sets of heads measured in the same wells three years apart, August 2000 and August 2003, are employed.

The observation wells are taken from the current Culebra monitoring network. The wells used for this analysis are the intersection of the set of wells in which heads were observed in both August of 2000 (WTS, 2003) and August of 2003 (Jones, 2003). In two cases, H-9 and H-10, different wells on the same hydropad (~30 m apart) were monitored at the two different times. For these analyses, the two different wells on each hydropad are considered to be equivalent and are counted as a single well. Additionally, the WIPP-29 well was removed from the analysis because it is far enough west of the other wells that heads measured in WIPP-29 are not representative of the heads in the vicinity of the WIPP site. The final sets of 30 wells and the adjusted freshwater heads measured in those wells in both 2000 and 2003 used in the monitoring network analysis in this report are shown in Table 3.

Table 3. Results of Monthly Head Monitoring Program for August 2000 and 2003.

Integer ID	Well Name	X coordinate (m)	Y coordinate (m)	Adjusted 2000 Freshwater Head (m)	Adjusted 2003 Freshwater Head (m)	Difference 2003-2000 (meters)
1	AEC-7	621126	3589381	933.10	933.36	0.26
2	DOE-1	615203	3580333	915.42	916.49	1.07
3	ERDA-9	613696	3581958	921.56	922.25	0.69
4	H-2b2	612661	3581649	926.28	927.13	0.85
5	H-3b2	613701	3580906	917.28	917.93	0.66
6	H-4b	612380	3578483	915.90	915.66	-0.24
7	H-5b	616872	3584801	936.73	937.12	0.39
8	H-6b	610594	3585008	933.79	934.51	0.72
9	H-7b2	608117	3574620	913.64	913.59	-0.05
10	H-9b/c	613989	3568261	911.27	911.28	0.01
11	H-10b/c	622975	3572473	922.42	922.06	-0.36
12	H-11b4	615301	3579131	915.52	915.45	-0.06
13	H-12	617023	3575452	916.10	917.02	0.92
14	H-17	615718	3577513	917.38	917.99	0.61
15	H-19b0	614514	3580716	917.65	918.30	0.65
16	P-17	613926	3577466	913.46	913.79	0.33
17	WIPP-12	613710	3583524	935.30	935.82	0.52
18	WIPP-13	612644	3584247	935.29	935.18	-0.11
19	WIPP-19	613739	3582782	937.88	938.59	0.70
20	WIPP-21	613743	3582319	926.55	927.12	0.57
21	WIPP-22	613739	3582653	932.83	933.59	0.76
22	WIPP-25	606385	3584028	931.66	932.14	0.49
23	WIPP-26	604014	3581162	921.14	921.25	0.12
24	WIPP-30	613721	3589701	936.79	938.23	1.43
25	WQSP-1	612561	3583427	935.69	936.29	0.60
26	WQSP-2	613776	3583973	938.75	939.05	0.30
27	WQSP-3	614686	3583518	935.70	935.97	0.27
28	WQSP-4	614728	3580766	917.87	918.45	0.58
29	WQSP-5	613668	3580353	917.12	917.88	0.76
30	WQSP-6	612605	3580736	920.16	920.95	0.79

The locations of the monitoring wells in Table 3 with respect to the WIPP site are shown in Figure 1.

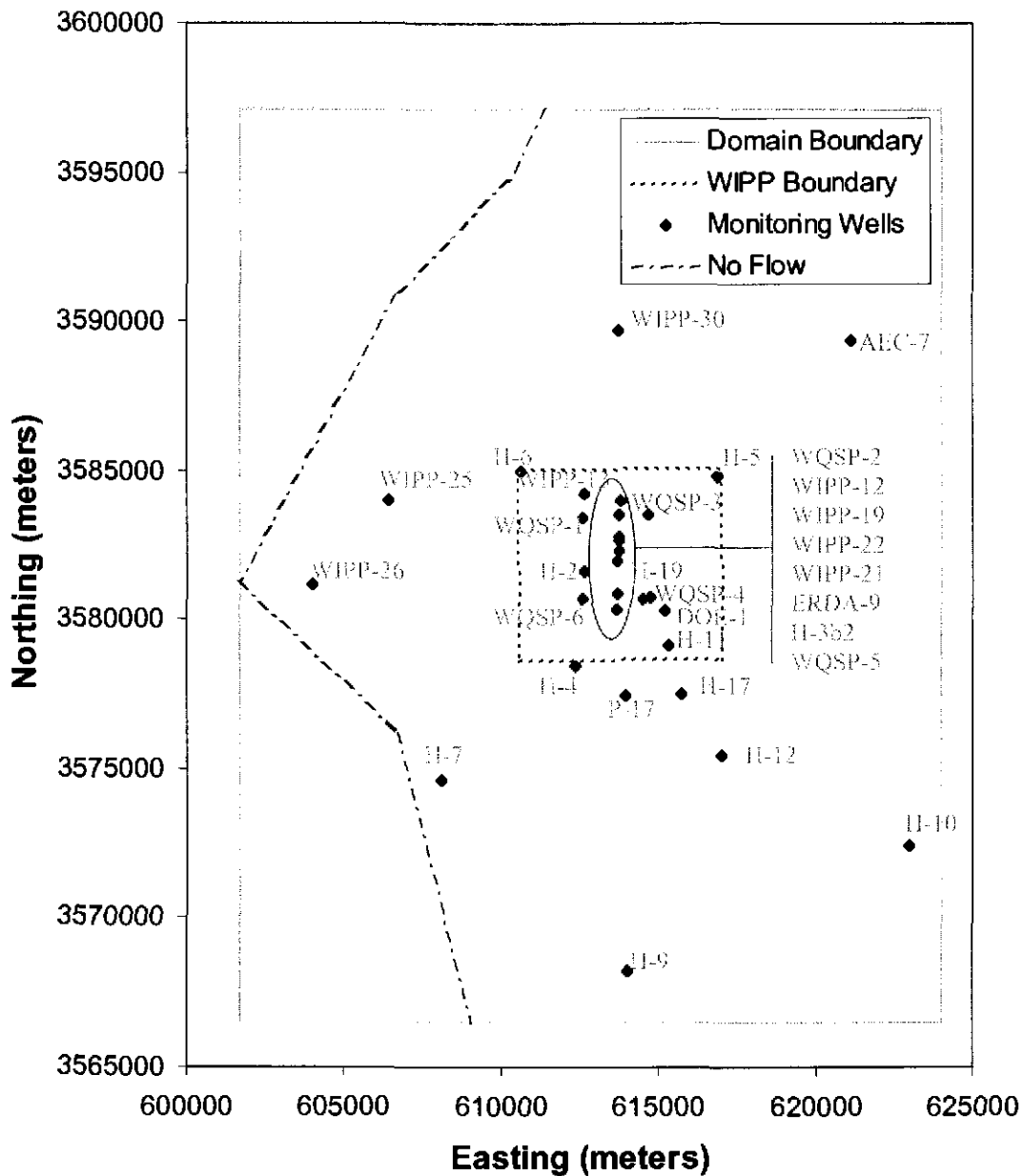


Figure 1. Locations of the monitoring wells with head observations (Table 3) used in this study.

In general, there has been a rise in head from 2000 to 2003 (positive values in the right column of Table 3), with a maximum rise of 1.43 meters in WIPP-30. The degree of change in the heads across the 3-year time period is shown as a scatterplot in Figure 2. Figure 2 shows that the rise in heads during this three-year time period has been fairly uniform and independent of the actual magnitude of the measured head.

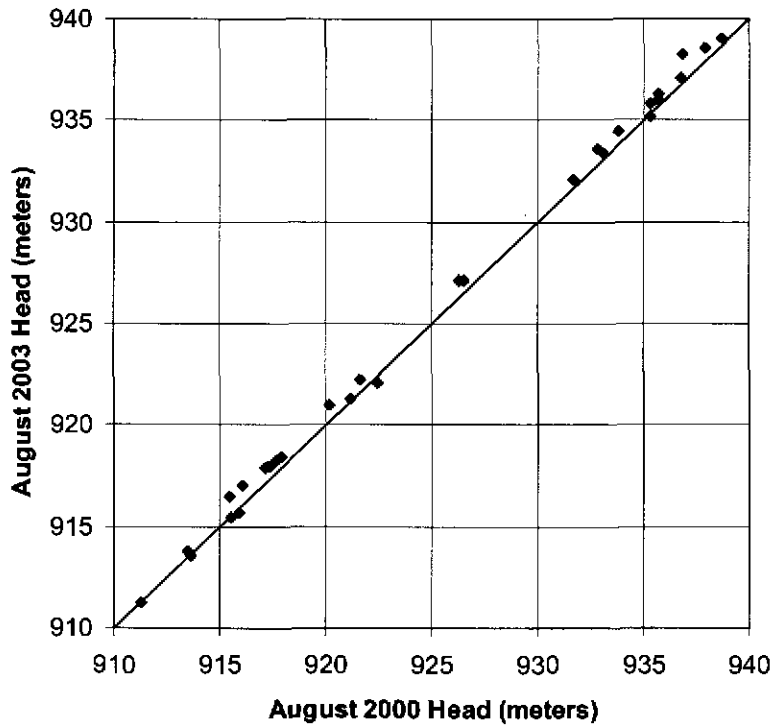


Figure 2. Scatterplot showing the relationship between the heads measured in August 2000 and August 2003.

In addition to the measured heads from August 2000 and August 2003, calculation results from the most recent stochastic inverse calibration of the Culebra transmissivity fields (McKenna and Hart, 2003) are also used. These results include the simulated head values and calibrated transmissivity values for each calibrated field. These files are stored on the lylin102 computational cluster in the subdirectories below: /h/WIPPcvs/trans/runs/. These results are used in the third approach, sensitivity-based, to long-term monitoring network design.

2.0 Geostatistical Variance Reduction

Geostatistics is the study and modeling of spatially correlated information and it has been used extensively over the past 30 years in areas including ore reserve estimation, contaminant mapping in soils and groundwater and modeling spatial variability of physical properties of aquifers and petroleum reservoirs. The geostatistical algorithm used for spatial estimation is kriging and, compared to other spatial interpolation algorithms, kriging is unique in that it produces both an estimate and a variance about that estimate at unsampled locations.

Previous studies (e.g., Rouhani, 1985) have used the kriging variance as a measure of the ability of a groundwater monitoring network to predict heads at locations where no wells exist. Groundwater monitoring network design can be optimized to reduce the kriging variance to a prescribed level at all locations or to minimize the maximum kriging variance. Calculation of the kriging variance can also be used to determine what wells to remove from an existing network such that the overall kriging variance has a minimal increase when those wells are removed. As an example, Tuckfield et al. (2001) used the kriging variance of contaminants in a plume to determine the redundancy of groundwater contaminant monitoring wells and targeted those wells with the highest redundancy for removal from the network. A major advantage of monitoring network design using kriging is that the kriging variance is not a direct function of the sample value at any single point and therefore changes in the kriging variance from the addition or removal of a well can be determined prior to adding or removing that well.

2.1 Trend Fitting and Residual Calculations

The more recent of the two sets of head observations, August 2003, are used for the geostatistical variance reduction analysis. A single best-fit planar gradient for these heads was calculated using the equation fitting tool in **SigmaPlot** (version 8.02). The equation for the best-fit plane to the August 2003 heads is:

$$Head(x, y) = Ax + By + C \quad (1)$$

The results of this equation fitting produced $A = 1.98E-04$, $B = 1.62E-03$ and $C = 5007.74$. With these parameter values, (1) fits the August 2003 heads with an R^2 of 0.60. Diagnostics regarding the equation fitting process are given in Appendix 1. This best-fit plane has a hydraulic gradient of $1.64E-03$ and a flow direction (negative of the mathematical gradient) of 173.04° counterclockwise from north, or -173.04° . Results of these calculations are stored in the spreadsheet *Trend_results.xls* on the CD-ROM as part of this analysis package (see the “Calculation Details” section). Residuals between the measured and estimated heads are calculated and shown in Table 4. The estimated and measured heads are compared graphically in Figure 3. Figure 3 shows that the planar fit to the heads has difficulty in estimating the highest and lowest measured heads.

Table 4. August 2003 head data and estimates of the head data from a best-fit plane. The residuals in the right column are calculated as the estimated – measured head.

Integer ID	Well Name	X coordinate (m)	Y coordinate (m)	Measured Head (m)	Estimated Head (m)	Residual (m)
1	AEC-7	621126	3589381	933.36	940.48	7.12
2	DOE-1	615203	3580333	916.49	924.62	8.13
3	ERDA-9	613696	3581958	922.25	926.96	4.71
4	H-2b2	612661	3581649	927.13	926.25	-0.88
5	H-3b2	613701	3580906	917.93	925.25	7.32
6	H-4b	612380	3578483	915.66	921.06	5.40
7	H-5b	616872	3584801	937.12	932.20	-4.92
8	H-6b	610594	3585008	934.51	931.29	-3.22
9	H-7b2	608117	3574620	913.59	913.95	0.36
10	H-9b/c	613989	3568261	911.28	904.79	-6.49
11	H-10b/c	622975	3572473	922.06	913.40	-8.66
12	H-11b4	615301	3579131	915.45	922.69	7.24
13	H-12	617023	3575452	917.02	917.06	0.04
14	H-17	615718	3577513	917.99	920.15	2.16
15	H-19b0	614514	3580716	918.30	925.11	6.81
16	P-17	613926	3577466	913.79	919.71	5.92
17	WIPP-12	613710	3583524	935.82	929.50	-6.32
18	WIPP-13	612644	3584247	935.18	930.47	-4.71
19	WIPP-19	613739	3582782	938.59	928.31	-10.28
20	WIPP-21	613743	3582319	927.12	927.55	0.43
21	WIPP-22	613739	3582653	933.59	928.10	-5.49
22	WIPP-25	606385	3584028	932.14	928.87	-3.27
23	WIPP-26	604014	3581162	921.25	923.75	2.50
24	WIPP-30	613721	3589701	938.23	939.53	1.30
25	WQSP-1	612561	3583427	936.29	929.12	-7.17
26	WQSP-2	613776	3583973	939.05	930.25	-8.80
27	WQSP-3	614686	3583518	935.97	929.69	-6.28
28	WQSP-4	614728	3580766	918.45	925.23	6.78
29	WQSP-5	613668	3580353	917.88	924.35	6.47
30	WQSP-6	612605	3580736	920.95	924.76	3.81

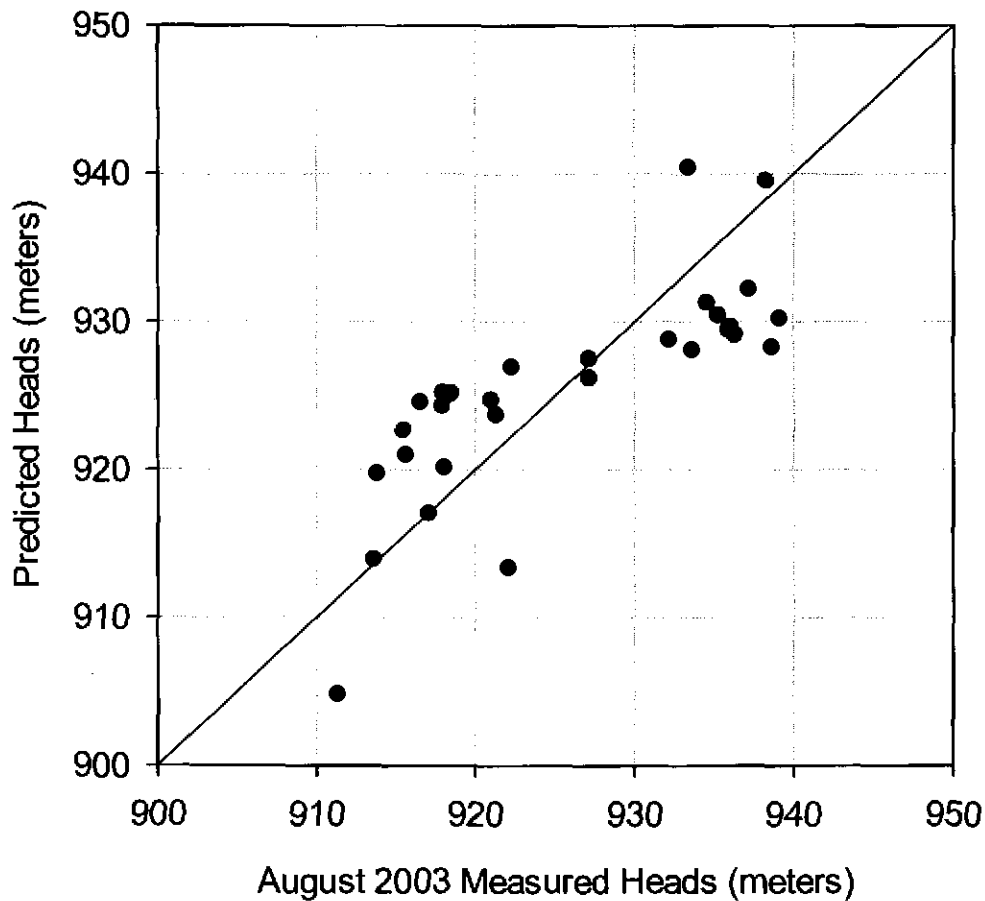


Figure 3. Scatterplot showing the relationship between the measured heads and those estimated with the best-fit plane for the August 2003 sampling period.

The residuals between the estimated and measured heads are used as the input data for the geostatistical analysis. The X, Y, measured head and residual values from the *Trend_results.xls* file are saved in *Aug_03_resid.dat* and a six line GeoEAS header is added to this file to allow for its use in the variogram and kriging calculations. The reason for using the head residuals in the geostatistical analysis is that the raw head measurements represent a strong trend in the data from high heads in the north to lower heads in the south. This type of trend is representative of a non-stationary mean in the data; however, geostatistical models have an inherent theoretical assumption of second-order (mean and variance) stationarity. Therefore, the head residuals represent the detrended head measurements and are suitable for geostatistical modeling.

2.2 Variogram Calculation and Modeling

The experimental variogram is calculated and then modeled using the commercial off-the-shelf **VarioWin** (version 2.21) software (Pannatier, 1996). The experimental variogram is calculated as:

$$\hat{\gamma}(\mathbf{h}) = \frac{1}{2N(\mathbf{h})} \sum_{i=1}^{N(\mathbf{h})} [z(\mathbf{u}_i) - z(\mathbf{u}_i + \mathbf{h})]^2 \quad (2)$$

where \mathbf{h} is the lag spacing, z are the residual values, $N(\mathbf{h})$ is the number of pairs of data points for a given lag spacing and \mathbf{u} is a vector of spatial coordinates (x, y) for the sample locations of each residual value. The values of the experimental variogram $\gamma(\mathbf{h})$, are plotted as a function of \mathbf{h} and a variogram model is fit to these data. Only a few variogram models are available that will produce a positive definite covariance matrix in the kriging equations and one of these, the Gaussian model, is chosen to fit the experimental variogram points. The equation of the Gaussian variogram model as implemented in **VarioWin** is:

$$\gamma(\mathbf{h}) = C \cdot \left\{ 1 - \exp\left[-\frac{(3\mathbf{h})^2}{a^2}\right] \right\} \quad (3)$$

where C is the sill and a is the range. The Gaussian model fit to the experimental variogram points is shown in Figure 4. This model has a nugget value of 13.0, a sill of 45.2 and a range of 9000 m. The numbers of data pairs that were used for the calculation of each point in the experimental variogram are also shown in Figure 4. The calculation of the experimental variogram was done by considering combinations of pairs of data points in all directions, an “omnidirectional calculation”. Due to the limited number of head data, 30, it was not possible to calculate directionally dependent variograms that might show anisotropy in the spatial correlation of the residuals. The Gaussian model fit to the experimental variogram in Figure 4 was constrained to reach a maximum at the covariance of the residual data set, 58.2 m², as shown by the horizontal dashed line in Figure 4. The experimental variogram points beyond the range of 9000 m and above the level of the covariance represent negative spatial correlation and are a result of the first-order trend surface fit to the measured heads not accounting for all variation in the head data. Higher order trend surfaces could be fit to the data, but the planar model is used here to be consistent with the calculations done for the local gradient estimates in the following section.

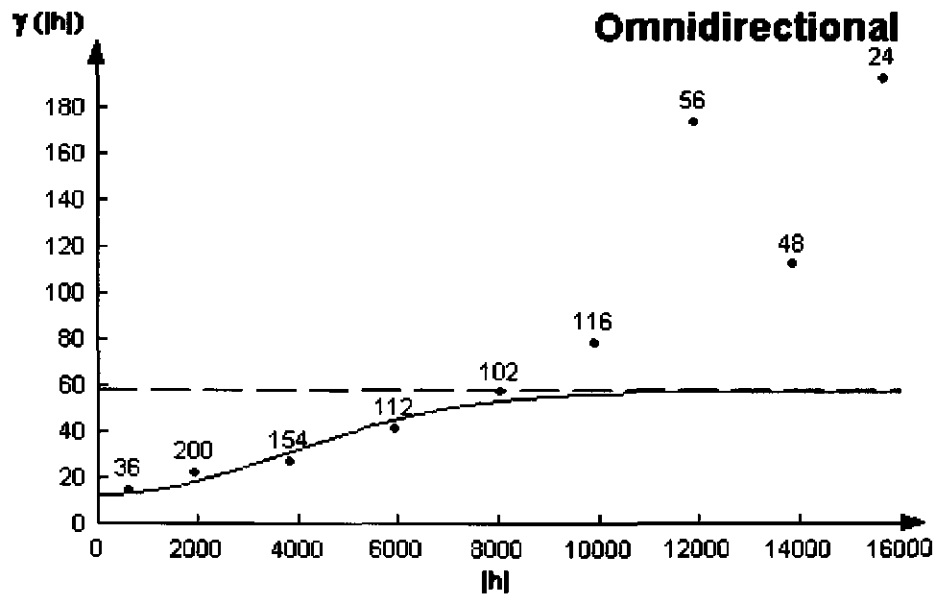


Figure 4. Experimental omnidirectional variogram (points) and Gaussian model variogram (line) fit to it.

2.3 Kriging

Kriging is a geostatistical algorithm for calculating spatial estimates of a measured property at unsampled locations. The kriging equations are formulated to provide an unbiased, minimum variance estimate of the property from a linear combination of the surrounding measured data. A distinct advantage of kriging over other spatial estimation algorithms is that in addition to the property estimates, kriging also provides a measure of the uncertainty about each estimate. The uncertainty measure is known as the kriging variance or the estimation variance. Details on the many variants of the kriging algorithm and its application can be found in Deutsch and Journel (1998), Goovaerts (1997), and Olea (1999) among others. For this work, we use ordinary kriging (OK) and the details of the OK algorithm are presented briefly.

Consider the problem of estimating the value of a continuous attribute, z , (e.g. head residual) at an unsampled location \mathbf{u} . The information available consists of measurements of z at n locations $\mathbf{u}_\alpha, z(\mathbf{u}_\alpha), \alpha = 1, 2, \dots, n$, as obtained at the monitoring wells. Kriging is a form of generalized least square regression and therefore all univariate kriging estimates are variants of the general linear regression estimate $z^*(\mathbf{u})$ defined as:

$$z^*(\mathbf{u}) - m(\mathbf{u}) = \sum_{\alpha_1=1}^{n(\mathbf{u})} \lambda_{\alpha_1}(\mathbf{u}) [z(\mathbf{u}_{\alpha_1}) - m(\mathbf{u}_{\alpha_1})] \quad (4)$$

where $\lambda_{\alpha 1}(\mathbf{u})$ is the weight assigned to the datum $z(\mathbf{u}_{\alpha 1})$ and $m(\mathbf{u})$ is the trend component of the spatially varying attribute. In practice, only the observations closest to \mathbf{u} being estimated are retained, that is the $n(\mathbf{u})$ data within a given neighborhood or window $W(\mathbf{u})$ centered on \mathbf{u} . If there is no trend in the data across the site, m is no longer a function of the spatial location \mathbf{u} but is now the global mean of the data set, then (4) defines the simple kriging, SK, estimator. In most practical applications of kriging, SK has proven to be overly restrictive and ordinary kriging is the preferred choice.

The most common kriging estimator is OK, which estimates the unsampled value $z(\mathbf{u})$ as a linear combination of neighboring observations without enforcing a global mean onto the estimate:

$$z_{OK}^*(\mathbf{u}) = \sum_{\alpha_1=1}^{n(\mathbf{u})} \lambda_{\alpha_1}^{OK}(\mathbf{u}) z(\mathbf{u}_{\alpha_1}) \quad (5)$$

OK weights λ_{α} are determined so as to minimize the error or estimation variance $\sigma^2(\mathbf{u}) = \text{Var}\{Z^*(\mathbf{u})-Z(\mathbf{u})\}$ under the constraint of unbiasedness of the estimate (5). These weights are obtained by solving a system of linear equations, which is known as the “ordinary kriging system”. Solution of the kriging system requires that covariances, Cov , between any two locations be calculated. These covariances are derived from the variogram model under an assumption of second-order stationarity.

$$\begin{cases} \sum_{\beta=1}^{n(\mathbf{u})} \lambda_{\beta}(\mathbf{u}) \gamma(\mathbf{u}_{\alpha} - \mathbf{u}_{\beta}) - \mu(\mathbf{u}) = \gamma(\mathbf{u}_{\alpha} - \mathbf{u}) & \alpha = 1, \dots, n(\mathbf{u}) \\ \sum_{\beta=1}^{n(\mathbf{u})} \lambda_{\beta}(\mathbf{u}) = 1. \end{cases} \quad (6)$$

The unbiasedness of the OK estimator is ensured by constraining the weights to sum to one, which requires the definition of the Lagrange parameter $\mu(\mathbf{u})$ within the system of equations. The addition of the Lagrange parameter can be thought of as the addition of another unknown to balance the additional equation added to the system to ensure unbiased estimates. The only information required for solution of the OK system is the variogram values for different lags, and these are readily derived from the variogram model fit to experimental values.

The kriging variance is also derived from the set of weights and the Lagrange parameter determined through solution of (6) and it is given as:

$$\sigma_{OK}^2(u) = \text{Cov}(0) - \sum_{i=1}^N \lambda_i \text{Cov}(u, u_i) - \mu \quad (7)$$

The covariances used to calculate the ordinary kriging variance are derived from the variogram model. The covariance with a zero distance argument, $\text{Cov}(0)$ is equal to the variance of the data set. The kriging variance has units of the square of the quantity being estimated, in this case head residuals, m^2 . It is important to note that the OK variance is not a function of the specific

data values, other than how those data values define the variogram of the residuals. As shown below, the kriging variance is only a function of the data configuration defined relative to the variogram model. Additionally, the kriging equations are non-parametric meaning that the OK estimate and the OK variance are the mean and variance of the local distribution defining the uncertainty in the estimate at any location, but there is no shape (e.g., Gaussian) assigned to that distribution. If it is necessary to assign a shape to this distribution, the multivariate Gaussian (mG) variant of kriging can be used.

2.4 Estimation Variance Calculations

The program **kt3d** (Deutsch and Journel, 1998) is used with the variogram model determined above to calculate both the estimated residuals and the estimation variance at all locations. The input parameter file for running **kt3d**, *kt3d.par*, is given in Appendix 2. The results of the kriging calculation are in the *\Monitoring_04\Geostat* subdirectory on the CD-ROM. The full calculation domain is 68,768 cells, each 100×100 meters, with 14,570 of those cells, 21 percent, lying to the west of the no-flow boundary. Those cells are not included in the calculations of estimation variance. A total of 4290 of the active cells are within the boundaries of the WIPP site. For the calculations done herein, the average estimation variance both within the flow domain and within the WIPP site are calculated for different monitoring well configurations.

The map of estimation variance for the August 2003 monitoring network defined in Table 3 is shown in Figure 5. From Figure 5, the effect of the monitoring network configuration on the resulting estimates of variance is obvious. The lowest estimation variance values, the nugget value of 13.0, occur at the well locations and the highest values occur at locations that are beyond the distance of the variogram range, 9000 meters, from the closest observation well. The minimum possible value of the kriging variance is the value of the nugget in the variogram model. Therefore, complete coverage of the site by the monitoring network would result in an estimation variance of 13.0 at all locations. Under ideal conditions, the maximum possible value of the kriging variance is equal to the total sill of the variogram, 58.2 m² in this case; however, in cases where data points are clustered, such as within the WIPP site, screening of some data by others can result in negative kriging weights that cause the kriging variance to increase above the level of the sill. The maximum kriging variance in these calculations is approximately 82 m². In the following analysis, the actual values of the kriging variance are not significant, it is only the relative changes in the kriging variance due to the addition, or subtraction, of wells to, or from, the monitoring network that are of interest.

The full monitoring network of 30 wells and the variogram model calculated from the head residuals at those 30 wells produce an average estimation variance within the flow domain of 53.6 m² and an average estimation variance within the WIPP domain of 23.5 m². From the map in Figure 5, it is obvious that there are many locations outside of the WIPP site where the addition of a well would have maximum impact on reducing the estimation variance. These locations are wherever a well could be located where its influence does not overlap on the region of decreased variance from an already existing monitoring well. Within the WIPP site, the estimation variance is already relatively low at all locations. In fact, given the small distances between some wells relative to the range of the variogram, it may be possible to remove some of the existing wells with only minimal increase in the estimation variance within the WIPP site boundary.

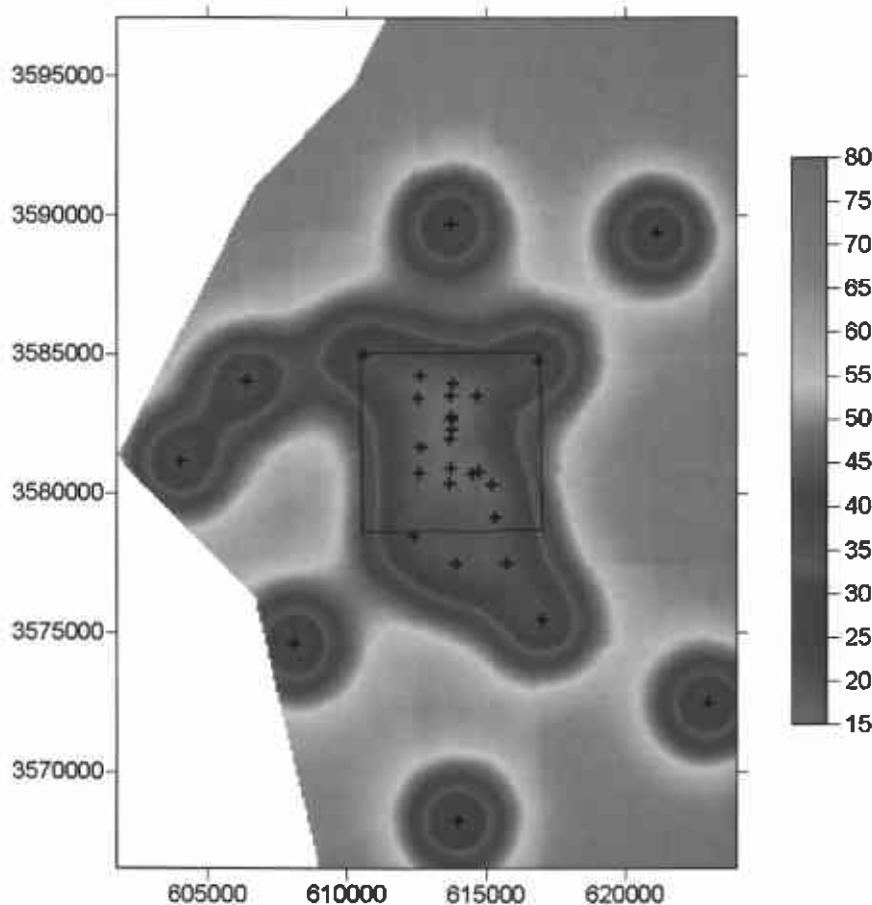


Figure 5. Kriging variance (m²) for estimation of the residuals between the estimated and measured heads.

Any location that is proposed for a new well can easily be added to the current data set and the estimation variance can be recalculated with inclusion of the proposed well. This approach takes advantage of the fact that the estimation variance does not depend on the data values, only the data configuration. This approach does require the assumption that the variogram model would not change significantly with the addition of one new well. Therefore it is easy to add one or

more proposed well locations to the current network and recalculate the estimation variance. Given the large number of potential well locations that could all produce a maximum reduction in the estimation variance, locations for the addition of new wells are not quantified any further than the map shown in Figure 5 for this study. When new well locations are proposed and/or drilled in the future, these calculations can be completed (See section 6.0 for an example).

The same approach for determining the variance reduction due to the addition of a new monitoring well can also be used to calculate the increase in the estimation variance from the removal of an existing well. In this case, it is possible to recalculate the variogram model from the remaining wells after any number of wells are removed; however, to make the process more efficient, the same variogram is used for all calculations done herein. This approach assumes that the variogram does not change significantly with the loss of any one of the 30 wells.

Each existing well, with the exception of the H-19 well and the WQSP wells that must remain in any future monitoring network configuration, is removed and the average estimation variances across the flow domain and the WIPP site are recalculated. These calculations were done in the *\Monitoring_04\Geostat\krig_minus* subdirectory through the use of a DOS batch file *krig_min.bat*. All of the input data files, each with a different data point removed, are located in this directory. A listing of this batch file is given in Appendix 3. Those wells that cause the smallest increase in average estimation variance are the ones that could be removed with a minimal impact on the ability of the monitoring network to provide accurate predictions of heads at locations without monitoring wells. The results of these calculations are shown in Table 5. The summary calculations for Table 5 are contained in the *results_min.xls* file in the *\Monitoring_04\Geostat\krig_minus* subdirectory

Table 5 shows the average estimation variance within the flow domain as well as within the WIPP site area as calculated using all wells in the network (top row) and also for the remaining 23 wells when each well is removed from the network in sequence. Removal of the WQSP wells and the H-19 well are not considered, as the WQSP wells must remain in any future monitoring network and H-19 is a relatively new, fiberglass-cased well with an expected long useful life. Table 5 also shows the percent increase in the average estimation variance for the entire domain and within the WIPP site when each well is removed from the network. Removal of wells that result in the largest increases in the estimation variance are the wells that are most important with respect to the ability of the network to predict heads. Therefore, if the goal is to predict heads across the entire domain, the wells that create the largest increases in estimation variance when removed are generally those located distant from other wells: AEC-7, WIPP-30, H-10, H-9, H-7, WIPP-25, and WIPP-26. Because these wells are located far from other wells, the removal of more than one of them would cause the overall increase in the estimation variance to be the sum of the increases due to removal of the individual wells. Small decreases in the estimation variance can also occur with the removal of a well (e.g., WIPP-13). These decreases are due to the configuration of the current wells creating negative kriging weights in the solution of kriging equations. These decreases are always less than one-tenth of one percent of the original variance and are considered as insignificant changes in this work.

Table 5. Results of estimation variance changes for the removal of one well from the current head-monitoring network.

Well Removed	Domain Average	Percent Increase	WIPP Average	Percent Increase
None	50.84	NA	23.30	NA
AEC-7	53.87	6.0	23.34	0.2
DOE-1	50.83	0.0	23.75	1.9
ERDA-9	50.84	0.0	23.31	0.0
H-2	50.85	0.0	23.74	1.9
H-3	50.84	0.0	23.33	0.1
H-4	51.08	0.5	24.29	4.2
H-5	51.94	2.2	25.37	8.8
H-6	51.46	1.2	24.06	3.3
H-7	52.09	2.5	23.33	0.1
H-9	52.93	4.1	23.30	0.0
H-10	53.11	4.5	23.34	0.2
H-11	50.84	0.0	23.69	1.6
H-12	51.97	2.2	23.33	0.1
H-17	50.83	0.0	23.45	0.6
P-17	50.96	0.2	23.40	0.4
WIPP-12	50.83	0.0	23.32	0.1
WIPP-13	50.80	-0.1	23.59	1.2
WIPP-19	50.84	0.0	23.30	0.0
WIPP-21	50.84	0.0	23.29	0.0
WIPP-22	50.84	0.0	23.30	0.0
WIPP-25	52.14	2.6	23.32	0.1
WIPP-26	51.99	2.3	23.32	0.1
WIPP-30	53.44	5.1	23.32	0.0

The wells that could be removed from the network and create the smallest increase in the estimation variance are those wells in close proximity to other existing wells. These include: DOE-1, ERDA-9, H-2, H-3, H-11, WIPP-12, WIPP-19, WIPP-21 and WIPP-22 (Table 5). However, because these wells are close to existing wells, the increase in the estimation variance from removing more than one of them will not be additive, but will become significantly larger as all wells are removed from a given area in the aquifer.

The wells outside of the WIPP site that, when removed, create the largest increases in the estimation variance for the flow domain have extremely little or no effect on the estimation variance within the WIPP site. These wells, AEC-7, H-9, H-10, H-12, WIPP-25, WIPP-26, and WIPP-30, are too far away from the WIPP site to impact the estimation variance therein. The most important monitoring wells, those that create the largest variance increase upon removal, for predicting heads within the WIPP site are: H-5, H-4, and H-6. The wells that create the smallest increases in estimation variance upon removal for both the WIPP site and the flow domain are: ERDA-9, H-3, WIPP-12, WIPP-19, WIPP-21 and WIPP-22. Any one of these six

wells could be removed with minimal effect on the ability of the network to predict heads across both the domain and the WIPP site. These calculations are for removal of a single well.

Two additional well-removal scenarios are considered. Wells WIPP-12 and WIPP-22 are removed from the network and then the changes in estimation variance for the removal of each remaining well in the network are calculated as done previously. Then, wells WIPP-12, WIPP-22, H-12, and P-17 are removed and each remaining well is removed one at a time and the estimation variances are recalculated. Wells H-12 and P-17 were removed based on their expected limited remaining life span within the monitoring network.

A decision was made to use the original residual variogram (Figure 4) for all calculations. The removal of two or more wells from the data set does change the shape and range of the variogram. However, the goal of this exercise is to examine changes in estimation variance due solely to the removal of different sets of wells and, to compare results across the different well removal scenarios, the original variogram was used for all calculations. The results of these two sets of calculations are shown in Tables 6 and 7.

Table 6. Results of estimation variance changes for the removal of one well from the head-monitoring network after wells WIPP-12 and WIPP-22 have been removed.

Well Removed	Domain Average	Percent Increase	WIPP Average	Percent Increase
WIPP-12 & WIPP-22	50.83	NA	23.32	NA
AEC-7	53.86	6.0	23.35	0.2
DOE-1	50.83	0.0	23.77	1.9
ERDA-9	50.83	0.0	23.32	0.0
H-2	50.84	0.0	23.75	1.8
H-3	50.83	0.0	23.34	0.1
H-4	51.07	0.5	24.30	4.2
H-5	51.91	2.1	25.35	8.7
H-6	51.45	1.2	24.08	3.3
H-7	52.08	2.5	23.34	0.1
H-9	52.93	4.1	23.32	0.0
H-10	53.10	4.5	23.35	0.1
H-11	50.83	0.0	23.70	1.6
H-12	51.96	2.2	23.34	0.1
H-17	50.82	0.0	23.47	0.6
P-17	50.95	0.2	23.41	0.4
WIPP-13	50.79	-0.1	23.64	1.4
WIPP-19	50.83	0.0	23.33	0.1
WIPP-21	50.83	0.0	23.32	0.0
WIPP-25	52.13	2.6	23.34	0.1
WIPP-26	51.98	2.3	23.33	0.1
WIPP-30	53.42	5.1	23.33	0.1

Table 7. Results of estimation variance changes for the removal of one well from the head-monitoring network after wells WIPP-12, WIPP-22, H-12, and P-17 have been removed.

Well Removed	Domain Average	Percent Increase	WIPP Average	Percent Increase
WIPP-12, WIPP-22, H-12, P-17	52.01	NA	23.43	NA
AEC-7	55.07	5.9	23.48	0.2
DOE-1	51.97	-0.1	23.89	1.9
ERDA-9	52.00	0.0	23.43	0.0
H-2	52.02	0.0	23.86	1.8
H-3	52.00	0.0	23.46	0.1
H-4	52.46	0.9	24.80	5.8
H-5	53.13	2.2	25.52	8.9
H-6	52.63	1.2	24.19	3.2
H-7	53.35	2.6	23.46	0.1
H-9	54.30	4.4	23.43	0.0
H-10	54.55	4.9	23.48	0.2
H-11	51.87	-0.3	23.84	1.7
H-17	52.59	1.1	23.65	0.9
WIPP-13	51.97	-0.1	23.75	1.4
WIPP-19	52.00	0.0	23.45	0.1
WIPP-21	52.00	0.0	23.44	0.0
WIPP-25	53.31	2.5	23.45	0.1
WIPP-26	53.16	2.2	23.45	0.1
WIPP-30	54.62	5.0	23.45	0.1

Results of the average variance calculations shown in Tables 5, 6, and 7 (columns 2 and 4) can be compared across all three tables as these are absolute values. The percent increases in estimation variance are relative to the base case in each table and cannot be compared across tables. The base cases considered are all 30 wells in the network (Table 5), wells WIPP-12 and WIPP-22 removed (28 wells total, Table 6), and wells WIPP-12, WIPP-22, H-12, and P-17 removed (26 wells total, Table 7).

The results show that removing wells WIPP-12 and WIPP-22 has negligible effect on the average estimation variances at both the domain and WIPP site scales. These results are expected as both of these wells are very close to other wells in the monitoring network (Figure 1). When H-12 and P-17 are also removed from the network, the change in average variances becomes significant (e.g., the average domain variance increases by more than one percent from 50.8 to 52.0. This is also expected as these two wells are not close to other wells in the network and therefore have a larger impact. The change in variances due to removal of just these two wells can be determined by comparing the top rows of Tables 5 and 6. The increase in variance with the removal of H-12 and P-17 is larger for the domain than within the WIPP site as both of these wells are outside of the WIPP site boundaries. From the final set of results in Table 6, wells ERDA-9, H-3, WIPP-19 and WIPP-21 are likely candidates for removal.

In summary, it is relatively simple to calculate the decrease or increase in the head estimation variance over a specified area from the addition or removal of a single monitoring well, respectively. The maximum reduction in estimation variance, or increase in the ability to predict heads, can be achieved by placing a new monitoring well in any location of the flow domain that is far away from any existing well. There are a large number of locations in the domain where a new well could be placed to meet this condition. At this point in the analysis, a maximal reduction in variance from a new well can be considered as a necessary, but not complete, condition for locating a new well. The estimation variance map shown in Figure 5 will be combined with other analyses such as local gradient estimators and sensitivity maps, as well as practical concerns such as development costs and access to the location, to determine the optimal locations for additional wells.

Removal of wells from the existing monitoring network was also examined using the estimation variance calculations. The impact of well removal was evaluated by calculating the increase in estimation variance for both the entire flow domain and the area of the WIPP site. These calculations were done for the removal of one well at a time starting from a base case network of 30, 28, or 26 wells and the results are only valid for the removal of the one specified well. These results also assume that the variogram is constant across all monitoring network configurations. These calculations can be completed again for removal of combinations of multiple wells when those combinations of interest are defined. Wells that are most important to the existing monitoring network that should not be removed are listed above and are, generally, those wells most distant from any existing wells. Wells that have the smallest influence on the ability of the current network to predict heads at unmeasured locations across the entire flow domain as well as within the WIPP site are also listed above. If more than one well is to be removed, the combinations of wells should be selected from this list.

2.5 Calculation Details

All calculations done for the variance reduction section were completed on a PC with a 1.7-GHz Pentium 4 chip under the Windows 2000 operating system. These calculations are contained within the `\Monitoring_04\Geostat\` directory on the CD-ROM accompanying this analysis package. Four different calculations were done in this section:

- 1) A planar trend was fit to the existing data and residuals between the measured heads and the planar trend were calculated using the commercial off-the-shelf software **SigmaPlot** (ver. 8.02).
- 2) Variograms of the residuals were calculated and modeled using the commercial off-the-shelf software **VarioWin** (ver. 2.21). The variogram model parameters determined here are necessary input to the **kt3d** code for the kriging step.
- 3) The residual fields were kriged using the software package **kt3d**. **kt3d** is part of the **GSLIB** public domain geostatistics software library and has been qualified and used previously on the WIPP project for the inverse calibration of transmissivity fields (McKenna and Hart, 2003). The output files from **kt3d** are named "*Aug_03_resid_min_WELL.out*" where the WELL portion of the file name is replaced with a character string that identifies the well removed from the network for that particular calculation. The output files from running **kt3d** multiple times are used as input to the **calc_var.c** routine.

- 4) The average estimation variance across the domain and within the WIPP site boundaries for the case of all 30 wells and for each case where a single well is removed are calculated using the routine: **calc_var.c**. These calculations are in the *\Monitoring_04\Geostat\krig_min* subdirectory. The routine **calc_var.c** is qualified as part of this analysis package. The final results of the variance reduction calculations are stored in the Excel spreadsheet: *results_min.xls* and the calculations of the percent variance reduction for each different configuration of monitoring wells relative to the current monitoring network are also calculated in this spreadsheet.
- 5) The average estimation variance across the domain and within the WIPP site boundaries for the base case of 28 wells and for each case where a single well is removed are calculated using the same routine: **calc_var.c**. These calculations are in the *\Monitoring_04\Geostat\krig_min3* subdirectory. The final results of the variance reduction calculations are stored in the Excel spreadsheet: *results_min3.xls* and the calculations of the percent variance reduction for each different configuration of monitoring wells relative to the current monitoring network are also calculated in this spreadsheet.
- 6) The average estimation variance across the domain and within the WIPP site boundaries for the base case of 26 wells and for each case where a single well is removed are calculated using the same routine: **calc_var.c**. These calculations are in the *\Monitoring_04\Geostat\krig_min5* subdirectory. The final results of the variance reduction calculations are stored in the Excel spreadsheet: *results_min5.xls* and the calculations of the percent variance reduction for each different configuration of monitoring wells relative to the current monitoring network are also calculated in this spreadsheet.

3.0 Local Gradient Estimation

The Culebra is a nearly textbook example of a 2-D aquifer. It is much more laterally extensive than it is thick and it is bounded on the top and bottom by relatively impermeable units. For such an aquifer, the groundwater flow patterns are essentially two-dimensional and any three measurements of the hydraulic head at different locations are all that is needed to estimate the magnitude and orientation of the hydraulic gradient. This three-point estimation is also referred to as a “local” gradient estimate as the estimates are relevant only in the area of the three head measurements. Recently, there has been a strong interest in the use of three-point estimators for discerning information on groundwater flow patterns that is more highly resolved than just an estimate of the magnitude and orientation of the regional gradient.

Two separate sets of calculations are done for the application of three-point estimators to determining flow patterns in the Culebra:

- 1) Simulations are completed using synthetic data to critically examine the applicability of three-point estimators through Monte Carlo simulation. The effects of estimator shape, orientation of the estimator relative to the direction of groundwater flow and the effects of measurement error are examined using synthetic data. Results of these calculations provide a set of constraints for application of three-point estimators to the Culebra data in step 2.
- 2) The use of three-point estimators in detecting temporal changes in the Culebra hydraulic gradient and in determining both redundant wells in the existing monitoring network and best locations to add wells to the monitoring network is demonstrated. This second set of calculations is done using data collected from the Culebra monitoring network.

3.1 Background

The earliest work on examining three-point local hydraulic gradient estimators appears to be that of Mizell (1980) who used perturbation theory to develop analytical expressions for the variance of the estimated magnitude and orientation of the hydraulic gradient as a function of the length scale of the three-point estimator normalized by the correlation length of the transmissivity field. All of Mizell’s (1980) results were calculated from only a single triangle shape (right-isosceles) and the analytical expressions are limited to relatively small values of transmissivity field variance. Results show that as the length scale of the estimator reaches and exceeds the correlation length of the transmissivity field, the variance in the estimates decreases significantly. In Mizell’s formulation, for estimator length scales that are smaller than the correlation length of the transmissivity field, the variance of the estimates is constant. The results of Mizell (1980) show that measurement error only affects the results for estimator length scales less than the correlation length of the transmissivity field. A simple application to three wells with 19 weekly observations is presented.

The work of Mizell (1980) does not appear to have been published outside of his dissertation and had largely gone unrecognized with the exception of Ruskauff and Rumbaugh (1996) who used Mizell’s results to guide a series of groundwater flow and solute transport simulations. Ruskauff and Rumbaugh’s (1996) results point out the fact that a groundwater flow model calibrated to

observed heads within an acceptable tolerance will not necessarily reproduce the true magnitude and orientation of the gradient.

Cole and Silliman (1996) looked at the ability of a three-point estimator with an isosceles shape to accurately determine the orientation and magnitude of the hydraulic gradient in unconfined aquifers. The goals of this study included a comparison of estimates made with the non-linear equation for unconfined head versus estimates made with a linearized version of this equation in terms of head squared. Additionally, Cole and Silliman (1996) completed a Monte Carlo modeling study of the effects of heterogeneity on the accuracy and precision of the orientation and magnitude estimates. Results of this work showed that the linearized unconfined flow equation provided unbiased estimates of both orientation and magnitude. Contrary to the theory developed by Mizell (1980), hydraulic conductivity heterogeneity with different levels of variability and correlation lengths produces slightly biased estimates of the magnitude and the orientation for well separation distances of less than one correlation length. For larger well separation distances, the accuracy and precision of the estimates improve, but large standard deviations about the orientation estimates exist at relative well separations of 10 correlation lengths or more.

Silliman and Frost (1998) pointed out that local estimates of the hydraulic gradient made with three-point estimators could provide significant information on the regional gradient as well as local variations in that regional gradient. They present plots of the estimated orientation and magnitude from each combination of three wells as a function of the size (area) of the estimator and demonstrate that these types of plots can provide additional information on the regional gradient beyond what might be gained from traditional head contouring techniques. Demonstrations of these techniques are presented on a laboratory “ant-farm” aquifer and from data collected at a field site. Results show that the plots developed in this work are excellent at identifying anomalous flow directions and magnitudes and that when correlated, these two types of anomalous results may indicate a region of low conductivity in the aquifer. This paper also demonstrates the use of examining data at different times to detect changes.

Silliman and Mantz (2000) examined the effect of measurement error on the ability of local gradient estimators to produce accurate estimates of the hydraulic gradient. This work was focused on the effects of measurement error in estimating vertical gradients from four measurement points in a three-dimensional domain. The results show that relatively small amounts of measurement error can cause the estimated orientation of the vertical component of the gradient to be straight up or straight down. Silliman and Mantz (2000) call for better determination of the measurement error in field studies and warn that measurement error will also complicate estimates of horizontal gradients when the gradient is small and/or the wells are placed close together.

The solution for fitting a potentiometric surface to more than three head measurements is to minimize a least squares, or average absolute, measure of the residuals between the fitted potentiometric surface and the measured heads. Such an approach was followed by Devlin (2003) who developed a spreadsheet program to calculate a least squares best-fit of the hydraulic gradient using multiple linear regression with up to 20 different head measurements. The planar surface that best fits multiple head measurements provides the orientation and magnitude of the

regional hydraulic gradient rather than a more local estimate as can be obtained when using only three measurements.

A large amount of previous work in monitoring network design has approached the problem from the perspective of minimizing the head estimation variance calculated from the proposed network (e.g., Rouhani, 1985; Loaiciga, 1989). This focus on monitoring head has led to the development of techniques for determining point locations that are, by some measure, optimal for the placement of new monitoring wells. A different perspective is to design a monitoring network to detect changes in both the magnitude and orientation of the hydraulic gradient. Estimation of the hydraulic gradient requires at least 3 wells, for a 2-D flow field, or 4 wells for a 3-D flow field and, contrary to head measurements, gradient estimates cannot be made from a single point support datum. With the exception of the work by Conwell, et al. (1997), who were interested in optimizing the design of networks of local gradient estimators for the calculation of variograms, monitoring network design from the perspective of data obtained using local gradient estimators has not been studied.

This portion of the report presents a critical examination of the ability of three-point estimators to accurately predict the orientation and magnitude of the gradient and then applies three-point estimators to monitoring network design. Specifically, this work provides:

- 1) Assessment of the accuracy and precision of the gradient estimates under measurement error when measurement error is cast in terms of relative head drop across the three-point estimator.
- 2) Examination of the effect of groundwater flow orientation on accuracy and precision of the gradient estimates made by three-point estimators.
- 3) Systematic examination of the effect of estimator shape on the accuracy and precision of the gradient estimates.
- 4) Extension of previously developed graphical techniques to detect and quantify changes in the hydraulic gradient over time.
- 5) Use of three-point estimators to identify redundant wells in an existing monitoring network.
- 6) Use of three-point estimators to identify optimal locations at which wells can be added to the monitoring network to improve the ability of the network to detect changes in the gradient.

3.2 Estimation of the Gradient

Following the work of Silliman and Frost (1998), the equation of the plane defining the potentiometric surface of a confined aquifer is:

$$H(x, y) = Ax + By + C, \quad (8)$$

where H is the value of head measured at location (x,y) and A , B and C are coefficients with unknown values. Three measurements of H at unique (x,y) locations provide enough information to set up three equations and solve for the three unknowns: A , B and C . This solution leads to expressions for the magnitude and orientation of the hydraulic gradient:

$$magnitude = \sqrt{A^2 + B^2}, \quad (9)$$

$$orientation = \arctan\left(\frac{B}{A}\right). \quad (10)$$

A slightly expanded formulation of these expressions is given by Devlin (2003). Silliman and Frost (1998) also provide the equivalent formulations for an unconfined aquifer.

3.3 Local Gradient Estimator Error Analysis

Two different aspects of the estimator and head measurement error are examined through Monte Carlo simulations. These two aspects are the relative measurement error and the shape of the estimator. All simulations assume that the estimator is applied to a steady-state groundwater system in a homogeneous aquifer. The effects of the homogeneous aquifer assumption are examined further below.

3.3.1 Relative Measurement Error

The amount of error inherent in measuring the head within an aquifer is not easily quantified. Multiple factors including calibration and drift of the electronics in the measurement device, changes in the measurement device hardware (e.g., cable stretching), elevation survey errors, and variations in barometric pressure make it difficult to determine the true head level at any point in a confined aquifer. Additionally, as pointed out by Ruskauff and Rumbaugh (1996), the importance of the amount of measurement error is relative to the amount of head drop across the estimator. In areas of low gradients, small measurement errors may be enough to completely degrade the estimates of hydraulic gradient magnitude and orientation.

For this study, head measurement error is assumed to be normally distributed with a zero mean and defined standard deviation: $N(0, \sigma)$. Measurement error is also assumed to be independent between the three different measurement points in the estimator. In the Monte Carlo simulations with synthetic data, measurement error is drawn independently from the $N(0, \sigma)$ distribution for each of the three wells in a given three-point estimator. This error is then added to the known, true, head value at each well to define the measured head (true + error) at each well and the orientation and magnitude of the hydraulic gradient are calculated from these measurements. For the case of synthetic data, the calculated values of the orientation and magnitude of the gradient are compared to the true values calculated without the addition of error. Results of this comparison are shown as a function of the relative head measurement error (RHME) defined as:

$$RHME = \frac{\sigma}{head\ drop} \quad (11)$$

where *head drop* is the decrease in head across the estimator from one edge to the opposite along a vector parallel but opposite to the direction of the gradient. The head drop is defined by the orientation and magnitude of the true gradient, both of which are known for the synthetic data case. The RMHE is the absolute measurement error normalized by the expected head drop across an estimator.

Equation (8) is linear in head and therefore we would expect the variance of the estimates made with (8) to increase linearly with increasing amounts of head measurement error (Taylor, 1996). To examine the increase in the variance of the estimates, a single estimator shape, a right-isosceles triangle, was used with 5000 sets of head measurement errors drawn at each of five different levels of RHME (one percent through ten percent). These measurements are then used to estimate both the magnitude and orientation of the hydraulic gradient, and the ratio of the estimated to true magnitude and orientation (Figure 6). These results show that independent, normally distributed measurement errors produce unbiased estimates of the magnitude and orientation and that increasing measurement error decreases the precision (larger estimation variance) of the gradient magnitude estimates more strongly than it does the gradient orientation estimates.

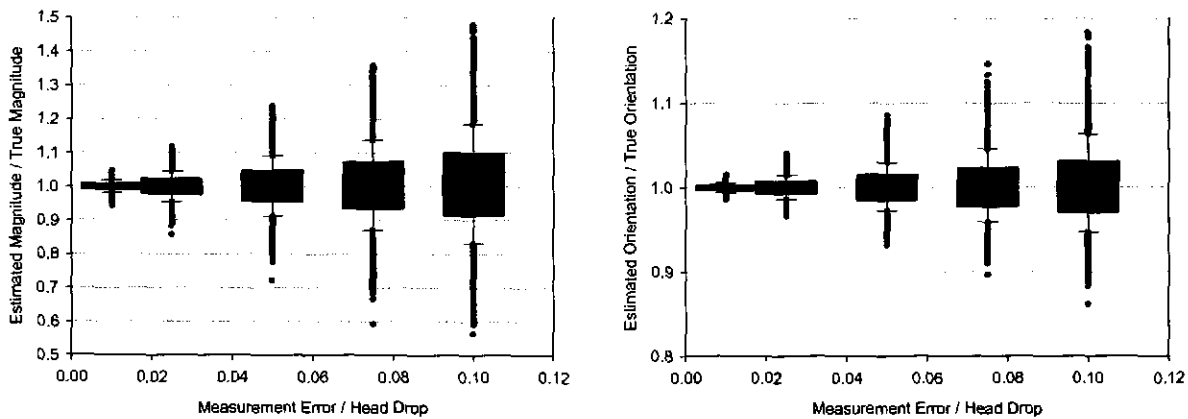


Figure 6. Box and whisker plots of the distribution of the ratio of the estimated to true magnitude (left graph) and the estimated to true orientation (right graph) as a function of the RHME. The boxes define the 25th and 75th percentiles. The whiskers define the 5th and 95th percentiles and the circles beyond the ends of the whiskers are individual results. All distributions contain 5000 results.

3.3.2 Estimator Shape and Gradient Orientation

Previous studies (e.g., Mizell, 1980; Cole and Silliman, 1996) have generally used a single estimator shape, most often an equilateral or right-isosceles triangle and, to date, the effect of different estimator shapes on the final gradient estimates has not been systematically studied. Intuitively, triangles with very large or very small base to height ratios may provide poor estimates of the magnitude and/or orientation of the hydraulic gradient for certain groundwater flow directions.

Here, eleven different estimator shapes are examined to determine the effect of shape on the ability of the three-point estimator to produce accurate and precise estimates of the gradient. The eleven different shapes are all isosceles triangles and are defined by both the size of the two equal angles as well as the base to height ratio (Figure 7). Each of the eleven different estimators

encompasses the same area. For each estimator shape, the direction of groundwater flow is varied in roughly 15-degree increments around the full 360-degree range (24 different directions). At each groundwater flow orientation, Monte Carlo simulation is used to draw 2000 head measurements at each measurement location with a specified value of RHME. Four different levels of RHME are used: 0.001, 0.005, 0.01, and 0.05.

The results of this analysis were examined in two ways: 1) the effect of flow orientation on the estimates of magnitude and orientation are examined for an individual estimator shape; and 2) the results from the different flow orientations and estimator shapes are summarized.

Isosceles Triangles with Equal Area

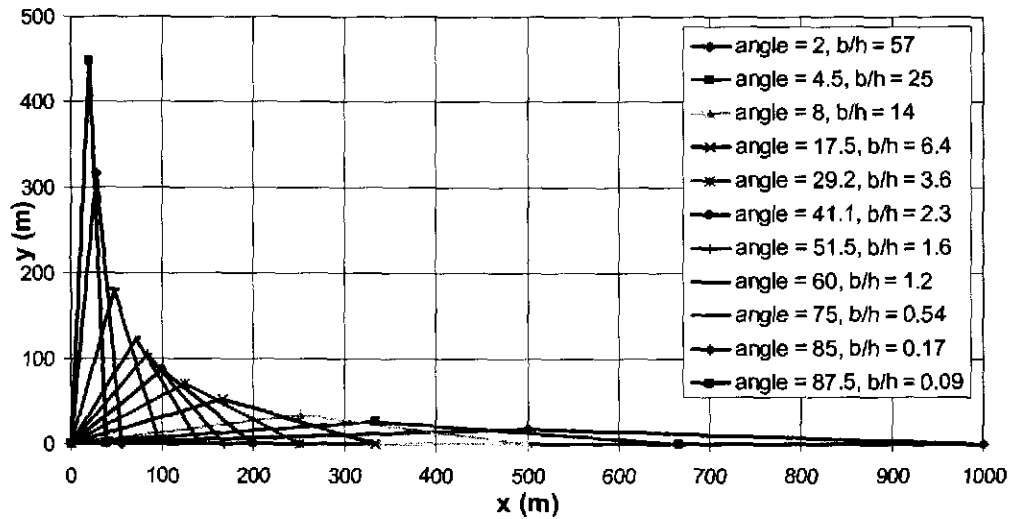


Figure 7. Shapes of the different triangles examined in this study. Each triangle is defined by the size of the two equal angles and the base to height ratio. All triangles have the same area.

The orientation of the flow relative to the three-point estimator can have a significant effect on both the gradient magnitude and orientation estimates. This result is demonstrated in Figure 8 that shows the results for the 41-degree estimator (base/height = 2.3). Figure 8 (top graph) shows the percent absolute error in the estimation of the gradient magnitude as a function of the orientation of the groundwater flow direction. Percent absolute error in the magnitude of the gradient is calculated as:

$$\text{Percent Absolute Error} = \frac{\text{TrueMagnitude} - \text{EstimatedMagnitude}}{\text{TrueMagnitude}} \times 100$$

Each point on the upper graph in Figure 8 represents the 95th percentile of the distribution across 2000 realizations (i.e., 95 percent of all calculated errors are less than or equal to the value shown by each point in Figure 8). Results for calculations at each of the four different values of RHME are shown. The solution for the gradient is set up such that a singularity occurs when the flow direction is aligned with the right leg of the triangle and results with that flow direction cannot be accurately determined. Figure 8 (lower graph) shows the absolute error, in degrees, for the estimates of the orientation of the hydraulic gradient. The lower graph in Figure 8 is the same as the upper graph with the exception that the Y-axis shows the absolute error of the estimated orientation, not the percent absolute error as shown in the upper graph.

Disregarding the results at flow directions of -41 and 139 degrees (aligned with the right leg of the triangle), the results in Figure 8 show that the different orientations of the groundwater flow direction can change the resulting error in the estimates of the magnitude approximately one-half

of an order of magnitude. Changes in the error of the orientation estimates are somewhat less than the errors calculated for the gradient magnitude (lower graph, Figure 8).

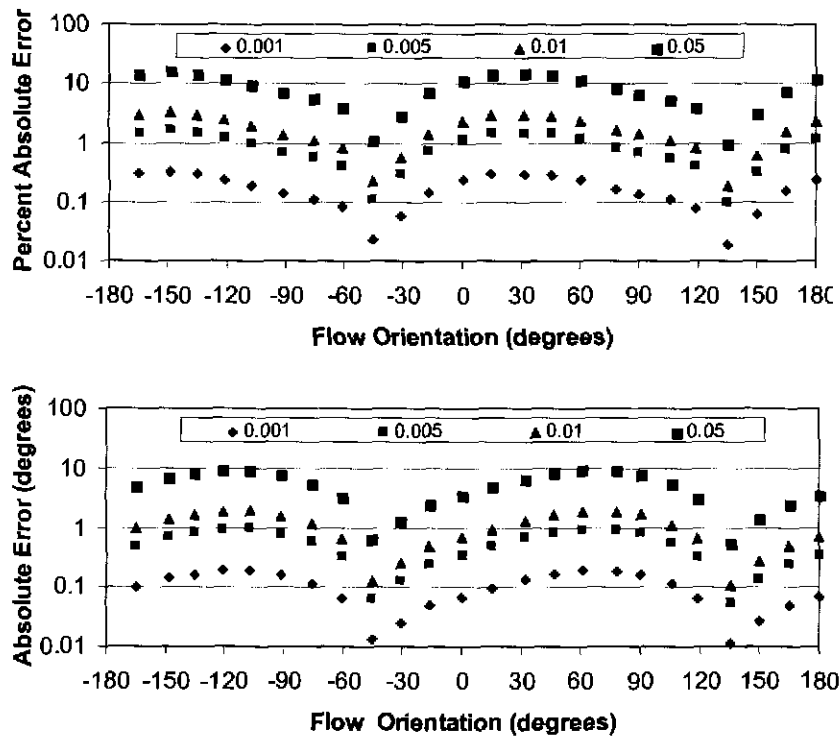


Figure 8. The 95th percentile error values for gradient magnitude (upper graph) and orientation (lower graph) for the 41 degree estimator as a function of groundwater flow direction and RHME. The different levels of RHME are shown in the legend.

The change in error across the different flow directions is abstracted by calculating the median value of the 95th percentile error across all 24 flow directions for each estimator shape. These median error values are then plotted as a function of estimator shape for each of the four different values of RHME (Figure 9). Results in Figure 9 show that approximately one order of magnitude variation in the hydraulic gradient magnitude error exists across the eleven different estimator shapes for a single level of RHME (upper graph, Figure 9). Results are similar for the hydraulic gradient orientation error (lower plot, Figure 9) with the range in variation being slightly less than one order of magnitude for any given level of RHME. For both the magnitude and orientation results, the minimum error values occur for three-point estimators with base to height ratios between 0.5 and 5.0.

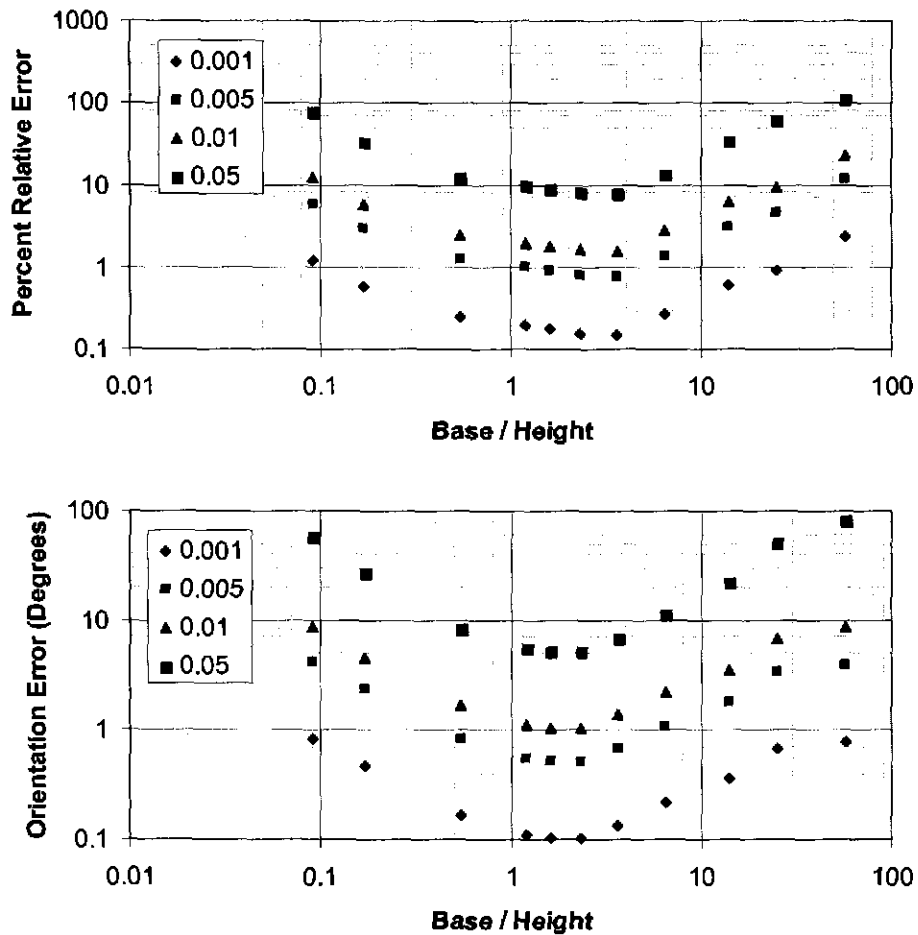


Figure 9. The median 95th percentile errors in magnitude (upper graph) and orientation (lower graph) as a function of estimator shape and RHME. The different RHME values are shown by the different symbols and the legend. Each median value is calculated across the results for the 24 different flow directions for a given estimator shape (e.g., the results in Figure 8).

The results of this analysis prove that not all three-point estimators produce equally accurate estimates of the magnitude and orientation of the hydraulic gradient. Any analysis using three-point estimators of the local gradient needs to take into account the shape of the triangle and the value of the RHME.

3.3.3 Choosing Acceptable Three-Point Estimators

For a given monitoring well network, the total number of possible three-point estimators can be determined as the number of unique combinations of wells taken three at a time from the existing monitoring network. The number of unique combinations containing n wells that can be chosen from a total of m wells in the network is:

$$mCn = \frac{m!}{n!(m-n)!} \quad (12)$$

where mCn is read as “ m choose n ”. For the set of monitoring wells considered in this example ($m=30$), there are 4060 possible three-point estimators. However, as seen above, not all estimators yield equivalently accurate estimates of the local gradient.

The criterion for acceptance of the estimators based on shape is simply to calculate the base and height dimensions of each estimator and determine if the base/height ratio falls within the acceptable limits of 0.5 to 5.0.

The criteria for acceptance of estimators with respect to the RHME is implemented as follows:

- 1) All available wells for a given time period are used to calculate the magnitude and direction of the regional gradient as a best-fit plane to the observed data. These calculations are done in **SigmaPlot** and are in the `\Monitoring_04\Planar_Trend\` subdirectory
- 2) The standard deviation of the normally distributed measurement errors is estimated based on knowledge of the measurement instrument and field conditions and an acceptable value of the RHME is specified.
- 3) The minimum distances in the X and Y directions (East-West and North-South) required to achieve an acceptable head drop across an estimator based on the X and Y components of the calculated regional gradient, $(dh/dx)_{reg}$ and $(dh/dy)_{reg}$, and specified acceptable RHME are determined as:

$$X_{min} = \frac{\sigma}{\left(\frac{dh}{dx}\right)_{reg} RHME} \quad Y_{min} = \frac{\sigma}{\left(\frac{dh}{dy}\right)_{reg} RHME} \quad (13)$$

- 4) Each three-point estimator is evaluated to determine whether or not it can contain X_{min} and Y_{min} within the bounds of the three wells. If yes, the estimator is retained. If not, the estimator is not used to estimate properties of the gradient.

The implementation of the RHME criteria as described above is relatively simple. However, the calculation of X_{min} and Y_{min} will degenerate if the regional gradient is oriented in one of the cardinal directions such that either $(dh/dx)_{reg}$ or $(dh/dy)_{reg}$ becomes undefined.

3.4 Application 1: Monitoring Temporal Changes

The monthly Culebra head monitoring program at WIPP has incorporated practices over the past several years to reduce absolute head measurement error to as little as possible. These practices include routine calibration of the measurement instrument, using the same instrument for all well measurements, surveyed elevations at each well and taking all measurements within a 24-36 hour period to reduce head fluctuations in a single sampling round due to changes in barometric pressure. However, as pointed out by other authors (e.g., Silliman and Mantz, 2000), it is nearly impossible to completely quantify the head measurement error in the field. For the examples shown in this work, the head measurement error is assumed to have a Gaussian distribution with a mean of zero and a standard deviation of 0.10 meters.

The RHME is defined relative to the head drop across a given triangle along the direction of groundwater flow as would occur given that the regional gradient in the Culebra applied locally at all locations. This use of the regional gradient is done to avoid using the heads measured at the three wells to estimate the local gradient as well as the local head drop and the RHME. For each set of measurements, the magnitude and the orientation of the regional gradient are calculated using **SigmaPlot 8.0**. Results of these regional gradient calculations for both time periods are stored on the CD-ROM in the \Monitoring_04\Planar_Trend\ directory in the *trend_results.xls* file. The magnitude and orientation of the calculated trends are shown in Table 8. The orientations in Table 8 are given as degrees counterclockwise from north where the negative sign indicates the counterclockwise direction.

Table 8. Magnitude and orientation of the regional gradient as determined through the best-fit plane technique for the 2000 and 2003 time periods.

Observation Period	Magnitude (-)	Orientation (degrees)
August 2000	1.60E-03	-172.84
August 2003	1.64E-03	-173.04

The results in Table 8 show that the regional gradient is essentially unchanged from 2000 to 2003. The average of the two gradient magnitudes, 1.62E-03, and the average of the estimated orientations, -172.94 degrees, will be used in the calculations of the local gradients from the different estimators.

For a measurement distribution with a standard deviation of 0.10 meters and an acceptable RHME of 0.02, two percent of the expected head drop across an estimator using the regional gradient, the minimum X and Y distances that an estimator needs to have (Equations 13) are approximately 25,000 and 3000 meters respectively. The large difference in the necessary estimator size between the X and Y directions is due to the orientation of the regional gradient being nearly due south. The closer the orientation of the regional gradient to due south, the less significant the east-west components of the gradient vector become to the point where if the orientation was completely due south, it would not be possible to calculate a distance in the X direction using (13). Given this regional orientation, only the minimum Y distance is used to screen out potential three-point estimators.

The local estimates of the gradient by each three-point estimator are calculated for: 1) all possible estimators; 2) those estimators with a shape such that $0.5 > \text{base/height} > 5.0$; and 3) those estimators with both $0.5 > \text{base/height} > 5.0$ and a minimum north-south distance of 3000 meters. The results of these calculations are shown via the relationships developed by Silliman and Frost (1998). However, to better interpret the information from the two different sampling periods, the results of each sampling period are shown on a single graph. Figure 10 shows the estimated magnitude of the gradient as a function of estimator size (area). The top image in Figure 10 shows all of the 4060 possible estimators, the middle image shows only those estimators that meet the shape criterion, and the bottom image of Figure 10 shows only those estimators that meet both the shape and RHME criteria.

The graphs in Figure 10 show the estimated magnitude as a function of the size (area) of the three-point estimator. For the larger triangles, the estimated magnitudes approximate that of the regional magnitude of $1.6E-03$ as determined above using the best-fit method. The size of the estimators does not change from one time period to the next and therefore it is possible to compare results along any vertical line for the same estimator. Changes in the estimated magnitude from 2000 to 2003 are evident when the “plus” and “box” symbols do not overlap, but are offset vertically from one another. Several instances of changes between time periods are visible in lower left portions of the images.

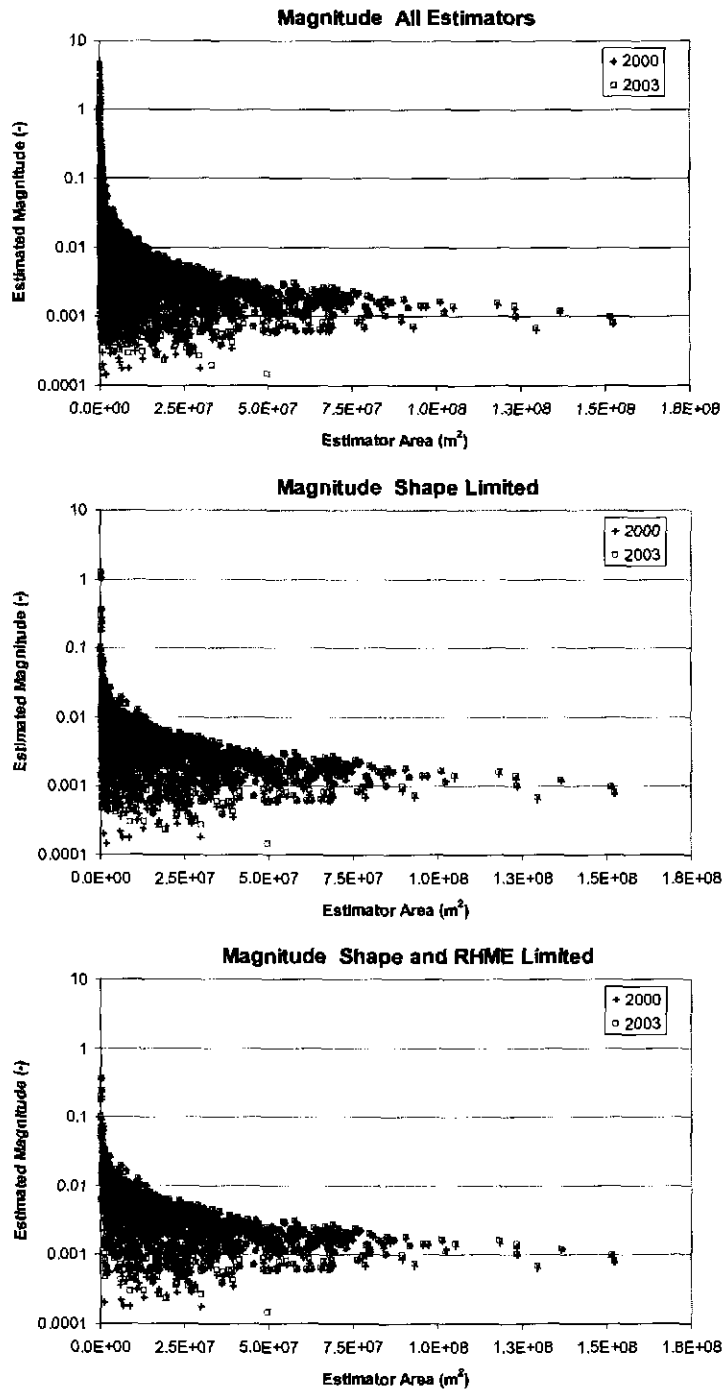


Figure 10. Estimated magnitude of the hydraulic gradient across all three-point estimators as a function of estimator size for the 2000 and 2003 head data. The upper graph shows all estimators, the middle graph shows results for those estimators meeting the shape criterion, and the lower graph shows results for estimators meeting the shape and RHME criteria.

Results (Figure 10) show that as additional criteria are applied to selecting estimators, the range in the estimated gradient magnitudes decreases from roughly 4.5 orders of magnitude to 3.5 orders of magnitude with the biggest decrease due to the application of the RHME criterion (bottom graph, Figure 10). Almost all of the reduction in the range of magnitude estimates takes place in the estimators with the smallest areas (left sides of the graphs).

The application of the estimator shape and RHME criteria to the set of all possible estimators reduces the number of estimators to those that should give acceptable estimates based on the simulations discussed above. The number of estimators in each graph of Figure 11 are 4060, 2280, and 1879 from top to bottom, respectively. The application of the shape and RHME criteria reduce the number of estimators to 56.2 and 41.7 percent of the original number, respectively. The final result in the bottom image is noteworthy in that using only the estimators that provide acceptable results, there are still three and a half orders of magnitude variation in the estimated magnitudes of the hydraulic gradient for this region of the Culebra. This variability in the results is due to heterogeneity within the Culebra causing higher and lower gradient magnitudes in different locations.

A set of graphs similar to those in Figure 10 is shown in Figure 11 for the orientation estimates. The orientations are measured clockwise from north where north equals a zero degree orientation. Similar to the magnitude estimates, the larger estimators produce estimates that approach the regional estimate of approximately -173° as calculated above. However, there is considerable variation in the orientation of the largest estimators between -150° and -180° and there are also several large estimators that produce orientation estimates of approximately 170 (-190) $^\circ$. All of the large estimators, those with sizes of $1.0E+08m^2$ or larger, produce consistent orientation estimates between the 2000 and 2003 sampling periods. Variations of the estimated orientation of 20° or more can be seen for some of the three-point estimators with smaller areas.

Application of the acceptable estimator criteria developed through simulation reduces the variability of the estimates from a somewhat uniform distribution (upper image, Figure 11) to a more bimodal distribution (lower image, Figure 11) with the modes centered on the -150° and $+165^\circ$ orientations. There is also a relatively large number of estimates from small area estimators between 60° and 90° for both time periods. Heterogeneity within the Culebra creates this variability in the estimated orientations.

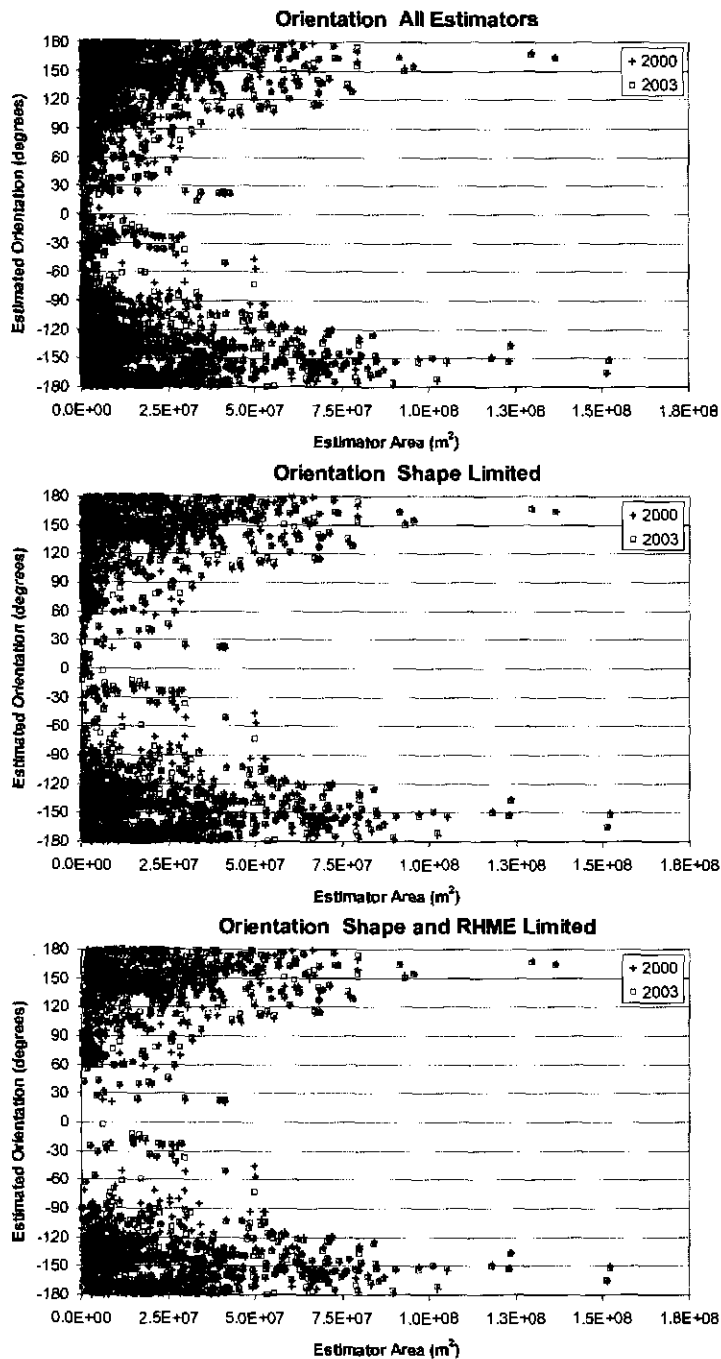


Figure 11. Estimated orientation of the hydraulic gradient across all three-point estimators as a function of estimator size for the 2000 and 2003 head data. The upper graph shows results for all estimators, the middle graph shows results for those estimators meeting the shape criterion, and the lower graph shows results for estimators meeting the shape and RHME criteria.

The final set of comparison graphs is shown in Figure 12. These graphs show the estimated orientation as a function of the estimated magnitude. As noted previously (e.g., Silliman and Frost, 1998), there can be strong relationships between the magnitude and orientation. Most interestingly, magnitudes that are significantly larger than the regional magnitude may have

orientations that are significantly off of the regional orientation. Silliman and Frost (1998) attributed these results to areas of the aquifer where flow was crossing low-permeability regions; however, they did not consider estimator shape or RMHE when interpreting their results.

Figure 12 (upper image) shows that the Culebra does exhibit coupled estimates of magnitude and orientation that are both significantly off of the regional values. The largest magnitudes in this figure are oriented at both 90° and -90° and are fairly consistent from 2000 to 2003. Application of the shape criterion to these results (Figure 12, middle image) shows that the majority of these estimates along the $\pm 90^\circ$ orientations are spurious and due to extremely tall or flat three-point estimators. The majority of the estimators that meet the shape criterion show a reasonably uniform distribution of magnitudes near the 155° and -155° orientations observed in Figure 12 with the largest magnitudes occurring at 135° , 75° , and -135° as well as a few at 90° and -90° .

Application of the RHME criterion to these data results in the removal of all but four pairs of estimated magnitudes greater than 0.1 and causes the majority of the remaining estimates to be clustered near 150° and -150° (Figure 12, bottom image). Additionally, there are some results trending towards higher magnitudes for orientations between 150° and 60° and -150° and -90° . Almost all of the remaining estimates have magnitudes between 0.001 and 0.01, and the largest change between 2000 and 2003 occurs in areas where the gradient is the smallest.

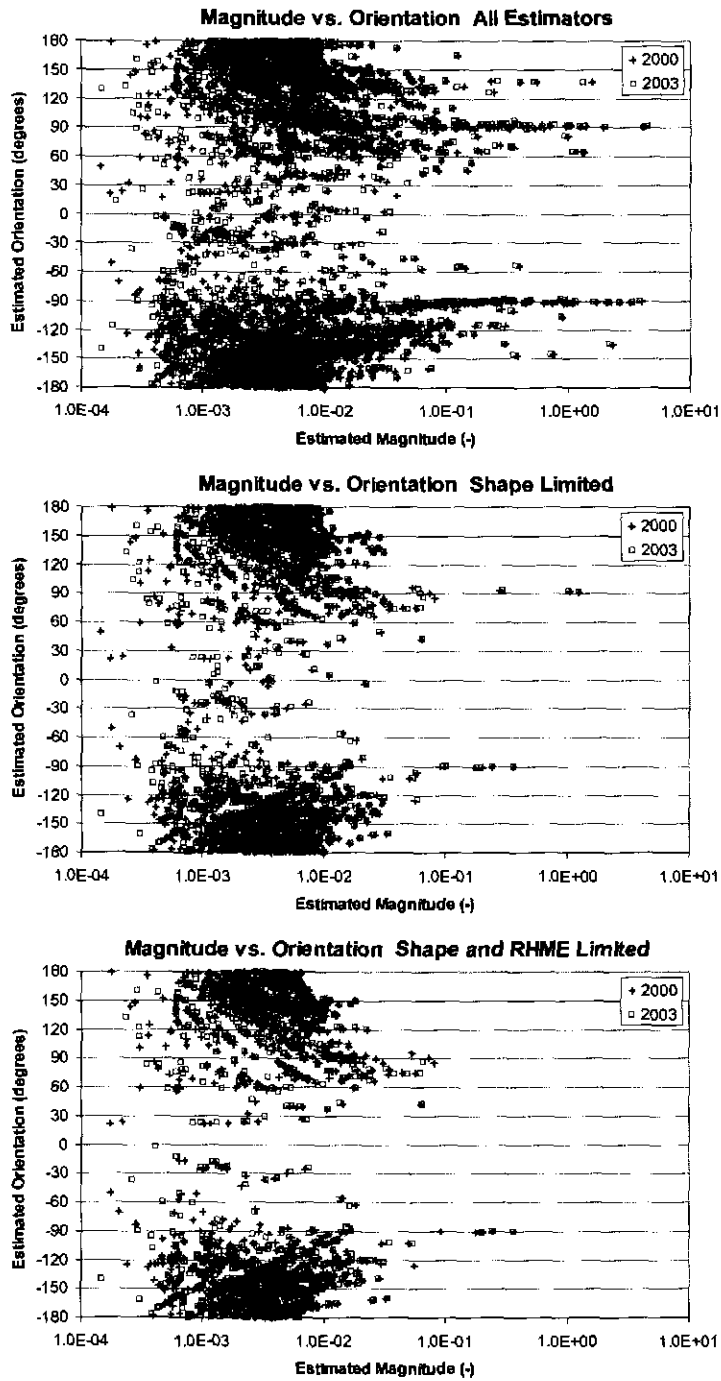


Figure 12. Estimated orientation of the hydraulic gradient as a function of estimated magnitude for the 2000 and 2003 head data. The upper graph shows results for all estimators, the middle graph shows results for those estimators meeting the shape criterion, and the lower graph shows results for estimators meeting the shape and RHME criteria.

In addition to the series of plots presented in Figures 10, 11 and 12, the direct differences in both the magnitude and orientation of the gradient between any two time periods can be determined for every estimator. Cumulative distributions of the absolute values of the differences in the orientation and magnitude of the gradient between August 2000 and August 2003 are presented in Figure 13 for all three sets of estimators. The absolute values of the differences are shown in order to better display the range of variation.

The distribution of the absolute values of the differences in the magnitude of the gradient (Figure 13, top) shows that the vast majority of the differences are less than the value of the regional gradient ($1.6E-03$). Roughly 95 percent of the differences in the orientation are less than 10 degrees between the two time periods. As the shape and RHME constraints are applied to the estimators, the variance of the distributions decreases. This is due largely to the estimators that produce the extreme differences being removed from the data set, although some very large differences do remain even after both criteria are applied. The root cause of these differences can now be examined in the field. In the future, the results produced by the three-point estimation calculations could be used to determine if the extreme differences in magnitude and/or orientation are all from estimators that have one or two wells in common. If so, changes in monitoring practices at these wells, or local changes in the Culebra hydrology such as nearby potentially leaky brine injection wells can be identified.

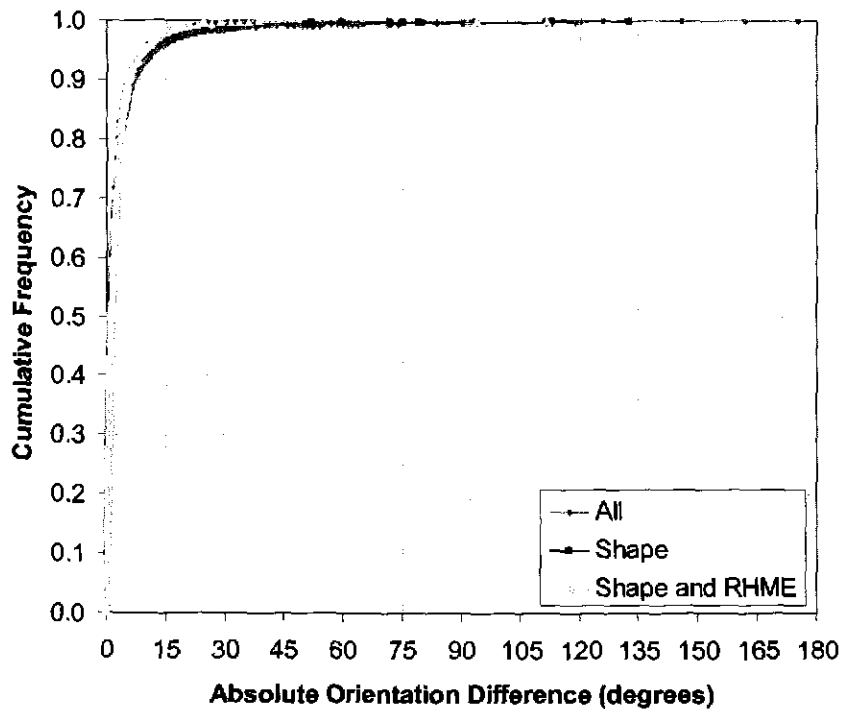
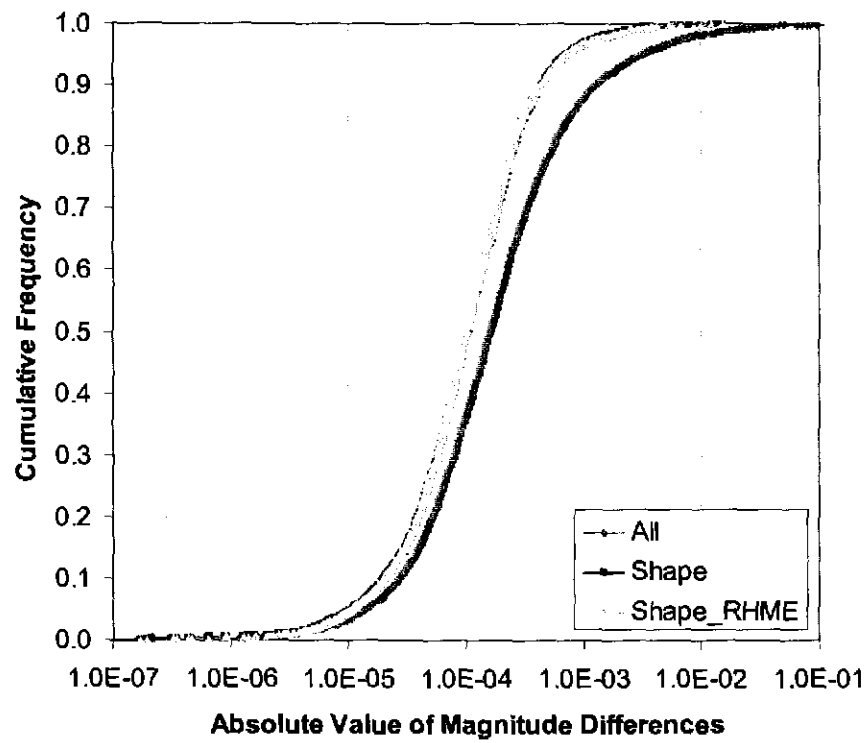


Figure 13. Cumulative distributions of absolute differences of the magnitude (top) and orientation (bottom) of the hydraulic gradient between the 2000 and 2003 measurements as calculated using the three sets of local gradient estimators.

3.5 Application 2: Long-Term Monitoring Network Design

There are two questions to be answered in the design of a long-term monitoring network that is an extension of an existing monitoring network: 1) Can any wells be removed from the current network with no, or very little, impact on the ability of the network to detect and characterize changes in the hydraulic gradient? and 2) Where are the best locations to add wells to the network in order to increase the ability of the network to detect and characterize changes in the gradient? Both of these questions are examined using the three-point estimators.

The August 2003 head data, second from right column of Table 3, are used for the well removal and addition calculations as they represent the more recent set of monitoring network observations. The magnitude and orientation of the regional gradient as calculated by the best-fit method for the August 2003 heads (Table 8, bottom row) are used in the calculation of the RMHE for the well removal and addition study. The shape and RMHE constraints used previously are also applied to the well removal and addition calculations.

3.5.1 Removal of Existing Monitoring Wells

Wells can be removed one at a time from an existing network and the resulting number of acceptable three-point estimators can be determined from the remaining wells. This calculation has been completed three times and the results are in Tables 9, 10, and 11. The three calculations are done with the original 30-well network, a 28-well network where WIPP-12 and WIPP-22 have been removed, and a 26-well network where WIPP-12, WIPP-22, H-12, and P-17 have been removed. The same constraints on estimator shape and RHME as discussed in the previous section are also applied to these calculations. The August 2003 observations result in 1879 acceptable estimators. This number is slightly different from the 1861 acceptable estimators calculated above using the average of the 2000 and 2003 regional gradient values.

If there were no constraints on the shape or RMHE of the estimators, 30 wells would produce 4060 unique three-well combinations. Removal of a single well would decrease this number to 3654 (Equation 12), a drop of 406 three-well combinations. Therefore, the maximum possible reduction in the number of acceptable triangles is 406. For this maximum reduction to occur, the removed well would have to have been included in every acceptable estimator, which will certainly not be the case. The corresponding number for the 28-well case is 3276 possible well combinations, and removal of a single well would decrease the possible number of combinations to 2925, a drop of 351 possible combinations. The 26-well network can produce 2600 possible combinations of three wells, and removing a single well from this network decreases this possible amount by 300 to 2300.

Results of the well removal calculations are shown in Tables 9, 10, and 11. For the case of the original 30-well network, a total of 23 different wells are removed, one at a time, and the remaining numbers of acceptable estimators are determined. Not all of the original 30 wells are removed for these calculations. The WQSP wells must remain in the network because they also serve as the water quality monitoring network. Additionally, one of the wells on the H-19 hydropad will likely remain in the gradient monitoring network for the foreseeable future because of the longevity of the fiberglass casing used at that location. The minimum drop in the acceptable number of estimators when one well is removed is 113 and the maximum decrease is 261 combinations (Table 9). These values are -5.0 and -12.9 percent decreases from the number

of acceptable estimators when all 30 wells are used in the calculations. Across all wells, removal of a single well results in decreases in the number of estimators that are between 28 and 64 percent of the theoretically possible maximum decrease.

The results in Table 9 indicate that removal of either the ERDA-9 or WIPP-21 wells would have the smallest impact on the gradient-monitoring network. Removal of the WIPP-19 or WIPP-22 wells would have only slightly greater impacts on the gradient monitoring network. Wells that would have the greatest impact on the gradient-monitoring network if they were removed are WIPP-25 and H-7b2, with H-5b, H-12, and WIPP-30 having only slightly less impact on the network.

Table 9. Decrease in the number of acceptable local gradient estimators due to removing one well at a time from the full (30-well) monitoring network

Removed Well	Remaining Acceptable Estimators	Absolute Decrease	Percent Decrease	Percent of Maximum Decrease
AEC-7	1650	229	-11.2	56.4
DOE-1	1683	196	-9.4	48.3
ERDA-9	1765	114	-5.1	28.1
H-2b2	1722	157	-7.4	38.7
H-3b2	1736	143	-6.6	35.2
H-4b	1644	235	-11.5	57.9
H-5b	1625	254	-12.5	62.6
H-6b	1650	229	-11.2	56.4
H-7b2	1620	259	-12.8	63.8
H-9b/c	1696	183	-8.7	45.1
H-10b/c	1672	207	-10.0	51.0
H-11b4	1665	214	-10.4	52.7
H-12	1634	245	-12.0	60.3
H-17	1642	237	-11.6	58.4
P-17	1653	226	-11.0	55.7
WIPP-12	1737	142	-6.6	35.0
WIPP-13	1696	183	-8.7	45.1
WIPP-19	1752	127	-5.8	31.3
WIPP-21	1766	113	-5.0	27.8
WIPP-22	1757	122	-5.5	30.0
WIPP-25	1618	261	-12.9	64.3
WIPP-26	1650	229	-11.2	56.4
WIPP-30	1634	245	-12.0	60.3

For the calculations done when WIPP-12 and WIPP-22 are already removed from the network, the minimum drop in the acceptable number of estimators when one well is removed is 111 and the maximum decrease is 233 estimators (Table 10). These values are -5.9 and -13.4 percent decreases from the number of acceptable estimators when the base case of 28 wells is used in the calculations. Across all wells, removal of a single well results in decreases in the number of estimators that are between 32 and 66 percent of the theoretically possible maximum decrease.

The results in Table 10 indicate that if WIPP-12 and WIPP-22 are removed from the network, then subsequent removal of either the ERDA-9 or WIPP-21 wells would have the smallest impact on the gradient-monitoring network. Removal of the WIPP-19 or H-3b2 wells would have only slightly greater impacts on the gradient monitoring network. Wells that would have the greatest impact on the gradient-monitoring network if they were removed are WIPP-25, H-5b and H-7b2, with H-12 and WIPP-30 having only slightly less impact on the network. All of these results are consistent with the results from removing wells from the original 30-well network.

Table 10. Decrease in the number of acceptable local gradient estimators due to removing one well at a time from the 28-well monitoring network where WIPP-12 and WIPP-22 have already been removed.

Removed Well	Remaining Acceptable Estimators	Absolute Decrease	Percent Decrease	Percent of Maximum Decrease
AEC-7	1414	202	-11.5	57.5
DOE-1	1448	168	-9.4	47.9
ERDA-9	1505	111	-5.9	31.6
H-2b2	1473	143	-7.8	40.7
H-3b2	1487	129	-7.0	36.8
H-4b	1414	202	-11.5	57.5
H-5b	1390	226	-13.0	64.4
H-6b	1410	206	-11.7	58.7
H-7b2	1385	231	-13.3	65.8
H-9b/c	1448	168	-9.4	47.9
H-10b/c	1432	184	-10.4	52.4
H-11b4	1433	183	-10.3	52.1
H-12	1397	219	-12.6	62.4
H-17	1410	206	-11.7	58.7
P-17	1416	200	-11.4	57.0
WIPP-13	1440	176	-9.9	50.1
WIPP-19	1491	125	-6.7	35.6
WIPP-21	1503	113	-6.0	32.2
WIPP-25	1383	233	-13.4	66.4
WIPP-26	1409	207	-11.8	59.0
WIPP-30	1401	215	-12.3	61.3

For the calculations done when four wells are removed from the original network (WIPP-12, WIPP-22, H-12 and P-17), the minimum drop in the acceptable number of estimators when one subsequent well is removed is 82 and the maximum decrease is 191 wells (Table 11). These values are -5.7 and -14.7 percent decreases from the number of acceptable estimators when the base case of 26 wells was used in the calculations. Across all wells, removal of a single well results in decreases in the number of estimators that are between 27 and 64 percent of the theoretically possible maximum decrease.

The results in Table 11 indicate that if WIPP-12, WIPP-22, H-12, and P-17 are removed from the network, then subsequent removal of either the ERDA-9 or WIPP-21 wells would have the smallest impact on the gradient-monitoring network. Removal of the WIPP-19 or H-3b2 wells would have only slightly greater impacts on the gradient monitoring network. Wells that would have the greatest impact on the gradient-monitoring network if they were removed are WIPP-25, H-5b, H-7b2, H-17, and WIPP-30. These results are consistent with the previous results shown in Tables 9 and 10.

In all three cases, ERDA-9, WIPP-21, WIPP-19, and H-3b2 are the least important wells and WIPP-25, WIPP-30, H-5b, and H-7b2 are the most important wells when wells are removed one at a time from the different base case networks. The results also indicate that H-12 would be an important well to replace should it be lost from service.

Table 11. Decrease in the number of acceptable local gradient estimators due to removing one well at a time from the 26-well monitoring network where WIPP-12, WIPP-22, H-12, and P-17 have already been removed.

Removed Well	Remaining Acceptable Estimators	Absolute Decrease	Percent Decrease	Percent of Maximum Decrease
AEC-7	1052	164	-12.5	54.7
DOE-1	1076	140	-10.5	46.7
ERDA-9	1134	82	-5.7	27.3
H-2b2	1104	112	-8.2	37.3
H-3b2	1112	104	-7.6	34.7
H-4b	1046	170	-13.0	56.7
H-5b	1032	184	-14.1	61.3
H-6b	1038	178	-13.6	59.3
H-7b2	1028	188	-14.5	62.7
H-9b/c	1074	142	-10.7	47.3
H-10b/c	1066	150	-11.3	50.0
H-11b4	1058	158	-12.0	52.7
H-17	1029	187	-14.4	62.3
WIPP-13	1064	152	-11.5	50.7
WIPP-19	1117	99	-7.1	33.0
WIPP-21	1127	89	-6.3	29.7
WIPP-25	1025	191	-14.7	63.7
WIPP-26	1049	167	-12.7	55.7
WIPP-30	1032	184	-14.1	61.3

3.5.2 Addition of New Monitoring Wells

To determine the best locations for new wells, an algorithm was developed to examine the number of acceptable estimators that would exist given the addition of a new well at any location within the domain. This calculation is conducted by locating a new well at every cell center on a 100×100 m² grid and then determining the number of acceptable estimators resulting from the insertion of this new well. Because wells do not actually exist in these locations, the average head resulting from 100 calibrated stochastic transmissivity fields (McKenna and Hart, 2003; Beauheim, 2003) is used as the “measured” head at each potential well location. The 100-meter grid used to define the potential well locations corresponds to the groundwater flow model grid used in the calibration of the transmissivity fields (see Table 1). Again, the number of acceptable estimators for the August 2003 data is 1879.

The addition of a new well to the existing monitoring network can only increase the number of acceptable estimators. Without the shape or RHME criteria, the maximum possible number of estimators from 30 wells is 4060 (Equation 12). The maximum possible number of estimators from 31 wells is 4495, an increase of 435. If the additional well can be placed such that all additional estimators created from that well meet both criteria, then the increase in the number of acceptable estimators will be 435. This number serves as an upper bound on the possible number of new estimators.

On average, addition of a new well to the Culebra network creates a total of 2137 acceptable three-point estimators, or an increase of 258 (14 percent), over the 1879 estimators created from the existing network. The maximum number of acceptable estimators constructed from the addition of a new well is 2195, or an increase of 316 (17 percent) over the existing well network. The minimum number of acceptable estimators created with the addition of a new well is 1966, an increase of 87 (5 percent) over the current network. These increases range from roughly 20 to 73 percent of the maximum possible increase in the number of estimators of 435.

The results of the well-addition calculations are shown as a map in Figure 14. Locations where the addition of a well will increase the number of acceptable estimators the most are generally in the areas surrounding the outside of the WIPP site. A well added in these areas can take advantage of the large number of existing wells within the WIPP site to create estimators that meet both the shape and RHME criteria. Exceptions to these areas are locations between the WIPP site and locations where wells already exist. The areas of highest return do not extend all the way to the edges of the domain because either the no-flow region restricts the number of triangles that can be created or, in the NE corner of the domain the addition of a single new well is not enough to create a large number of new estimators. The problem is not as great in the SE corner of the domain as there are already existing wells closer to that corner of the domain. An additional well within the WIPP site will produce the smallest increase in the number of acceptable estimators as this area already has a large number of wells and the majority of the estimators created by an additional well within this area will not be large enough to achieve the necessary head drop to meet the RMHE criterion.

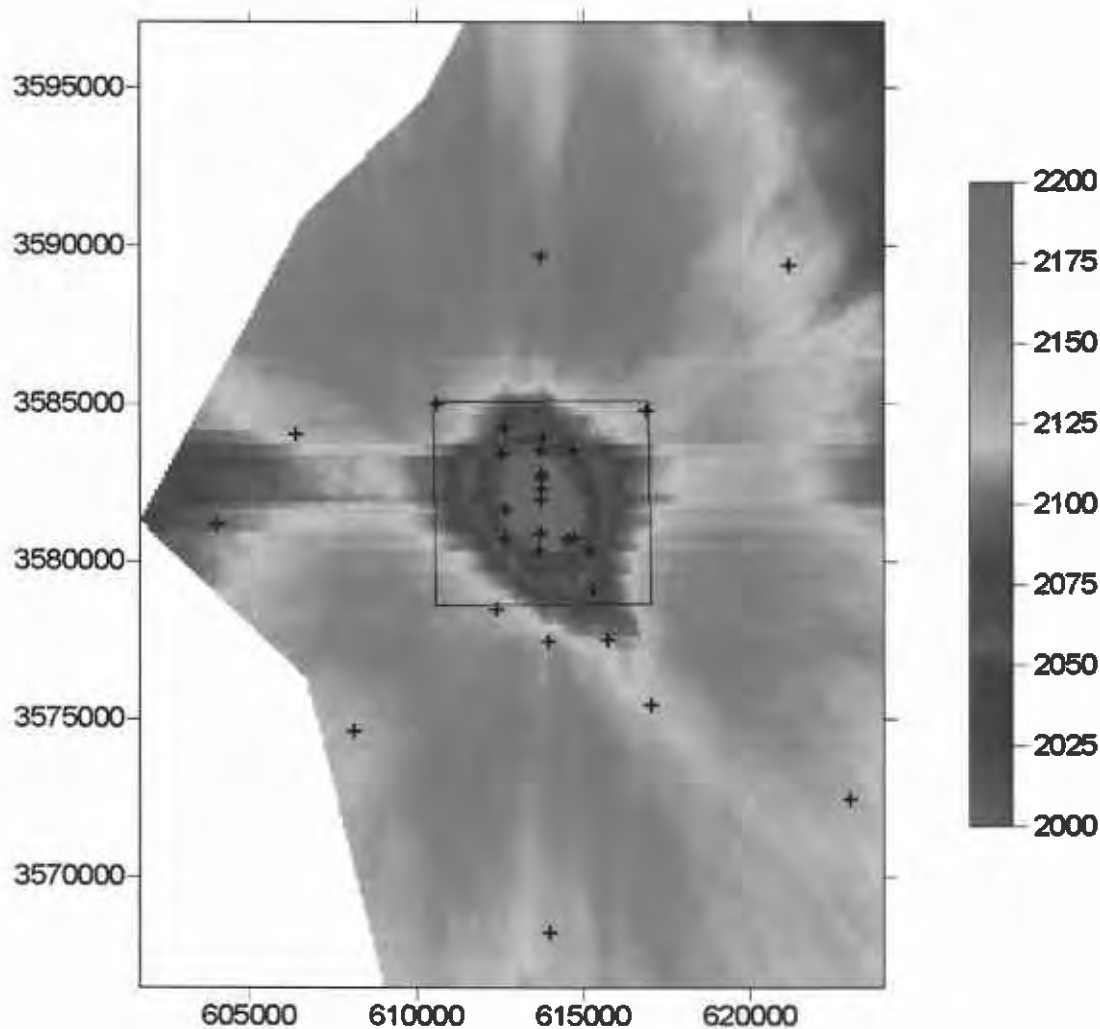


Figure 14. Number of acceptable local gradient estimators for a single new well placed at any location within the domain. The current network produces 1879 acceptable local gradient estimators. The black crosses show the existing 30-well monitoring network. The contour is 25 estimators and the contour levels correspond to the levels identified in the color scale.

3.6 Local Gradient Estimation Summary

The ability of local gradient estimators consisting of three wells at unique locations to accurately and precisely estimate the magnitude and orientation of the hydraulic gradient was examined with respect to the RHME, the triangle shape, and the orientation of the hydraulic gradient relative to the orientation of the three-point estimator. Head measurement errors were simulated using Monte Carlo simulation and the results show that the unbiased measurement errors produce unbiased (accurate) estimates of both the orientation and magnitude of the hydraulic gradient. As would be expected, the precision of the estimated magnitude and orientation decreases linearly with increasing measurement error, with the rate of decrease in the precision

for the orientation estimates being roughly half of that for the magnitude estimates. The measurement error can be cast as a proportion of the expected head drop across any three-point estimator and is called the RHME. Across eleven different isosceles triangles all with the same size (area) but covering a broad range of shapes (base to height ratios) those triangles with base to height ratios between 0.5 and 5.0 produced the most precise estimates of the magnitude and orientation of the hydraulic gradient for four different levels of RHME.

Two criteria for selection of acceptable three-point estimators were developed from the results of the Monte Carlo simulations: 1) Triangles need to be large enough to allow for a RHME of 0.02 or less; and 2) Triangles must have base to height ratios between 0.5 and 5.0. These two criteria were applied to the existing Culebra head monitoring network in the vicinity of the WIPP site. Application of these two criteria to the three-point estimators in the Culebra results in 1879 acceptable estimators relative to a total of 4060 possible estimators. Application of these criteria reduces the range of estimated hydraulic gradient magnitudes by at least an order of magnitude and significantly changes the distribution of estimated orientations relative to when all possible three-point estimators are used to make the estimates. These results indicate that estimator size is not necessarily a good indication of the accuracy of the magnitude and orientation estimates provided by the three-point estimator and that accurate estimates can be obtained from smaller triangles.

The three-point estimators that meet the RHME and shape criteria are used in two different applications of monitoring network design for the Culebra. Changes in the estimated magnitudes and orientations of the local gradients over a three-year time period range from essentially zero to $1\text{E}-01$ and 170° respectively, although the majority of the magnitude and orientation differences are less than $1.0\text{E}-03$ and 10° , respectively. In a future analysis, the estimators responsible for the largest changes in magnitude and orientation could be identified and the wells comprising those estimators could be examined for the causes of these large changes. The possibility of doing this type of analysis points out the higher level of understanding that can be gained from monitoring gradients rather than just monitoring heads. The comparison of the 2000 and 2003 heads shows a general rise in head during this time (Figure 2). The comparison of the 2000 and 2003 estimated magnitudes and orientations (Figures 10 through 13) uses the same 30 data points as used to detect changes in heads, but provides a much richer picture of how flow conditions in the aquifer are changing during this time period relative to just examining head changes.

The second application of the three-point estimators to monitoring network design determined the two sets of existing wells that had the least and the greatest impact on the ability of the network to estimate the magnitude and orientation of the hydraulic gradient. The number of acceptable three-point estimators lost due to removal of a single well serves as a measure of the reduction in the ability of the network to make accurate estimates of the magnitude and orientation of the gradient. Three-point estimators have not been used previously for this type of analysis and the results indicate that three-point estimators do an excellent job of preserving the wells that uniquely provide coverage in certain areas and also in identifying wells that provide redundant coverage. This approach demonstrated here can readily complement the more commonly used variance reduction and data-worth approaches to long-term monitoring network design. The decrease in the number of acceptable estimators due to the removal of a single well

ranges between 5 and 13 percent of the current number of acceptable estimators depending on which well is removed. A similar approach was used to determine the locations where an additional well would have the greatest increase in the number of acceptable three-point estimators. These calculations were done by placing a new well at every location on a 100×100 m² grid within the calculation domain and then assigning a head to the new well location that is equal to the average head from an ensemble of previously calibrated groundwater flow models. The percent increase in the number of acceptable three-point estimators due to a single new well relative to the existing network ranges from 5 to 17 percent with an average increase of 14 percent. Mapping these results across the calculation domain shows that the best places for a new well are in a nearly continuous circular band outside of the WIPP site with the areas within the WIPP site producing the lowest increase in the number of acceptable three-point estimators. The calculations for both existing well removal and the addition of a new well are done for the removal/addition of a single well. Further calculations for the removal/addition of combinations of two or more wells can be completed, but the possible combinations of well locations, especially for the addition problem, are essentially infinite and other well placement criteria would need to be used to constrain these calculations.

3.7 Assumption of Homogeneity

An implicit assumption in the use of the local gradient estimators to determine the orientation and magnitude of the hydraulic gradient is that the aquifer material within any three-point estimator (triangle) is homogeneous. For any aquifer, this assumption will not be met. Previous work (e.g., Mizell, 1980) has shown that when the size of the triangle is much larger or much smaller than the correlation length scale of the transmissivity, it is possible to invoke the homogeneous assumption.

The homogeneity assumption was evaluated by selecting a series of 1879 triangles for which the magnitude and orientation of the gradient could be evaluated. These 1879 triangles are a subset of the total possible 4060 triangles that meet both the shape and RHME constraints (see Section 3.4). For each triangle, the head estimates are available at each of 100 calibrated transmissivity fields (Hart and McKenna, 2003; subdirectories below /h/WIPPcvs/trans/runs/). These heads can be used as input to a three-point estimator to estimate the magnitude and orientation of the gradient 100 times for each triangle (187,900 total estimates of orientation and magnitude). This ensemble of estimates can be compared directly with the estimates made from the field observations of head using those same 1879 three-point estimators. Comparison of the estimates of magnitude and orientation based on measured and model-generated heads are shown in Figure 15. This comparison is made using just the mean results of all estimators as calculated across all 100 realizations.

The comparison in Figure 15 shows that there is considerably less variation in the estimates of both magnitude and orientation when the model-generated heads are used versus those measured in the field. For example, considerably fewer magnitudes lie outside the 0.01 contour for the model-generated heads (right image) compared to the field-based estimates (left image). From Figure 15, it is not possible to determine if there is a significant change in the mean orientation estimate between the field- and model-based results. The decrease in variation from the field- to the model-based estimates can be due to incorrect representation of the true heterogeneity within

the model as well as the averaging process. It is not possible to determine in exactly what way the model incorrectly represents the heterogeneity, but certainly the use of $100 \times 100 \text{ m}^2$ cells in the model will smooth out some of the true heterogeneity.

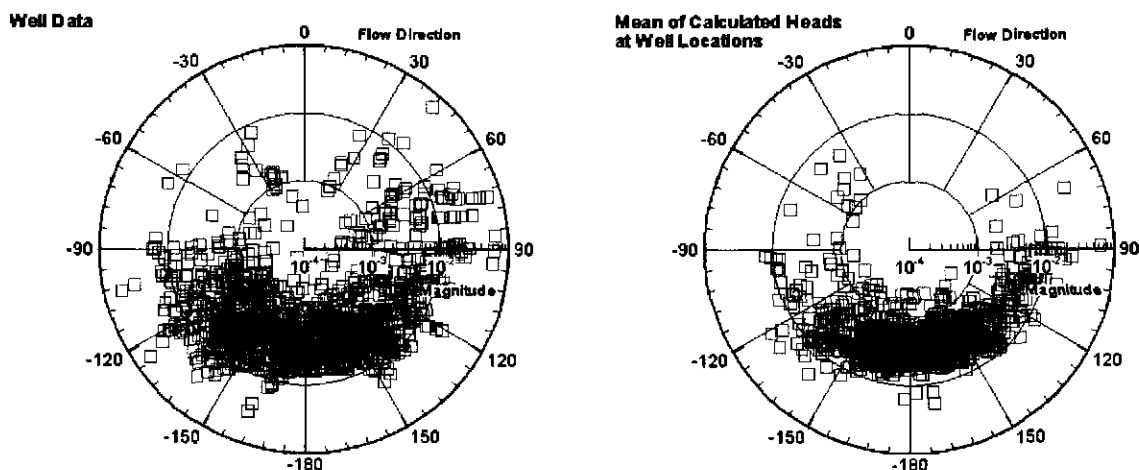


Figure 15. Polar coordinate plots comparing the estimated orientation and magnitude of the hydraulic gradient based on field measurements (left image) and model-generated heads (right image). The magnitudes are shown on log₁₀ scale.

The question of the effect of heterogeneity on the ability of local gradient estimators to accurately estimate the hydraulic gradient is examined by discretizing each of the three-point estimators as defined by the wells into a number of smaller triangles. For this work, each triangle defined by the wells, “well triangle”, was subdivided into smaller triangles, “grid triangles”, based on the underlying 100-meter grid spacing. This discretization is shown for an example triangle in Figure 16. Each grid triangle is an isosceles triangle that fits in a 3×3 set of grid cells. For the example in Figure 16, 221 grid triangles fit within the example well triangle. Details on the calculation and assignment of the different triangle sizes are given in Appendix 4.

The grid triangles are small enough such that they are only a fraction, less than or equal to 0.20, of the transmissivity correlation length calculated by McKenna and Hart (2003) and therefore should contain relatively homogeneous regions of the aquifer. The same local gradient estimation techniques used for the data at the wells are also applied to the calculated heads at each of the vertices of each smaller triangle. An average hydraulic gradient and orientation as calculated across all grid triangles can then be compared to the same quantities as calculated using the well triangle that contains all grid triangles. These averages are calculated as a straight linear average and as a flux-weighted average where the total flux through each grid triangle relative to the flux through the well triangle determines its weight in the average. If the average magnitude and orientation of the gradient as calculated over all grid triangles is consistent with the larger scale estimate made over the well triangle, then the triangles defined by the three wells

are reasonable estimators of the composite gradient within them and heterogeneity becomes a second-order effect.

A complication of this comparison approach is that there is not a single groundwater flow model result from which to obtain head values from the grid triangles. There are 100 calibrated head fields. Therefore, every one of the 1879 well triangles will have a distribution of 100 average gradients as calculated over all of the grid triangles contained within that well triangle. These distributions are calculated using the **Median_HeadGrad** program (Appendix 5) and compared to the results of the gradient estimates calculated using the field observations in Figure 17 (magnitudes) and 18 (orientations).

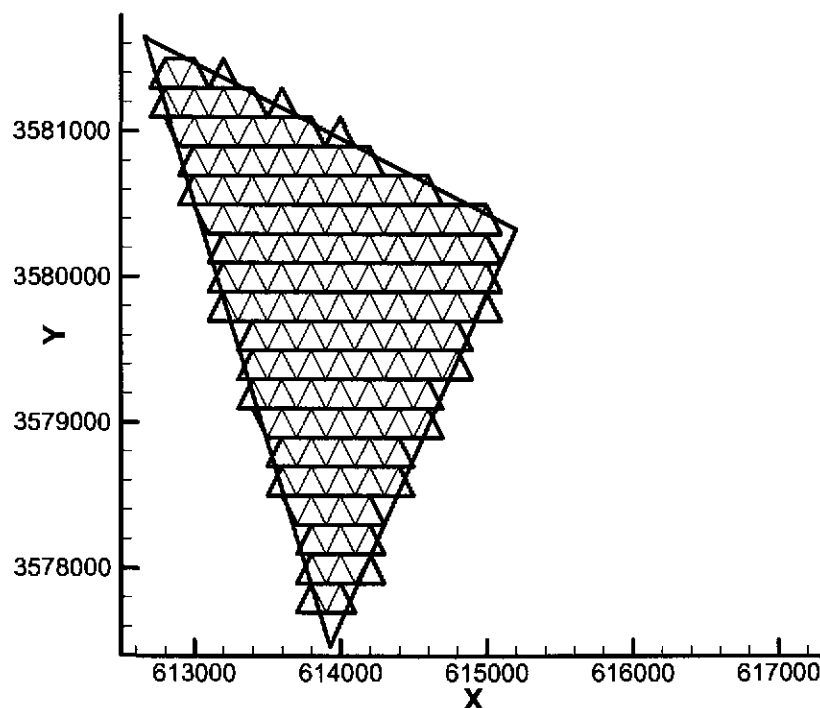


Figure 16. Example of discretizing a large triangle defined by wells with a number of smaller isosceles triangles defined using the underlying 100-meter grid spacing.

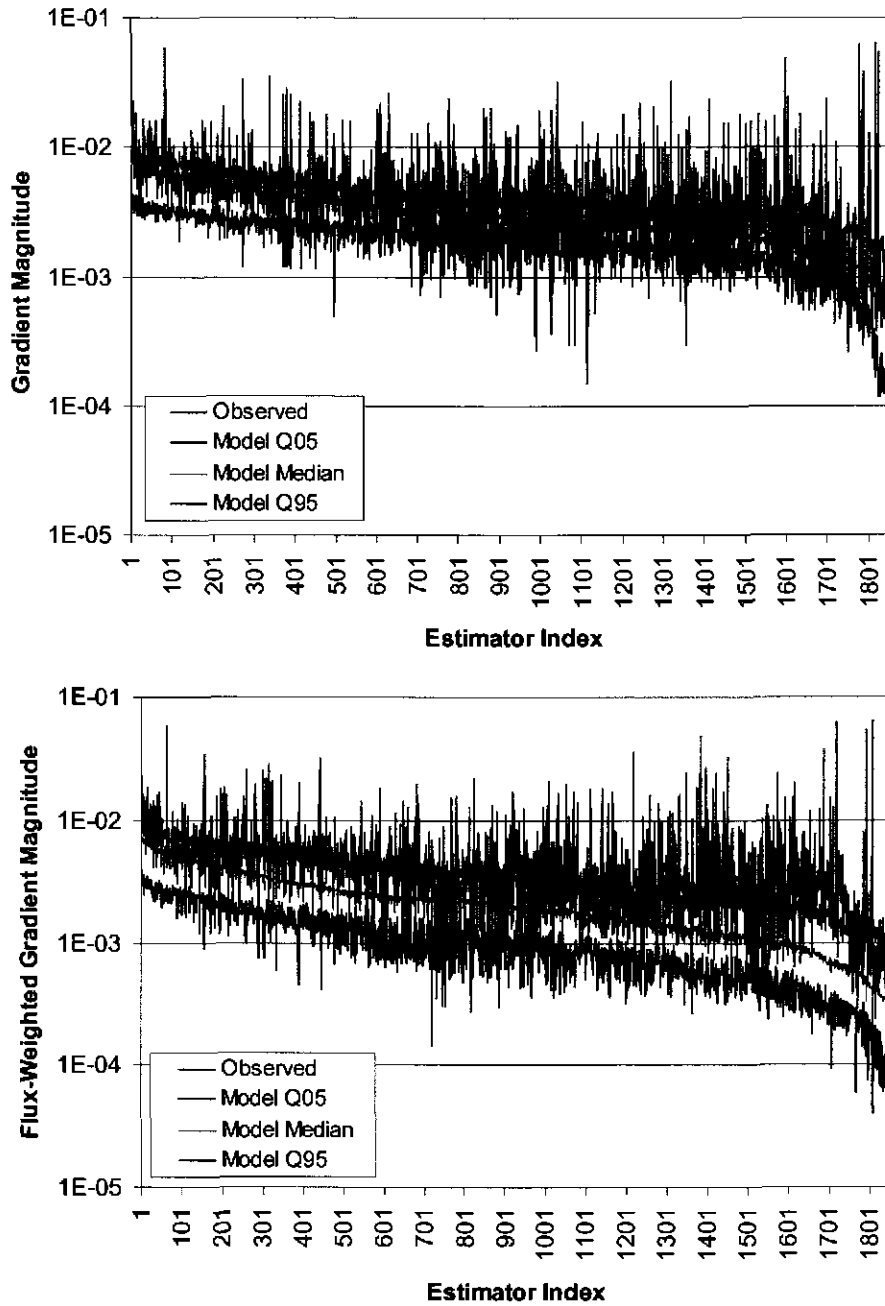


Figure 17. Estimates of the magnitude of the hydraulic gradient from the observed head values at the wells and as unweighted (top) and flux-weighted averages (bottom) of the grid triangles within each well triangle. The results are sorted by the mean values (not shown) and are arranged from high to low magnitude and then each result is assigned an index for plotting.

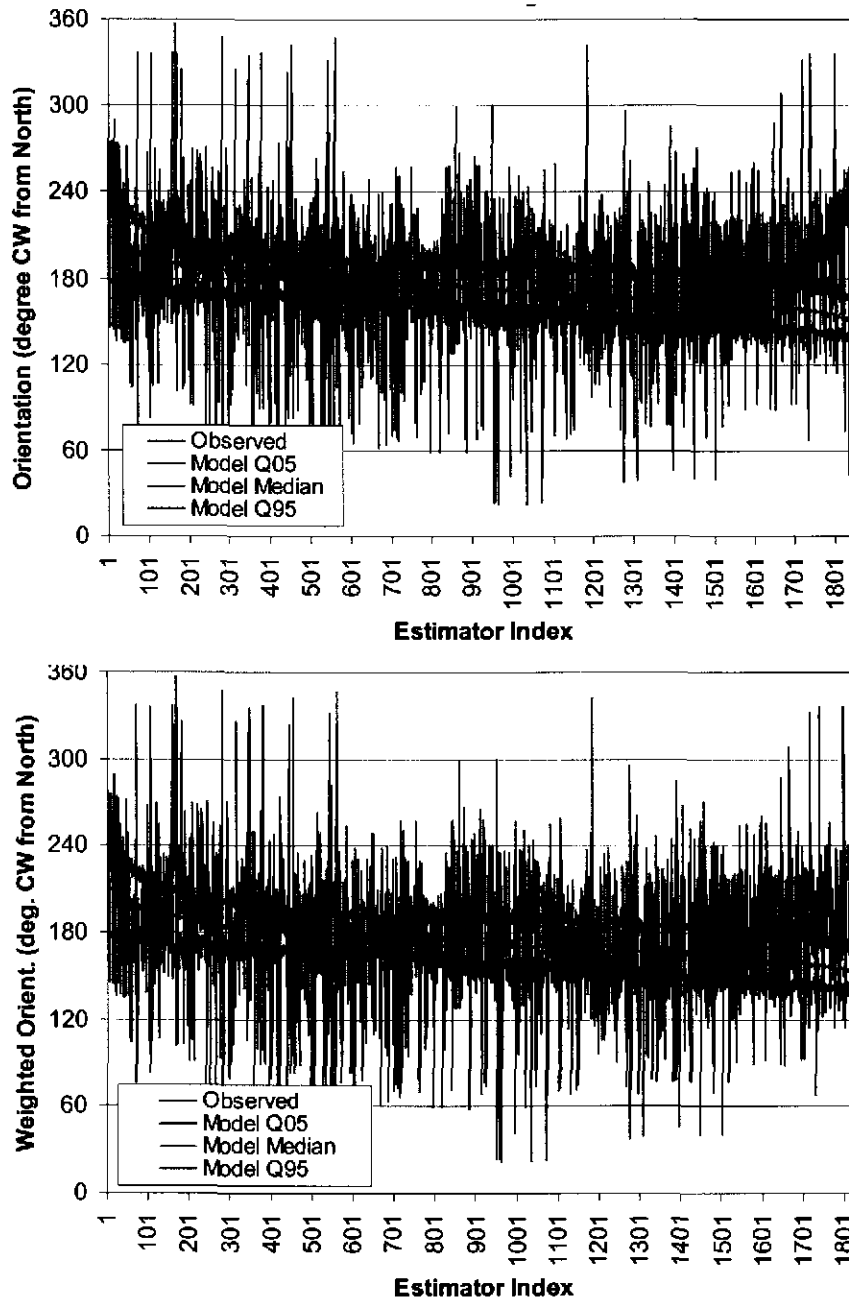


Figure 18. Estimates of the orientation of the hydraulic gradient from the observed heads values at the wells and as unweighted (top) and flux-weighted (bottom) averages of the grid triangles within each well triangle. The different estimators are assigned indices for plotting.

Figures 17 and 18 show several interesting patterns. For both the magnitude and orientation estimates, the observed head data produce considerably more variation in the estimates than are seen in the model output. This result is due to the model producing estimates with less variability for any set of measurements as seen in Figure 15 and is also due to the distributions shown in Figures 17 and 18 being distributions of averages across many small triangles not distributions of estimates made from individual sets of observations. The model effect and the

averaging both act to reduce the variation in the estimated values. The variation of the gradient estimates from the observed data is due to measurement error and heterogeneity. As seen in Figure 15, the numerical model smoothes the estimates of the magnitude and orientation relative to estimates made directly from the field observations.

The choice of averaging algorithm for the grid triangles makes a large difference in the resulting estimates of the magnitude of the gradient (note the decrease in estimated magnitudes when flux-weighted averaging is used (Figure 17)), but has little effect on the orientation estimates (Figure 18). Using the linear (unweighted) average produces relatively unbiased estimates of the magnitude while using the flux-weighted averages shifts the model estimates to below those of the field-based estimates. Prior to this set of calculations, the importance of incorporating the flux into the averaging process was unknown and these results confirm that a simple unweighted average of the smaller, grid, triangles provides the best estimates of the gradient magnitudes made from the observed data. For either type of averaging, the orientation estimates produce relatively unbiased estimates of the orientation obtained from the field observations.

A specific question to be addressed in this analysis is whether or not there is an estimator size beyond which a triangle becomes so large that it cannot provide reliable estimates of the hydraulic gradient on the WIPP site. This question cannot be answered directly as the true gradient is unknown. However, the relationship between the average gradient estimated from the small triangles enclosed by a well triangle and the gradient defined by the observed heads can be determined. If this relationship is a strong function of estimator size, then there may be a point at which an estimator becomes so large as to no longer provide an estimate of the gradient consistent with the average calculated from the triangles enclosed within that estimator. The difference between the median value of the average magnitude and orientation of each estimator as determined by all grid triangles within the larger well triangle and the estimates of the magnitude and orientation as defined by the well data are shown as a function of estimator size in Figures 19 and 20.

The major result of this analysis as shown in Figures 19 and 20 is that the differences in the magnitude and orientation of the hydraulic gradient as estimated from averages of modeled heads in smaller internal triangles or from the observed head data at the wells are only a general function of estimator size. In both Figures 19 and 20, trends of decreasing differences with increasing estimator size can be identified. For example, absolute differences of magnitude above $1.0E-02$ only occur for estimators smaller than $1.0E+07 \text{ m}^2$ in the unweighted case (Figure 19, top image) and slightly less than $1.0E+07 \text{ m}^2$ for the weighted case. In general, the larger the estimator, the less difference there is between the gradient estimated from the observed heads and the gradient calculated as an average of all the small, relatively homogeneous regions of the aquifer within the estimator. However, the smallest absolute differences of all, those of $1.0E-04$ or less, occur in a relatively uniform band between estimator sizes of roughly $8.0E+05$ to $1.0E+08 \text{ m}^2$.

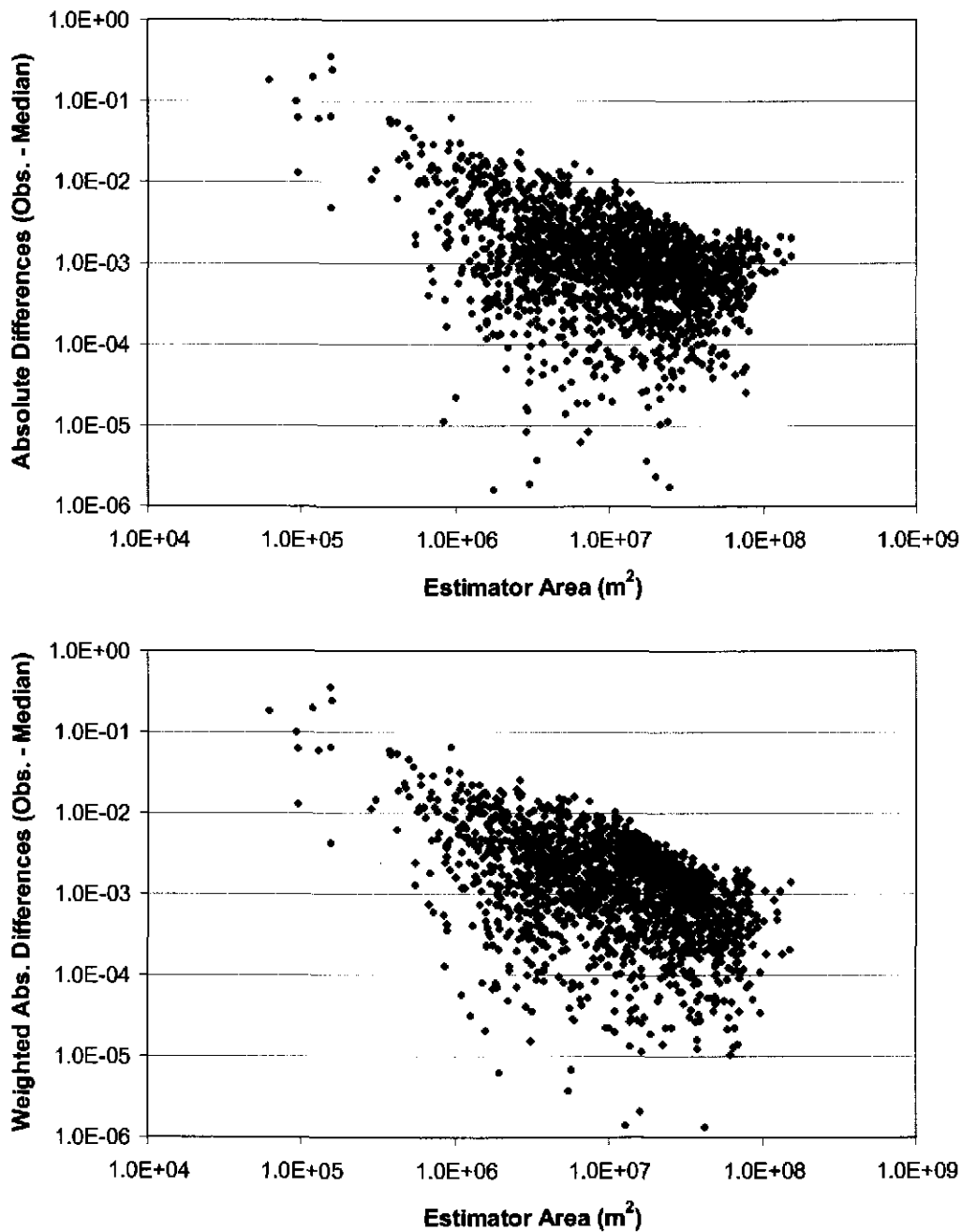


Figure 19. Difference between the magnitude of the hydraulic gradient as estimated from the well observations and the median average estimated magnitude across 100 realizations as a function of estimator size. The results of the unweighted averaging are shown in the top image and the flux-weighted averaging results are shown in the lower image.

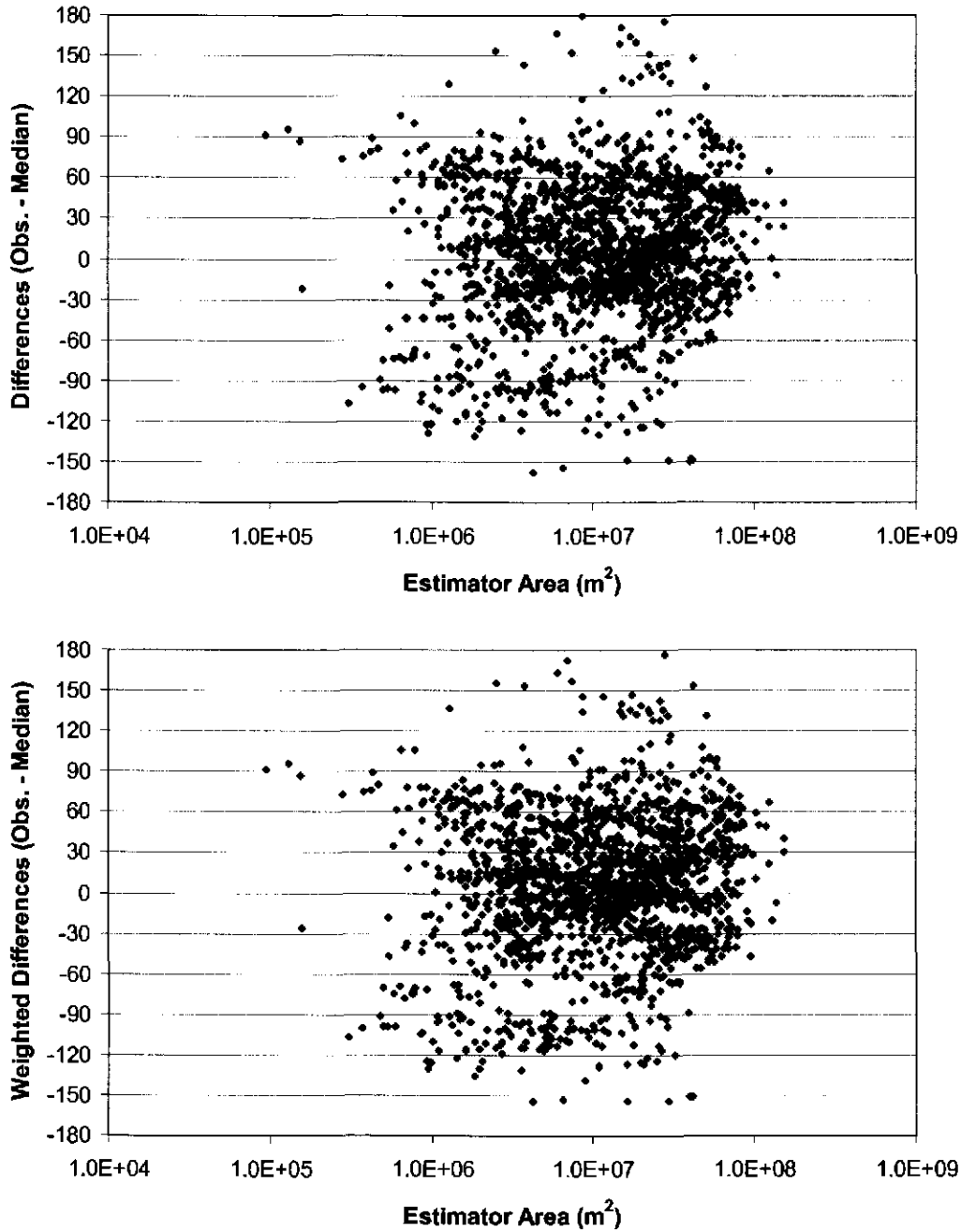


Figure 20. Difference between the orientation of the hydraulic gradient as estimated from the well observations and the median average estimated orientation across 100 realizations as a function of estimator size. The results of the unweighted averaging are shown in the top image and the flux-weighted averaging results are shown in the lower image.

In order to monitor the gradient across the WIPP site, three-point estimators could be used that are, at the minimum end, contained completely within the WIPP site and at the maximum size extend beyond the WIPP site boundaries. As a frame of reference, a three point estimator using wells at the center of the panel area and the two southern corners of the WIPP site would have an area of roughly one-fourth the WIPP site or $1.05E+07 \text{ m}^2$. An estimator of this size would fall nearly in the middle of the range of lowest values of absolute differences in observed vs. modeled gradient magnitudes (Figure 19). Using Figure 19 as a guide, the estimator could be a factor of four to five times larger than this and still provide consistent results between the modeled and observed magnitudes. Estimators smaller than this can provide consistency between modeled and observed gradient magnitudes, but the maximum difference between modeled and observed results increases as the estimator size decreases. This size of an estimator corresponds to a wide range of differences between modeled and observed orientations (Figure 20). Increasing the size of the estimator beyond that of one-half the WIPP site decreases the differences between modeled and observed orientations (Figure 20).

Given the results in Figures 19 and 20, the upper limit on estimator size appears to be approximately $1E+08 \text{ m}^2$, or two and half times the size of the WIPP site. The lower limit, using a absolute difference of $1.0E-02$ in the unweighted gradient magnitudes (Figure 19, upper image) as a threshold, is approximately $5.0E+06 \text{ m}^2$, or 8 times smaller than the WIPP site. Estimators within this range of sizes that are either fully contained within the WIPP site boundaries or contain a large portion of the WIPP site within the three wells can be expected to provide good estimates of the magnitude of the gradient across the WIPP site. Based on these same calculations, good estimates of the orientation of the gradient can be made with estimators that are the size of the WIPP site, $4.3E+07 \text{ m}^2$, and larger.

These calculations show that model-based estimates of the hydraulic gradient are considerably less variable than those made with field data. While heterogeneity plays a role in the amount of variability from the field estimates, in general across all triangles, the correct orientation and magnitude of the hydraulic gradient can be determined. These calculations show that the estimate of the hydraulic gradient as determined from three wells in a triangle is a good estimate of the gradient when calculated as an average of many small local gradient estimates across relatively homogeneous domains within that larger triangle. In other words, the average of a number of estimates on small, relatively homogeneous pieces of the aquifer is well approximated by the larger scale calculation done over the heterogeneous piece of aquifer. The larger the estimator, the better the degree of *approximation*.

From the opposite perspective, if the monitoring goal is to accurately determine the local-scale gradients over a smaller portion of the Culebra, such as the southern end of the WIPP site, large triangles will not be capable of determining this local scale variability in magnitude and orientation. Figures 19 and 20 show that for a triangle of $1.05E+07 \text{ m}^2$, one-fourth of the WIPP site area, there is a three order of magnitude variation in the gradient magnitude and a nearly 360 degree range in orientation. Not all of this variability will occur within the southern end of the WIPP site as there are many triangles of this size throughout the monitoring network, but it can be concluded that the largest triangles will not provide the detail necessary to monitor gradient magnitudes and directions over a portion of the WIPP site.

3.8 Calculation Details

The first set of calculations done in this section was completed to develop a relationship between the absolute head measurement error and the error in the estimated magnitude and orientation of the hydraulic gradient. These calculations are done using the RHME code. The code is tested in the *Monitoring_04\Test_Problems\RHME_test* subdirectory on the CD-ROM that is part of this analysis package. A summary of the test problem and results are included here as Appendix 6. The RHME code is then used to create the data that are the basis for Figure 6. These calculations are done in the *Monitoring_04\RHME_calcs* subdirectory. The final results are contained in the *mserr_####.out* files where #### denotes the value of RHME and are also stored and processed in the *rhme_calcs.xls* file.

The effects of estimator shape and orientation of the gradient on the ability of the estimator to produce accurate estimates of the hydraulic gradient are calculated using the **main** code. The **main** code is tested in the *Monitoring_04\Test_Problems\shape_test* subdirectory and a summary of this testing is included as Appendix 7. The calculations are done in the *Monitoring_04\shape_calcs* subdirectory. For each of the 11 triangle shapes as defined in Figure 7 there is a single input file. The naming convention for the input files is *##cases.txt* where the ## defines the size of the two equal angles in the triangle in degrees. A set of 2000 calculations is done on each of 24 gradient orientations for a specified value of RHME (set as **ERR_TO_DROP** in the main code). Each set of these 48,000 calculations is contained in a single output file and there are a total of 11 output files for each value of RHME, one for each estimator shape. The naming convention for the output files is *mserr##_\$\$\$\$.out* where the ## defines the shape of the triangle as given in Figure 7 and \$\$\$ defines the value of RHME.

The output files are read into a series of **Excel** files, one for each estimator shape, that have the naming convention of *##.xls* where the ## defines the shape of the estimator. Each of these **Excel** files contains all the output for a given triangle shape across all four values of RHME. Additionally, the 95th percentiles of the distributions for each orientation of the gradient and each level of RHME are calculated in a separate worksheet in the file. At the bottom of these worksheets, the mean and median values of the 95th percentile across all 24 directions are calculated. These median values are then summarized for all shapes in the file *Msmt_error_summary.xls*.

The removal of a single well from the network and the recalculation of the number of acceptable three-point estimators are calculated with the **estimate_remove** code. This code is tested on a six and then five well configuration in the *Monitoring_04\Test_Problems\Remove_test* directory. The results of this testing are summarized in Appendix 8. The same code is used for the Culebra calculations in the *Monitoring_04\Removal* subdirectory. Several modifications are made to the *estimate_remove.cpp* file prior to recompiling it and running it on the Culebra problem. These are a change of the loop limit on line 65 from 2 to 24, removal of the comment marks on lines: 128, 134, 135, 136, 142 and 143 to activate the base to height ratio criteria and the RHME criteria for the Y component of the gradient, and addition of the correct input and output file names to the switch statement at the bottom of the file. These changes are readily apparent by comparing the file *estimate_remove.cpp* in both the *Monitoring_04\Test_Problems\Remove_test* and *Monitoring_04\Removal* subdirectories. This same code is used to look at the case of first removing WIPP-12 and WIPP-22 and then every

well in order in the `\Monitoring_04\Removal_3` subdirectory. In order to not modify the code, the input and output file names are kept the same as in the original run in `\Monitoring_04\Removal` subdirectory. Each original input file is modified to remove the lines with the WIPP-12 and WIPP-22 information. The WIPP-12 and WIPP-22 output files are ignored. The number of triangles is the number of lines in each output file minus one for the header line. The same approach is used for the case where the WIPP-12, WIPP-22, H-12, and P-17 wells are removed prior to all other removals. These calculations are in the `\Monitoring_04\Removal_5` subdirectory.

The well addition calculations are made using the `locat` code. This code is tested using a 10×10 grid of potential well locations in the `\Monitoring_04\Test_problems\add_test\` subdirectory. A summary of this testing is included in Appendix 9. The same code is used for the Culebra calculations in the `\Monitoring_04\locat_triangle\` subdirectory with some modifications. Lines 223, 231, 232, 233, 237 and 239 are uncommented and the input and output file names in the switch statement at the bottom of the file are changed to `Aug_2003_wells.in` and `Aug_2003_wells.out`, respectively, for the Culebra calculations. These changes are readily apparent by comparing the `locat.cpp` file in the `\Monitoring_04\Test_problems\add_test\` and `\Monitoring_04\locat_triangle\`.

4.0 Spatial Sensitivity-Based Monitoring

In addition to the variance reduction and local gradient estimator approaches to monitoring network design, a third approach is also examined to directly incorporate uncertainty in the performance assessment into the monitoring network design. These calculations also incorporate recent updates in the geologic conceptual model and the influence of these updates on the spatial distribution of transmissivity within the Culebra. These recent updates in the geologic conceptual model have been used to produce the base transmissivity fields used in this study and are documented by Holt and Yarbrough (2003).

4.1 Background

Spatial sampling design is concerned with locating samples such that variations in state variables and/or material properties can be accurately mapped. In an aquifer, these state variables are typically hydraulic head or contaminant concentration. Traditional approaches to spatial sampling design have focused on either increasing the probability of detection of an object(s) with a prescribed shape and size (Gilbert, 1987) or locating samples to minimize the variance of the prediction error in the sampled property (Burgess et al., 1981; Olea, 1984; Rouhani, 1985; Tuckfield et al., 2001) as was done in the first section of this report. While there are numerous variations on these approaches, they can all be considered as techniques that add samples to minimize the limitations of the current data set where these limitations are defined through easily calculated geometrical and/or spatial covariance-based relationships.

Another approach to the sample optimization involves heavy use of numerical simulation and has been applied mainly to the development of monitoring networks for efficient detection of groundwater contamination downstream of an existing disposal site. Work in this area includes optimization of future well locations based on those that provide maximal data worth (James and Gorelick, 1994; Wagner, 1995), where “worth” is quantified in monetary terms, or locations that meet other objectives such as finding networks that simultaneously minimize network cost, maximize probability of detecting a contaminant leak and minimize the extent of the contaminant distribution at first detection (Meyer et al., 1994; Storck et al., 1997).

More recent works in spatial sample design have begun to consider the sensitivity of a model output to the estimates of one or more heterogeneous state variables and/or the influence of the model acting on the spatially heterogeneous material properties. Spatial variability in material properties, such as transmissivity, leads to variations in the influence of any location within a model domain on the model results. For simple models of variability with few parameters governing the distribution of material properties, analytical techniques, such as Taylor series expansion, can be used to determine the sensitivity of the model output to the material property parameters. Work in this area has examined the sensitivity of mechanics models to the spatially discrete distribution of soil properties for geotechnical applications (Graettinger and Dowding, 2001). This approach has recently been extended to properties that vary continuously in space through the incorporation of kriging variance in the sensitivity calculations (Supriyaslip et al., 2003).

However, depending on the scale of the problem, the variation in many material properties may not be adequately described by simple assignment of homogeneous properties within predefined zones (Hill et al., 2001) and are better characterized as spatial random variables (SRV's). For these types of material properties, Monte Carlo sampling of the spatial random function can be employed. Here we propose a new approach for the calculation of spatial sensitivity coefficients based on the results of an ensemble of stochastic models. In contrast to previous work involving spatially varying sensitivity that has employed derivatives to determine sensitivities, the sensitivity values calculated herein rely on sampling-based sensitivity values (Helton and Davis, 2000). This work compares input parameter values to model outputs using rank regression as a sampling-based measure of sensitivity.

The goal of this portion of the report is to propose and demonstrate a new approach to monitoring network design that will specifically address the PA monitoring network design goal of providing head data for defensible calibration of PA models. Additionally, the approach developed here specifically incorporates PA information in the form of groundwater travel times from the repository area to the boundaries of the WIPP site. This approach makes use of the already existing ensemble of calibrated transmissivity fields (McKenna and Hart, 2003) such that no additional groundwater flow and/or transport modeling is necessary.

4.2 Derivative-Based Sensitivity Coefficients

The goal of this work is to develop a technique determining the sensitivity of a model output with respect to all uncertain inputs. While such an approach is generally applicable, the focus here is on spatially varying model inputs. Typically, sensitivity coefficients, S , are calculated as the derivative of a model output with respect to each input parameter:

$$S_{ij} = \frac{\partial O_i}{\partial P_j} \quad (14)$$

where S_{ij} is the sensitivity of the i^{th} model output, O_i , to the j^{th} model parameter, P_j . For models with a linear relationship between the input parameters and the output, values of S can be calculated directly. For models with non-linear relationships between the parameters and the outputs, a Taylor series expansion of the derivative is used to linearize the relationship and sensitivities (see Graettinger and Dowding, 2001). The Taylor series expansion approach is limited to a relatively small number of model parameters and may entail some specific assumptions (e.g., Gaussian distributions) on the uncertainty inherent in the model.

4.3 Sampling-Based Sensitivity Coefficients

Another approach to sensitivity calculation that is used heavily in probabilistic modeling is sampling-based sensitivity (Helton and Davis, 2000) where regression models are used to define relationships between model inputs and outputs. The spatially heterogeneous distribution of material properties is modeled as the realization of an SRV. While the values of the actual realization are only known at the sample locations, multiple conditional realizations of the SRV can be drawn from a specified spatial random function (SRF). A two-point spatial covariance model is used to define a spatially correlated, conditional, N -variate conditional cumulative distribution function (ccdf) of the N SRV's, Z_i . The multivariate cdfs, $F_{(N)}$, are defined as:

$$F_{(N)} = (z_1, \dots, z_N | (n)) = \text{Prob}\{Z_i \leq z_i, i=1, \dots, N | (n)\} \quad (15)$$

where z_i are the values sampled from SRV and $|n$ indicates the set of n data used to condition the N SRV's. The N variables represent the same attribute (e.g., transmissivity) sampled at the N nodes of a dense grid used to discretize the model domain.

Stochastic simulation algorithms are used to sample these cdfs where one set of samples results in a single spatially correlated property field (realization). Repeated application of these algorithms creates an ensemble of equally probable random fields that reproduces the first and second (bivariate) moments of a specified distribution under an assumption of second-order stationarity. Details of the stochastic spatial simulation algorithms can be found in the works of Goovaerts (1997) and Deutsch and Journel (1998). This ensemble of random fields is used as input to a physical process model (e.g., groundwater flow). For each application of the physical process model, a prediction of some performance measure is produced. The performance measure is the result of the integrated response of that physical process across the joint distribution of the sampled cdfs. Across the full ensemble of material fields, the physical process model acts as a transfer function to transfer the uncertainty in the spatial distribution of material properties to uncertainty in the resulting physical process.

The empirical distribution of simulated values at any location, \mathbf{x} , within the model domain across multiple realizations amounts to repeated independent samples of the local cdf. The actual distribution of $F(N, \mathbf{x})$ changes from one realization to the next, but across all L realizations a local cdf, $F_{(N, \mathbf{x}, l)}$ is defined. Each independent sample of $F_{(N, \mathbf{x}, l)}$ defines the property value of a single model cell in a single realization and therefore is associated with a single model output. All model cells in a given random field, l , are associated with the same model output O_l . Across the ensemble of all realizations, sensitivity of the model output to the property values at each location within the domain can be computed with sampling-based sensitivity techniques (Helton and Davis, 2000). Here we examine the ability of the Spearman rank correlation coefficient (see Conover, 1980) calculated for each location in the model domain, $r(\mathbf{x})_s$, to identify changes in O_l with respect to changes in the values drawn from $F_{(N, \mathbf{x}, l)}$. The Spearman rank correlation coefficient is:

$$r(\mathbf{x})_{Sp} = \frac{\sum_{i=1}^n (R_i - \bar{R})(S(\mathbf{x})_i - \bar{S}(\mathbf{x}))}{\sqrt{\sum_{i=1}^n (R_i - \bar{R})^2} \sqrt{\sum_{i=1}^n (S(\mathbf{x})_i - \bar{S}(\mathbf{x}))^2}} \quad (16)$$

where R and S are the internal ranks of O_l and the values contained in $F_{(N, \mathbf{x}, l)}$ respectively, and define the sensitivity of the integrated model output to each of the locally sampled property values. The value of $r(\mathbf{x})_s$ defines the proportion of the variability in O_l explained by $F_{(N, \mathbf{x}, l)}$ and can be displayed as a map across the model domain for all locations.

4.4 Application to Culebra Calculations

Determination of $r(\mathbf{x})_s$ across an ensemble of stochastic transmissivity fields is applied to the results of groundwater flow and advective transport models that use heterogeneous, stochastically-generated transmissivity (T) fields as input. Calculations of spatial sensitivity coefficients developed here are provided to determine the locations to which the groundwater flow model calibration is most sensitive to the simulated value of T and to simulated head values. These sampling-based sensitivity coefficients, calculated as $r(\mathbf{x})_s$, are compared to sensitivity coefficients calculated as partial derivatives of the model calibration (Equation 14) to the T value through a Taylor series approach at 99 selected locations. In addition to mapping the sensitivity of the model output to the spatially variable T, the spatial sensitivity of the model to the single state variable, pressure, is also determined.

Results of the previously completed transmissivity field calibration (McKenna and Hart, 2003) are used to compare analytically calculated sensitivity coefficients with the sampling-based sensitivity coefficients. For this comparison, the sensitivity of the overall calibration is calculated with respect to the estimated transmissivity values at each pilot point. The 100 transmissivity fields were created through a stochastic inverse modeling procedure where 99 pilot points distributed throughout the domain were considered to be the design variables in the inversion process (McKenna and Hart, 2003). The selection of the 100 fields used in this study was done by Beauheim (2003). For each pilot point, the inverse parameter estimation procedure calculates the sensitivity of the overall objective function to the estimated values of each pilot point. In the Culebra stochastic inverse modeling, the overall objective function was composed of both the mismatch between the modeled and measured heads, including both steady-state heads and drawdowns observed during a number of transient pumping tests, as well as the regularization function that forced the pilot point values to be as similar to each other as possible. The sensitivities of the value of the objective function with respect to the estimated values of the pilot points can be compared to the sampling-based sensitivity coefficients at the same locations.

The sensitivity coefficients for each pilot point are calculated as the relative composite sensitivity (Doherty, 2000):

$$S_{ii}^{rel} = \frac{(J'QJ)_{ii}^{1/2}}{m} \cdot |P_j| \quad (17)$$

where \mathbf{J} is the Jacobian where each column is composed of entries of numerically calculated sensitivities of each parameter to each of the m observations. \mathbf{Q} is a diagonal cofactor matrix containing the weights assigned to each observation and P_j is the final estimated value of the j^{th} parameter. For the Culebra transmissivity field calibrations, the quantity estimated at every location was the residual between a base transmissivity value estimated from a geologic conceptual model and a response surface that was conditioned to the actual transmissivity measurements at the well test locations (McKenna and Hart, 2003). Both the base transmissivity field and the response surface were defined in units of $\log_{10} (\text{m}^2/\text{s})$ and therefore the estimated residual values also have units of $\log_{10} (\text{m}^2/\text{s})$.

The sampling-based sensitivity coefficients are determined using all 100 transmissivity fields, whereas the relative composite sensitivity coefficients are calculated separately on each calibrated transmissivity field. To facilitate comparison of the two types of sensitivity coefficients, the average value of S_{ii}^{rel} is calculated across all 100 transmissivity fields. Additionally, the calculation of S_{ii}^{rel} uses the absolute value of the parameter as estimated in log10 space, so these values are compared to the absolute values of the sampling-based sensitivity coefficients. The comparison between the two types of sensitivity coefficients is shown in Figure 21.

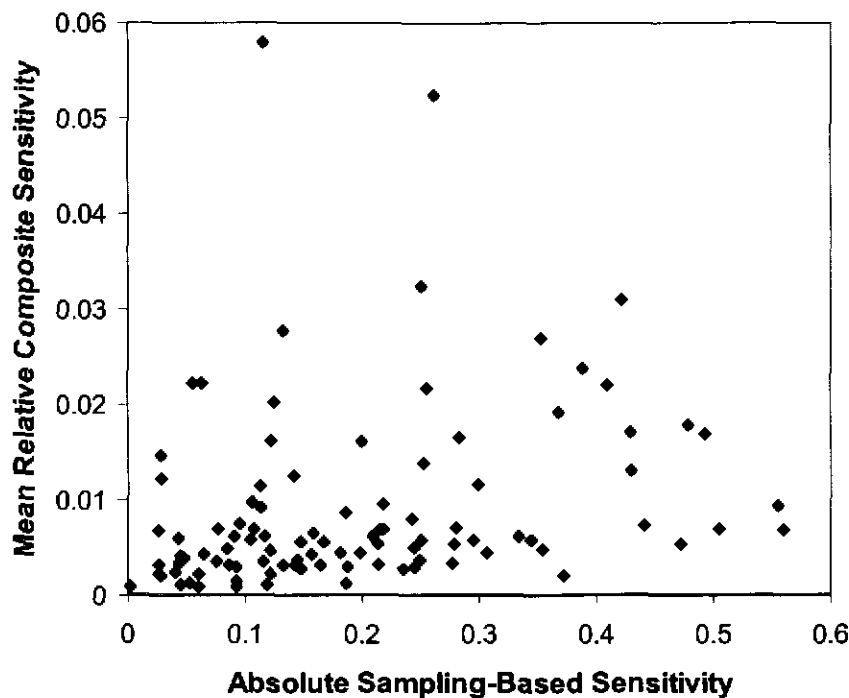


Figure 21. Comparison of sampling-based sensitivity coefficients to the median of the analytically calculated sensitivity coefficients. Both sets of coefficients define the sensitivity to the overall model calibration with respect to the estimated head at 99 different locations.

The comparison of the two types of sensitivity calculations shows that while there is a weak positive correlation there is not strong one-to-one relationship between the two types of sensitivity coefficients. This is expected as the composite sensitivities are calculated analytically on each realization and then the mean over all realizations is taken, whereas each sampling-based sensitivity is calculated using results across all realizations as input. However, it is not the direct relationship between the two quantities that is most important. Analysis of either quantity should be able to identify areas of relatively higher and lower sensitivity of the calibration to the transmissivity field. Comparison of the correlation between the ranks of the two different quantities shows a correlation coefficient of 0.67, indicating moderate correlation between the ranks of the two different sets of sensitivities.

Advantages of the sampling-based sensitivity coefficients over the composite sensitivity coefficients are: 1) that they are calculated at all locations in the model domain; and 2) they can be calculated after the groundwater model calculations with respect to any model output. These advantages are demonstrated in Figures 22 and 23. Figure 22 shows the sensitivity of the model calibration to the simulated heads at all locations in the domain. This relationship was not calculated using the composite sensitivities but done as a post-processing step on the model results. Figure 23 shows the sensitivity of the overall model calibration to the transmissivity at all locations. This map shows the same relationship calculated with the composite sensitivities at the 99 pilot points, but done at all locations using the sampling-based sensitivity coefficient approach. The circular lines seen in Figure 23 are due to the circular updating pattern extending out from each pilot point. These lines are most apparent in the high T and low T regions on the west and east of the site, respectively, where the pilot point density is lower.

For the sensitivity of the model calibration to both head and transmissivity, the results show higher sensitivity to the head solution than to the transmissivity values. The map of sensitivity of the model calibration with respect to head shows large, spatially continuous regions of positive and negative sensitivity (Figure 22). These results are due to the diffusive nature of the pressure solution. The sensitivity of the model calibration to the transmissivity values (Figure 23) shows more localized regions of high and low sensitivity. These results are due to the more complex and local relationship between transmissivity and the simulated head values. Comparison of Figures 22 and 23 shows that locations of high sensitivity with respect to transmissivity are not necessarily collocated with locations of high sensitivity with respect to head.

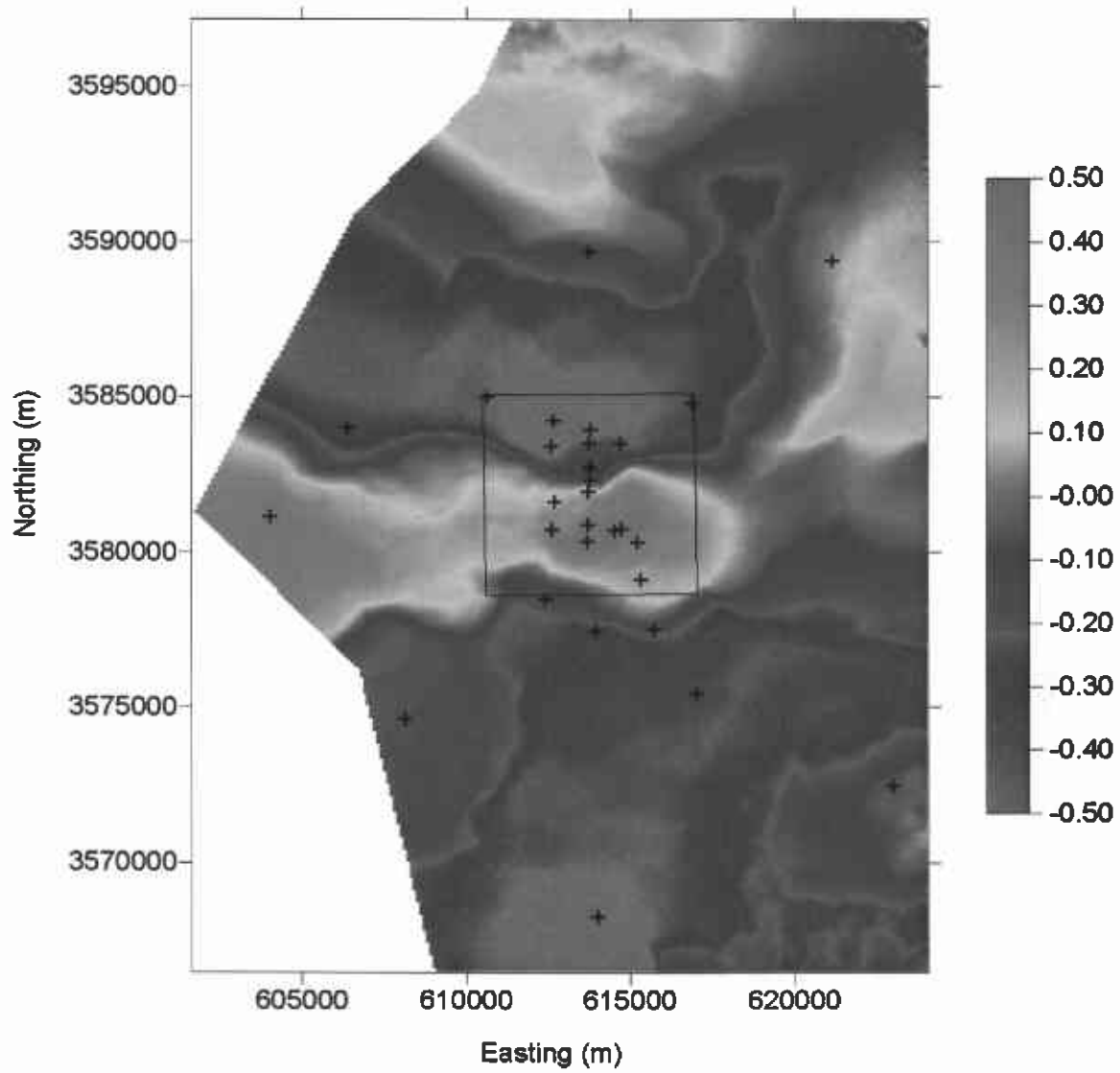


Figure 22. Sampling-based sensitivity of the overall steady-state and transient calibration to the simulated head values.

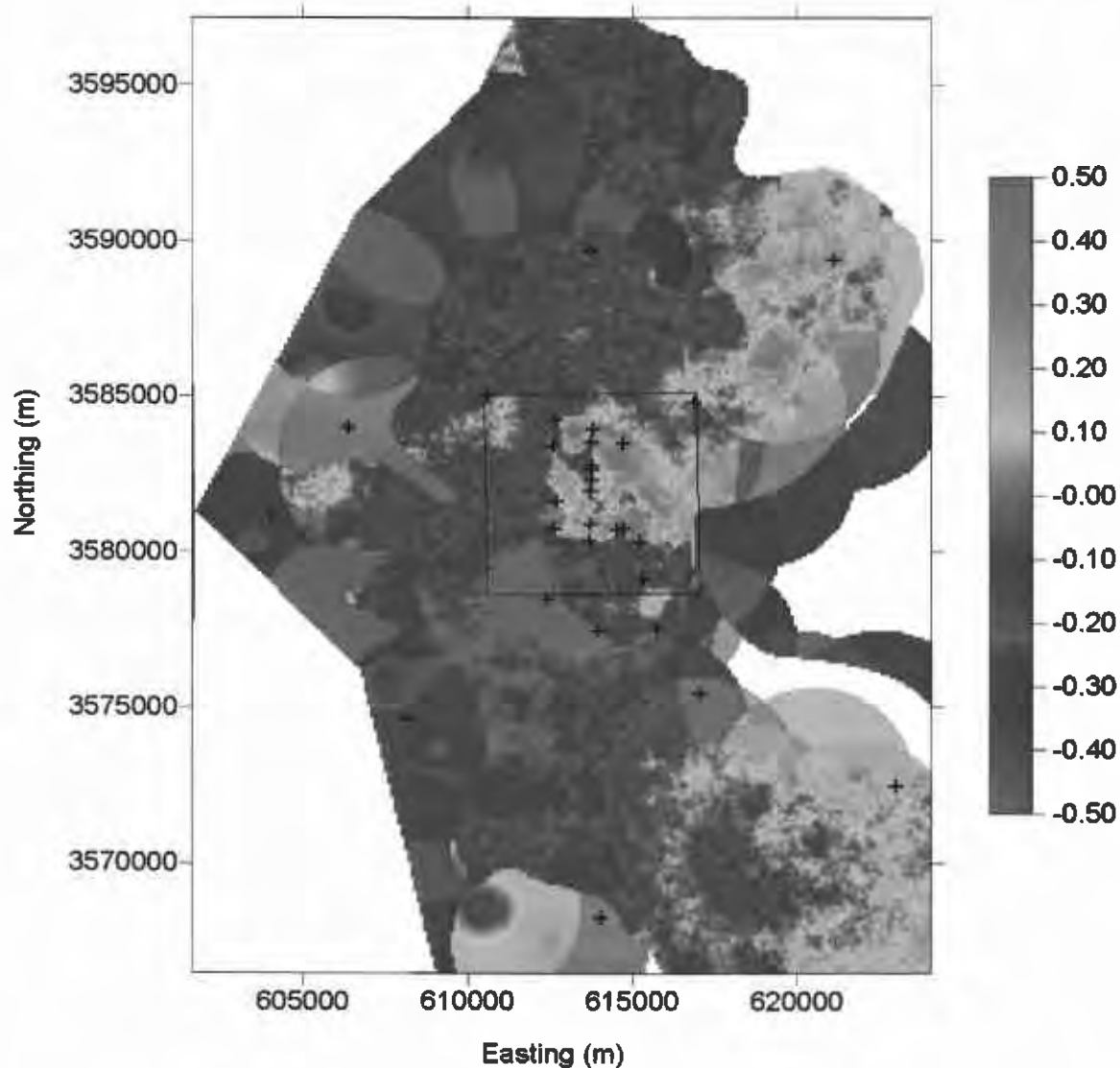


Figure 23. Sampling-based sensitivity of the overall steady-state and transient calibration to the calibrated transmissivity values.

4.5 Results

The calibration of the 100 transmissivity fields to steady-state and transient heads did not incorporate the groundwater travel time as an estimation variable. The groundwater travel time was a separate calculation done after the transmissivity fields were calibrated; therefore, the sensitivity of the groundwater travel time to either heads or transmissivity cannot be calculated using the composite sensitivity calculation (Equation 17).

The sampling-based sensitivity approach was applied to the results of the 100 calibrated transmissivity fields and used to determine the sensitivity of the groundwater travel time to the

WIPP boundary with respect to both the simulated heads and the calibrated transmissivity values. The results of these calculations are shown in Figures 24 and 25, respectively. The wells shown in Figures 24 and 25 are the set of 30 monitoring wells used in the previous monitoring network design calculations; it is important to note that these are not necessarily the same wells that were used to calibrate the transmissivity fields. A map showing each of the 100 paths along which travel time was calculated is shown in Figure 26 as a reference for the discussion below.

The results show that the magnitudes of the correlation coefficients are not very large, signifying weak to moderate correlation, both positive and negative, between the travel time to the WIPP boundary and the heads and transmissivities used to calculate those travel times. However, the results clearly show regions of relatively higher and lower travel time sensitivity to the two input parameters. The map showing sensitivity of travel time with respect to head (Figure 24) shows a much more smoothly varying image of sensitivity than does the map of travel time sensitivity with respect to transmissivity (Figure 25). These results are consistent with the diffusive relationship between head potential field and travel time and the much more focused and short spatial scale advective relationship between transmissivity and travel time.

There are two main regions of the site where the travel time is most sensitive to the value of estimated head. These are the large positive region to the south of the western portion of the site and the smaller negatively correlated region located in the WIPP site and extending out to the west of the WIPP site. Intuitively, the positive correlation south of the site is the result of increased head south of the site decreasing the relative gradient and therefore increasing the amount of time it takes for water to flow off-site. It is interesting to note that this high correlation region does not extend across the entire domain to the east. This appears to be due to only a few travel paths exiting the southern WIPP boundary on the east side (Figure 26).

The region of negative correlation within and to the west of the site (Figure 24) defines an area where increases in head result in shorter travel times and vice versa. This region is interpreted as locations that both change the timing and the direction of the flow paths out of the WIPP site, although there is no clear visual relationship between this region and the locations of the paths leaving the WIPP site.

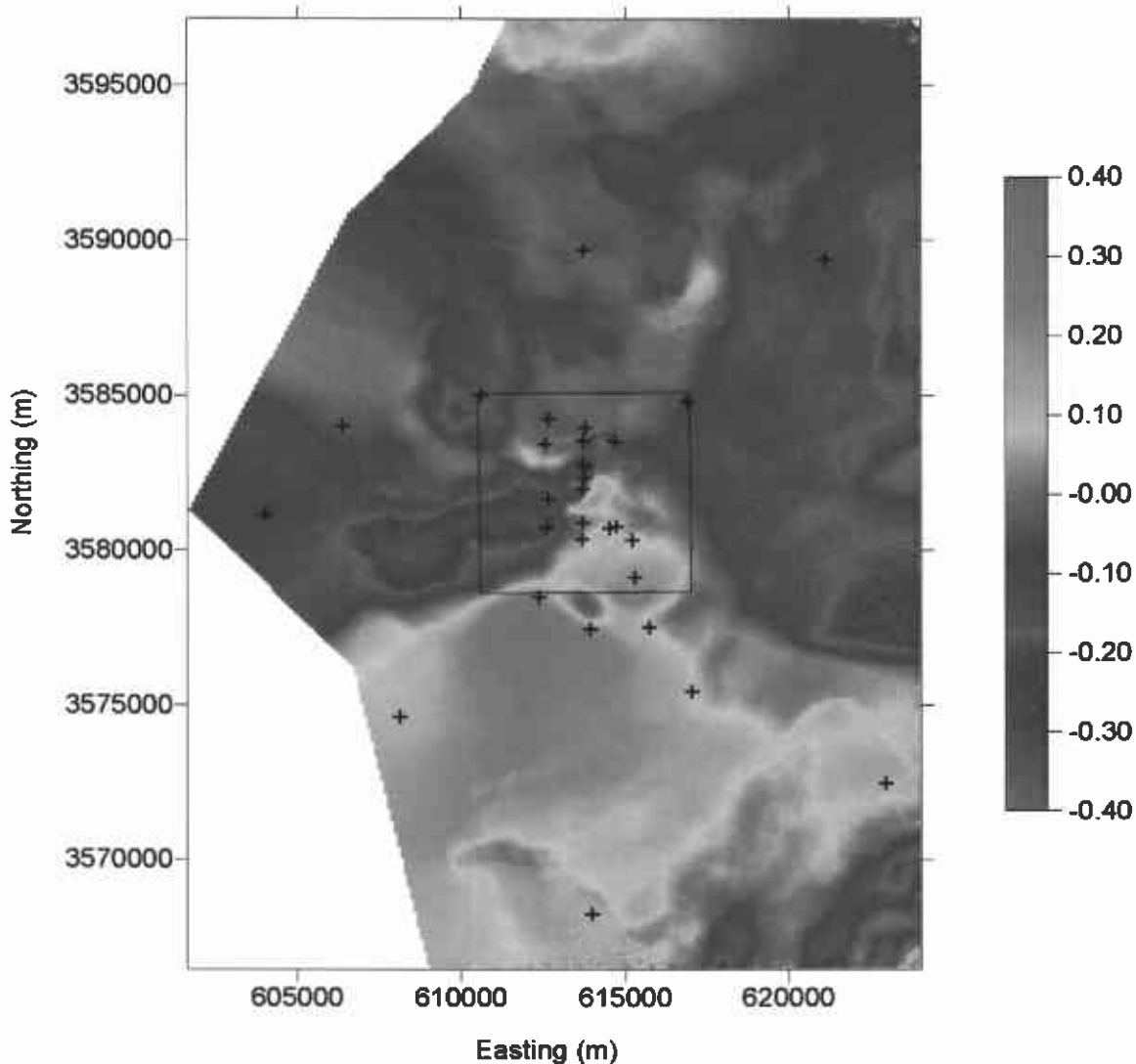


Figure 24. Sampling-based sensitivity of travel time to the WIPP boundary with respect to simulated heads.

For the sensitivity with respect to transmissivity (Figure 25), the location with the strongest correlation (negative) is just south of the center of the southern WIPP site boundary. Low transmissivity values in this location result in long travel times and vice versa. This area of negative correlation is coincident with a high density of flowpaths (Figure 26). There are several small regions of relatively high positive correlation throughout the domain. Two of these are near the extreme boundaries of the domain. At the north end, a small area serves to connect the high-T zone down the west side of the domain to the northern fixed-head boundary condition. The higher the T in this zone, the more flux goes down the western edge and avoids the WIPP site resulting in longer travel times. At the southern end of the domain, there is a relatively large region of high correlation that has some positive relationship with the travel time to the WIPP site boundary. The cause of this increased correlation has not been identified. The relatively

high correlation regions to the west of the WIPP site provide a connection between the high-T zone and the WIPP site. When T is high in these regions, travel time is longer and the interpretation is that flow path directions are altered to provide longer travel times with this influx of water into the WIPP site region. The uncolored regions in the east and northeast regions of Figure 25 identify locations where transmissivity never changed across the 100 realizations. These areas are in the low transmissivity zone on the east side of the domain and are far from any pilot point. No changes in the transmissivity make it impossible to calculate the rank regression coefficient for these areas.

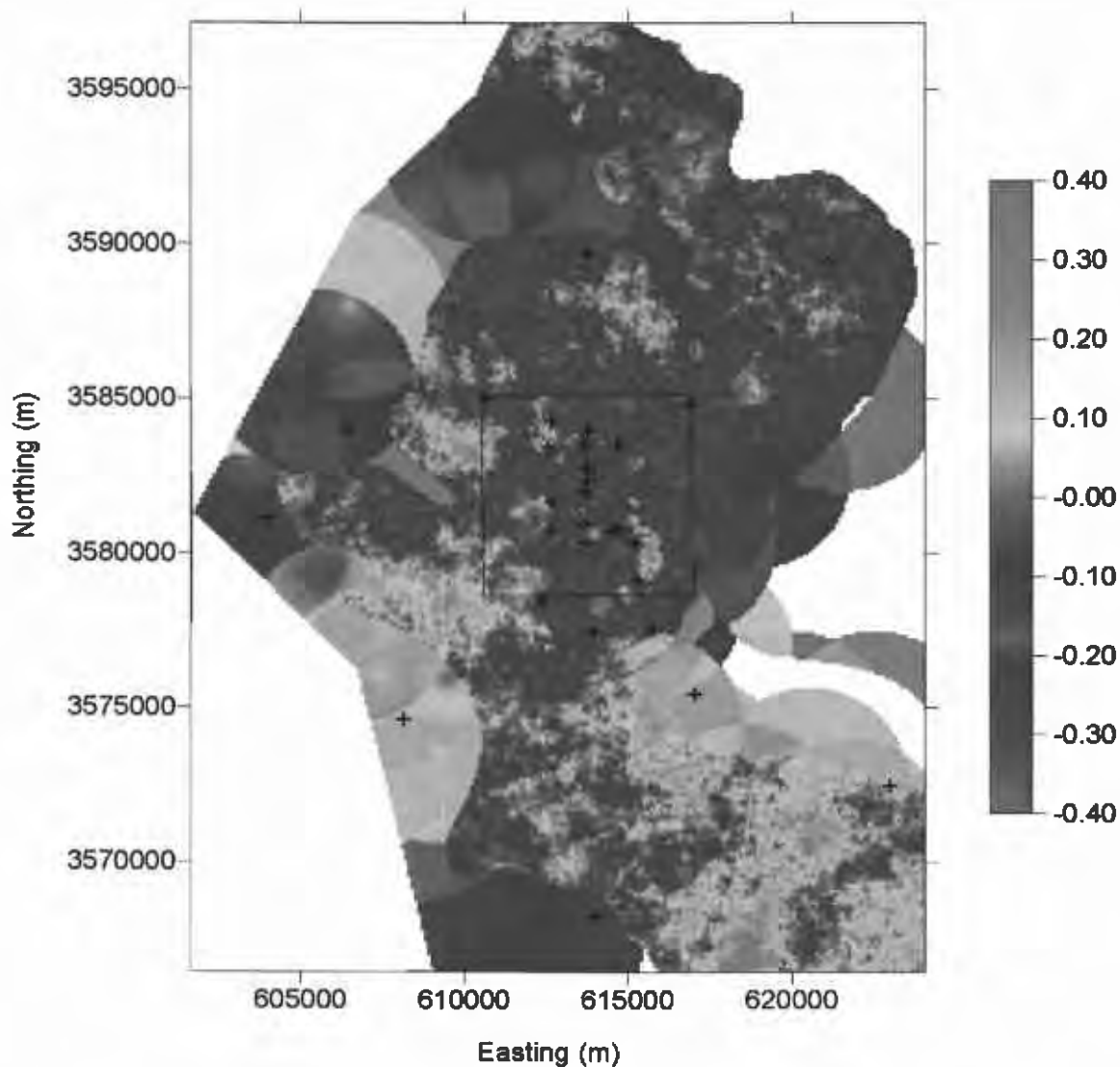


Figure 25. Sampling-based sensitivity of the travel time to the WIPP boundary with respect to calibrated transmissivity values.

It is noted here that identification of areas to increase knowledge of T pertains more to site characterization activities and is not directly a concern in long-term monitoring. However, T enters the PA calculations as the parameter that is optimized during the calibration of the T fields that are used in subsequent radionuclide transport calculations for PA. Areas of the domain

where travel time has high sensitivity to T (Figure 25) identify locations where a single-well or multi-well transmissivity test would reduce uncertainty in T that affects travel times. These types of measurements can be seen as one-time efforts and these locations do not necessarily identify optimal locations for long-term monitoring of heads and gradients.

The spatial sensitivity of groundwater travel time through the heterogeneous transmissivity fields is calculated for a single groundwater travel time performance measure. Relative to the results for the model calibration, the sensitivity of the groundwater travel time to T is elevated in only very localized regions. The areas of high sensitivity of the travel time to pressure are larger and more diffuse. The correlation at any one location in the model domain is not especially strong. Absolute values of the Spearman correlation coefficient from 0.20 to 0.30 are typical, with maximum values of 0.60 to 0.70 depending on the sensitivity calculation.

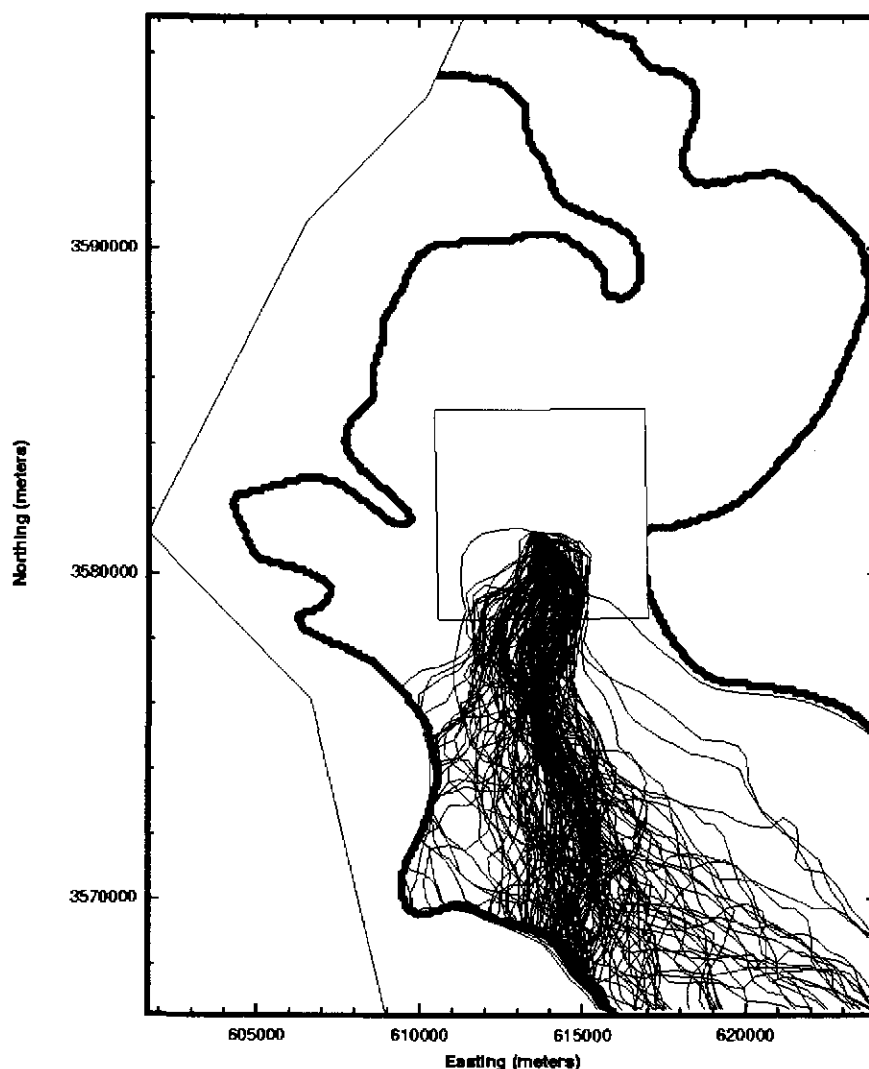


Figure 26. Locations of the 100 flowpaths along which travel time to the boundary of the WIPP site is calculated.

4.6 Summary

Calculation of sensitivity coefficients across a spatial domain has only recently been applied and these applications have focused on the sensitivity of model results to a small number of input parameters. Here, a new sampling-based sensitivity analysis procedure that considers the sensitivity of an integrated model output to each of N input variables has been developed. These sampling-based sensitivity coefficients are consistent with, but different from, the average sensitivities calculated as numerical derivatives at 99 pilot points. Each set of sensitivities calculated at the pilot points is done for a single realization of the transmissivity field. The advantage of this approach to calculating sensitivity is that it is computationally efficient; however, the disadvantage is that it only provides sensitivity of a chosen output to the input variable for a given configuration of the transmissivity field. The sampling-based sensitivity coefficients require an ensemble of calibrated transmissivity fields, which is computationally burdensome, but they provide an integrated measure of sensitivity to all of the calibrated transmissivity fields at once. This approach captures the non-uniqueness of the transmissivity calibration by using all 100 calibrated fields and also provides a measure of output sensitivity to the input variables at all locations within the domain.

Application of the sampling-based sensitivity approach to the Culebra shows distinct regions of higher and lower sensitivity to travel time with respect to both calibrated heads and transmissivity. For travel time sensitivity with respect to heads, the regions of high and low sensitivity are broad and fall mainly within and directly to the south of the WIPP site. Results of travel time sensitivity with respect to transmissivity show regions of high and low sensitivity that are considerably more localized. The region with the greatest absolute value of sensitivity is approximately 1 km square directly below the central portion of the southern WIPP-site boundary. These regions of high or low sensitivity can be identified and targeted for additional head monitoring wells and measurements of transmissivity. Results of the spatial sensitivity calculations are combined with results of other approaches to monitoring well optimization in the following section

The spatial sensitivity calculations are the only one of the three techniques used to identify locations for additional monitoring wells that directly link the monitoring network to a PA calculation. This direct link identifies regions of the Culebra where the travel times to the WIPP boundary are most sensitive to calibrated head and transmissivity values. However, it is necessary to keep in mind that these PA calculations are predictions and the regions of increased sensitivity determined here are only as good as these PA predictions. If the conceptual model of transmissivity, including the definition of the high and low transmissivity regions, changes, the results of these sensitivity calculations will change. Furthermore, the sensitivity calculations use the groundwater flow models calibrated with the current set of boundary conditions and responses to transient hydraulic tests. When new data are acquired that change these boundary conditions or that provide different transient calibration targets, these may also change the calculated regions of elevated sensitivity.

4.7 Calculation Details

The calculation of the Spearman rank correlation coefficients as spatial sensitivity coefficients was done using the program **vsap** on the Albuquerque linux cluster *lylin102*. The **vsap** source and executable are in the */h/wipp/sensitivity/steady-state/QAd/source* directory. The actual

calculations using **vlsap** are in the */h/wipp/sensitivity/steady-state/QAd/* directory. The **vlsap** program is designed to be run from a single set of instructions entered on the command line. Multiple runs of **vlsap** to calculate different sensitivity coefficients are completed using the shell *GetSens.sh*. A listing of this shell is provided in Appendix 10. Prior to running the *GetSens.sh* shell, it is necessary to identify the 100 calibrated transmissivity and head fields to be used in the calculations. These fields are accessed and stored in the correct locations for running **vlsap** by using the shell *GetTop100.sh*. A listing of this shell is included in Appendix 10. These 100 fields are a subset of the fields calibrated by McKenna and Hart (2003). The **vlsap** program is tested on 100 realizations of a 1x100 cell test problem that is also run in Excel. The testing is summarized in Appendix 10.

5.0 Combining Monitoring Approaches

Three different approaches to identifying optimal locations for additional monitoring wells have been demonstrated and, in some cases, developed in this work. In the case of the geostatistical estimation variance reduction approach, areas of high estimation variance were identified as being locations for additional wells. However, there are many locations with high estimation variance and the results of this approach do not uniquely identify optimal locations for additional wells. To some extent, combining all three of the approaches into a single map can reduce this non-uniqueness. Here, the three approaches are combined to provide a combined score, S_c , that identifies the best locations for new wells. The higher the value of the score, the better the location for a new well.

The combined score is the weighted sum of the three different measures calculated in the three monitoring approaches.

$$S_c = \omega_1 \sigma_{OK}^2(\mathbf{x}) + \omega_2 N_{3pt}(\mathbf{x}) + \omega_3 |r(\mathbf{x})_s| \quad (18)$$

The three components of S_c are the ordinary kriging variance, σ_{OK}^2 , calculated from the existing network, the total number of acceptable three-point estimators when a new monitoring well is added to the network at location x , N_{3pt} , and the absolute value of the rank correlation coefficient between travel time to the WIPP boundary and either the estimated transmissivity or head, r_s . The absolute value of the rank correlation coefficient is used as both positive and negative values are of equal importance for locating new monitoring wells. For every location, \mathbf{x} , in the model domain, all three component values of S_c are determined. The weights, ω_i , can be adjusted to account for more or less emphasis on any of the three components. For the results presented here, each component of the combined score is equally weighted: $\omega_1 = \omega_2 = \omega_3 = 1.0$, and the weights are dropped from further development of the combined score equations.

The units of the different results to identifying monitoring locations are not consistent, being in m^2 , number of triangles, and unitless. Therefore, it is necessary to rescale the results into dimensionless values. This rescaling is accomplished as:

$$S_c = \frac{\sigma_{OK}^2(\mathbf{x}) - MIN(\sigma_{OK}^2(\mathbf{x}))}{MAX(\sigma_{OK}^2(\mathbf{x})) - MIN(\sigma_{OK}^2(\mathbf{x}))} + \frac{N_{3pt}(\mathbf{x}) - MIN(N_{3pt}(\mathbf{x}))}{MAX(N_{3pt}(\mathbf{x})) - MIN(N_{3pt}(\mathbf{x}))} + \frac{|r(\mathbf{x})_s| - MIN(|r(\mathbf{x})_s|)}{MAX(|r(\mathbf{x})_s|) - MIN(|r(\mathbf{x})_s|)} \quad (19)$$

where the MAX and MIN operators define the maximum and minimum values of the different components of the combined score across the entire calculation domain. This rescaling process constrains the values of each component to lie within [0,1].

Maps of the rescaled components of the combined score are shown in Figures 27, 28, 29 and 30. These maps can be compared with the maps of the raw, not rescaled, components in Figures 5,

14, 24 and 25, respectively. In each of the rescaled maps, the August 2003 monitoring network is shown along with eight additional wells that have been completed in the last several years. These well locations were determined using a number of factors independent of the monitoring network optimization approaches defined in this report and are shown here for comparison purposes. The names and locations of the eight new wells are given in Table 12.

Table 12. Names and location of new monitoring network wells.

Well Name	X coordinate (m)	Y coordinate (m)
C-2737	613597	3581401
IMC-461	606180	3582240
SNL-1	613782	3594302
SNL-2	609113	3586529
SNL-3	616103	3589047
SNL-5	611984	3587281
SNL-9	608705	3582238
SNL-12	613210	3572728

5.1 Results

The final maps of the combined score values are shown in Figures 30 and 31. The theoretical minimum and maximum combined score values for any location are 0.0 and 3.0 respectively. The calculated minimum and maximum combined score values when the sensitivities of travel time to head are one of the components (Figure 31) are 0.1 to 2.4, respectively; when the sensitivity of travel time to transmissivity is included as a component (Figure 33), the maximum and minimum values are 0.08 and 2.2.

The combined score map that includes sensitivity of travel time with respect to head (Figure 31) shows the highest combined scores to the west, south and east of the WIPP site. The lowest scores occur within the WIPP site boundaries. The character of the three component maps is evident in the final combined score map, which is controlled mainly by the rescaled estimation variance map (Figure 27) and the rescaled sensitivity of the travel time to the estimated heads map (Figure 29). The area of high combined scores to the east of the site is to the east of the low transmissivity boundary. The high values of the combined score in this area are caused by high values of all three components (Figures 27, 28, 29 and 30), but it is noted that only one of these three components is directly based on solution of the groundwater flow model (Figure 30). The high component scores in this region east of the site for the estimation variance and the three-point estimators are due mainly to the paucity of monitoring wells in this area.

The combined score map that includes the sensitivity of the travel time to the calibrated transmissivities (Figure 30) shows that the lowest combined scores occur in the center of the WIPP site and this area is not optimal for the location of additional monitoring wells. The locations with the highest combined scores are generally controlled by the estimation variance and number of acceptable three-point estimator maps. These high score locations are generally located at the northern and southern portions of the domain in areas distant from existing wells.

The two combined score maps, Figures 31 and 32, show similar results for the locations of the calculated regions of high and low scores. This result is not surprising given that two of the components in each map are identical: the estimation variance and number of three-point estimators (Figures 27 and 28). Therefore the differences in the combined score maps are due to differences in the travel time sensitivity maps (Figures 29 and 30). One strong difference in these maps is that the highest sensitivity of travel time with respect to transmissivity occurs just south of the southern WIPP site boundary (Figure 30), but this location has extremely low travel time sensitivity with respect to heads (Figure 29). Therefore, the combined score for this region is low or moderately high depending on whether the sensitivity is calculated with respect to head (Figure 29) or transmissivity (Figure 30). These results point up the fundamental difference in identifying locations needed for better understanding of T in order to calibrate PA models versus locations identified for long-term monitoring of heads and gradients. If the main goal of new monitoring wells is to identify transmissivity and to reduce uncertainty in the travel time calculations, then it may be prudent to locate a well in this location. If monitoring changes in the heads and the gradient over time is the main goal, then this location may not require a new well.

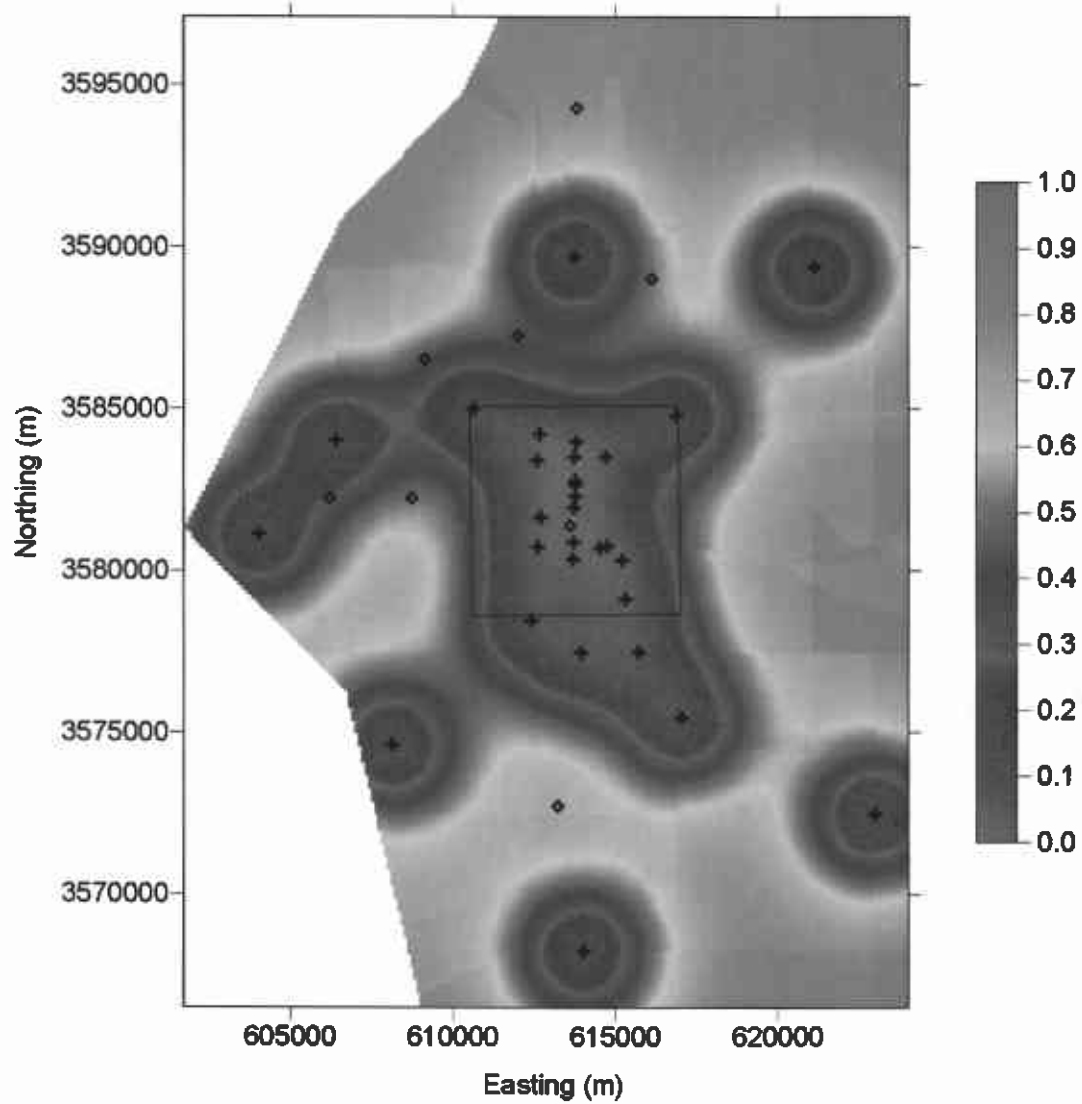


Figure 27. Rescaled [0,1] estimation variance map. The wells in the historic monitoring network are shown as plus signs; the new well locations are shown by diamonds.

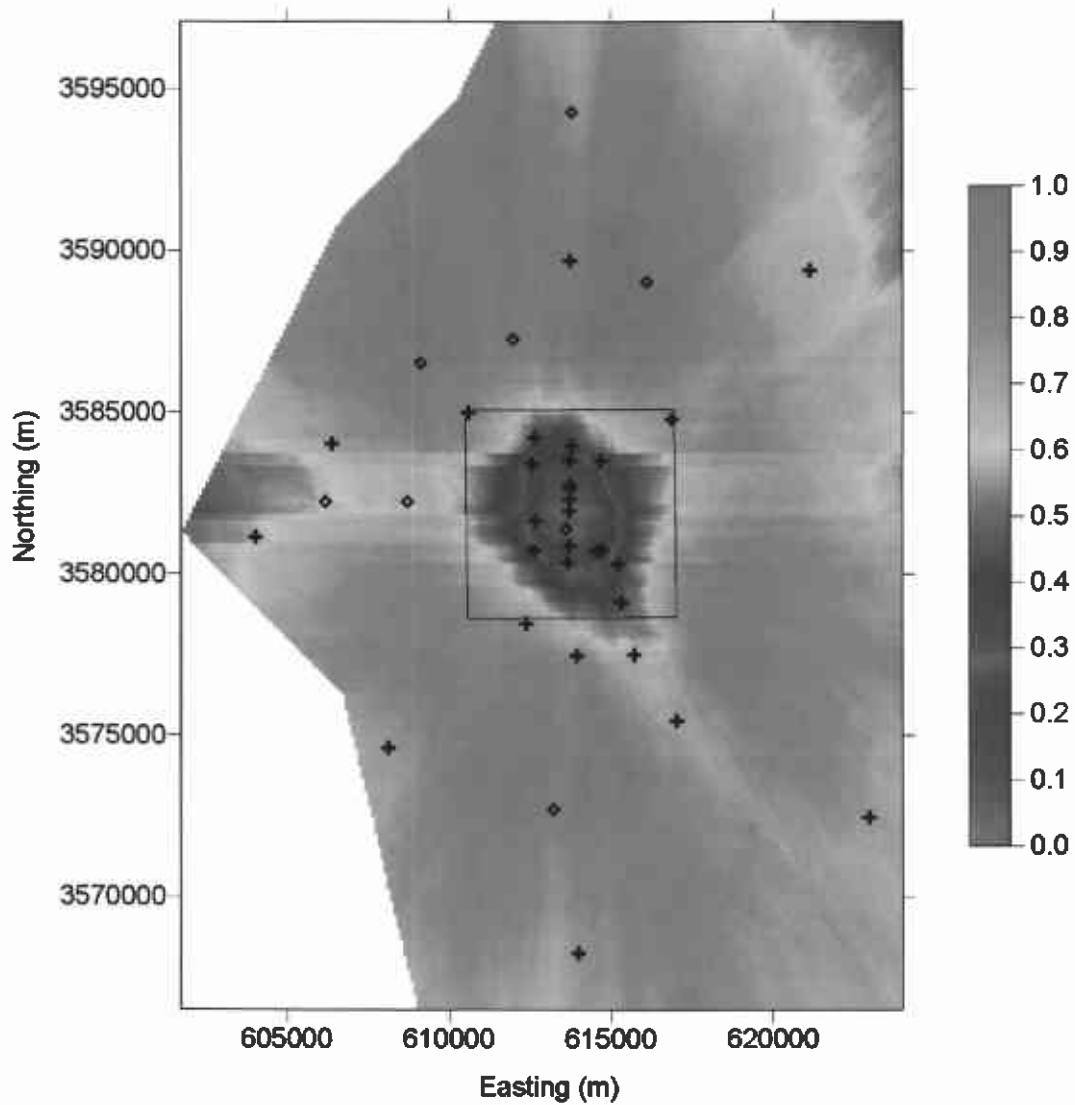


Figure 28. Rescaled [0,1] number of acceptable three-point estimators map. The wells in the historic monitoring network are shown as plus signs; the new well locations are shown by diamonds.

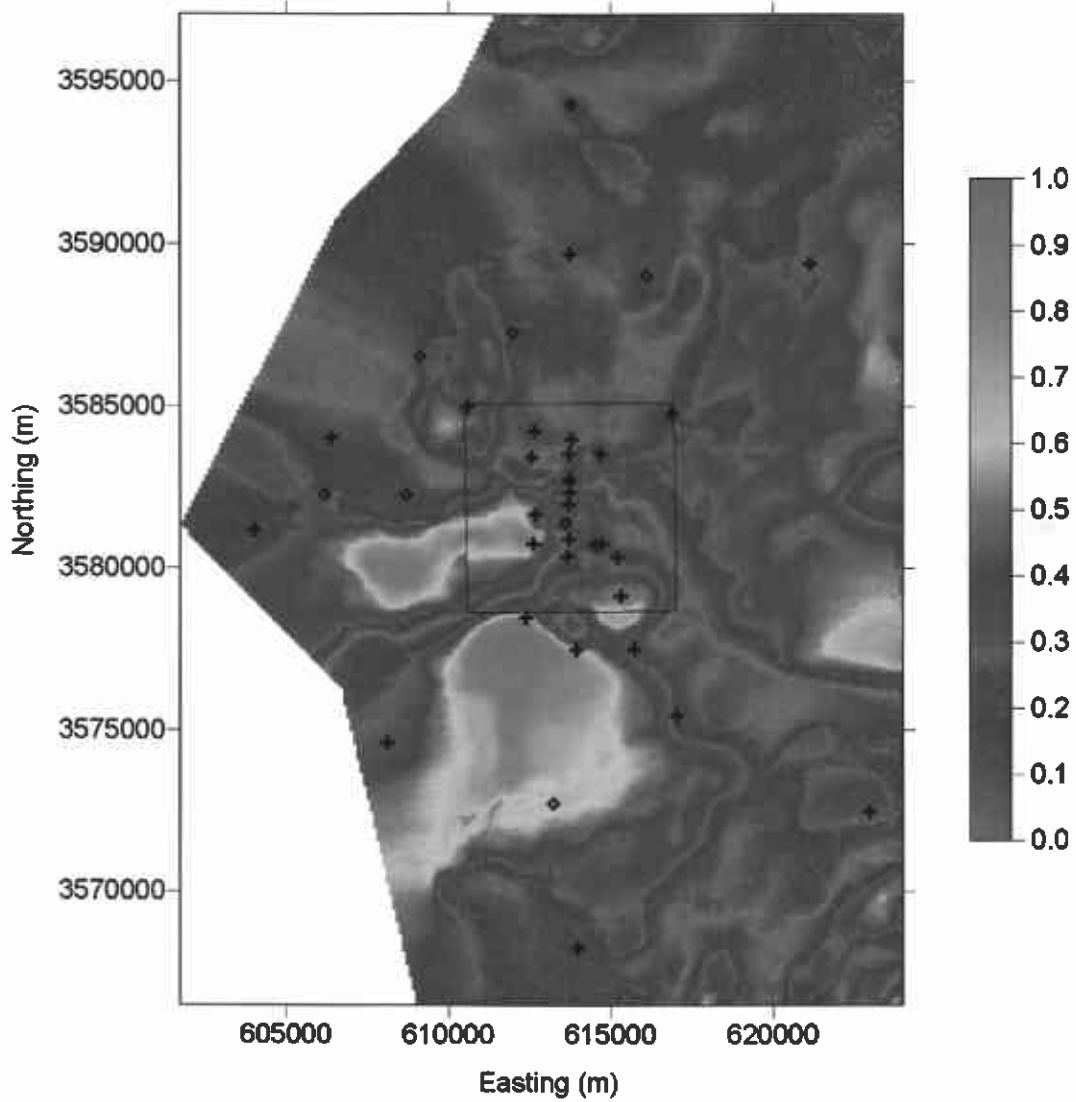


Figure 29. Rescaled [0,1] absolute value of the sensitivity of the travel time to the WIPP boundary with respect to the estimated head at every point. The wells in the historic monitoring network are shown as plus signs; the new well locations are shown by diamonds.

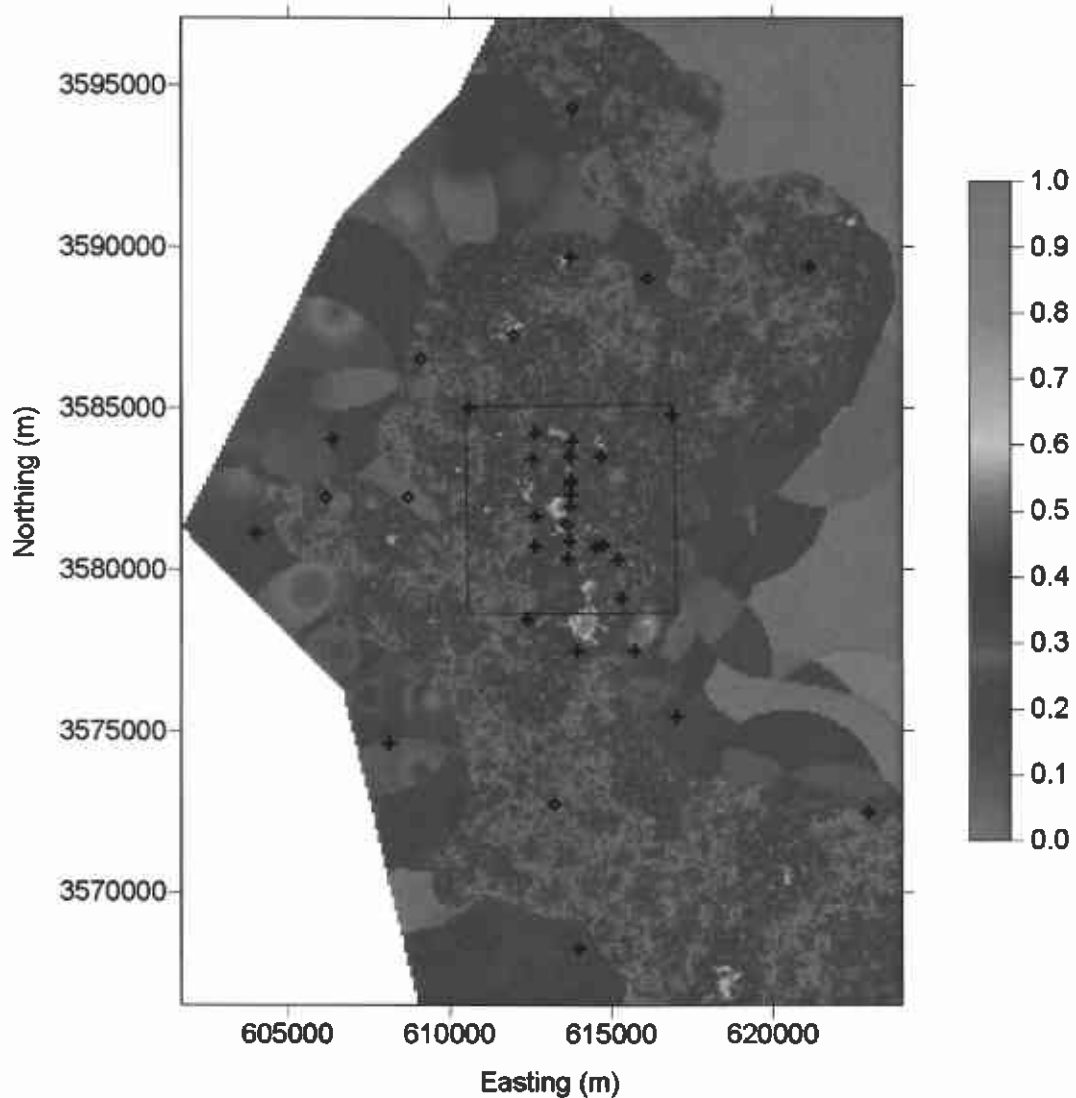


Figure 30. Rescaled [0,1] absolute value of the sensitivity of the travel time to the WIPP boundary with respect to the transmissivity at every point. The wells in the historic monitoring network are shown as plus signs; the new well locations are shown by diamonds.

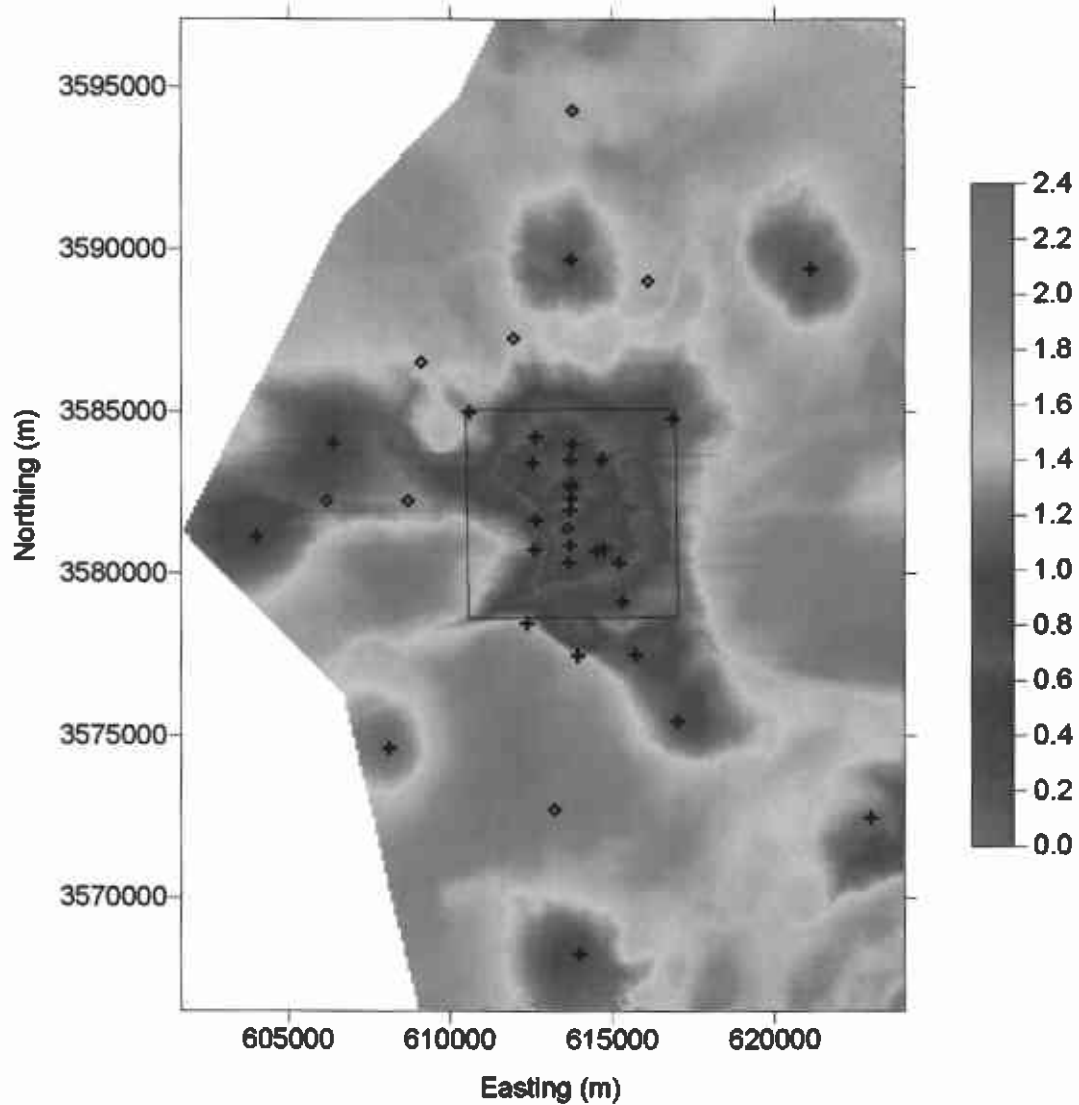


Figure 31. Combined score values map including estimation variance, number of three-point estimators and sensitivity of travel time to head. The wells in the historic monitoring network are shown as plus signs; the new well locations are shown by diamonds.

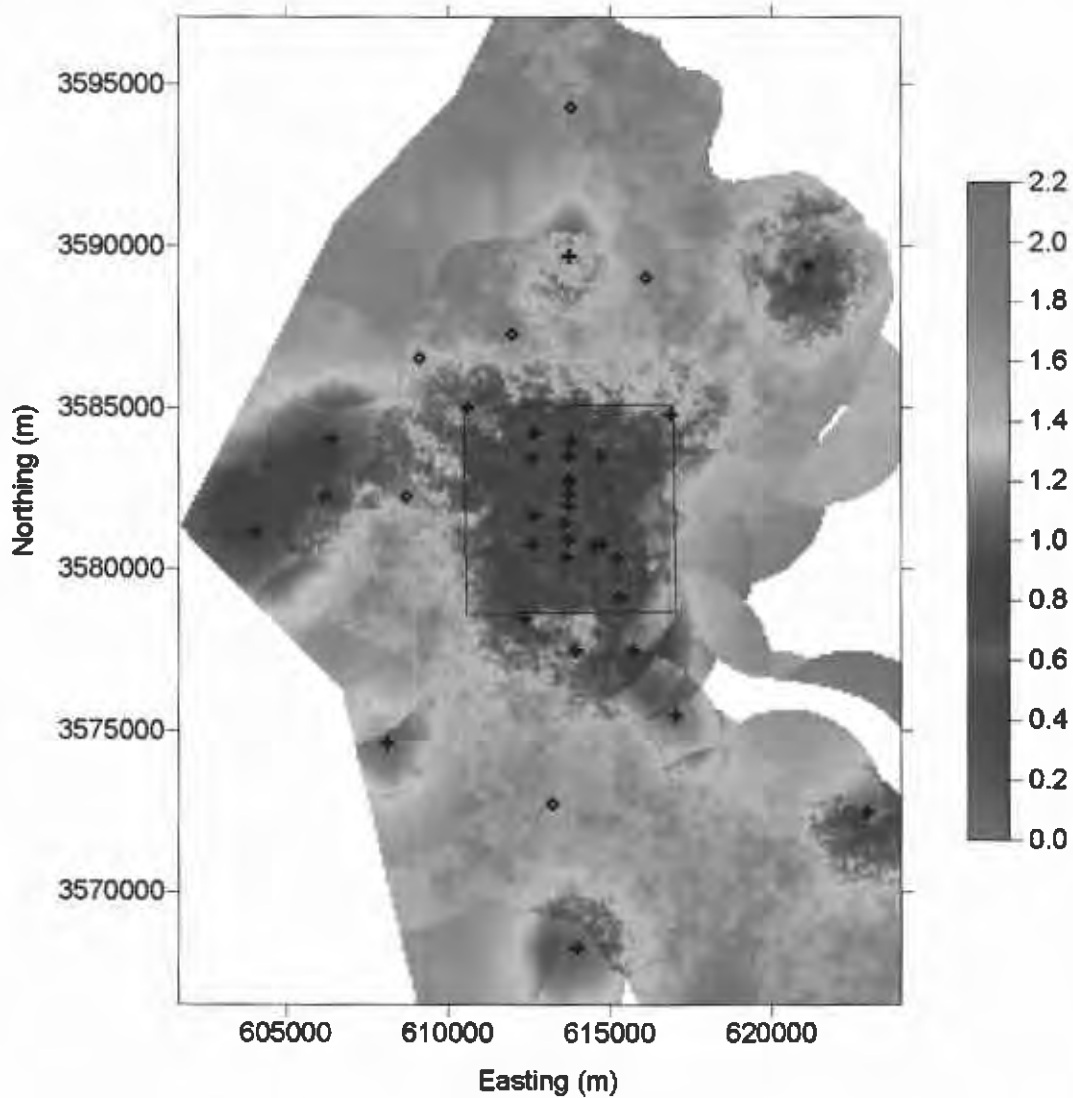


Figure 32. Combined score values map including estimation variance, number of three-point estimators and sensitivity of travel time to transmissivity. The wells in the historic monitoring network are shown as plus signs; the new well locations are shown by diamonds.

5.2 Summary

Three different approaches to monitoring network optimization were used to identify locations where additional wells could improve the network. These three approaches identify: 1) locations where additional wells will reduce the uncertainty in predicting head values at locations without wells; 2) locations where an additional well will allow for maximum improvement in the ability of the existing monitoring well network to identify changes in the magnitude and orientation of the hydraulic gradient by maximizing the additional number of acceptable local gradient estimators that can be created; and 3) locations where the performance assessment measure of advective travel time to the WIPP boundary is most sensitive to the value of head or transmissivity.

These three approaches to monitoring network design all attempt to optimize the network with respect to different objectives. Combining all three of these approaches is done by rescaling each of the raw maps of estimation variance, additional local gradient estimators and sensitivity to have a range (minimum to maximum) of 1.0 and to be unitless. The final combined score maps show, on a scale of 0.0 to 3.0, the best places to locate additional wells to meet all three objectives when each of the three objectives is given equal weight. The higher the combined score, the better the location for a new well. The final combined maps are similar with some minor, but important differences depending on whether or not sensitivity with respect to head or transmissivity is included in the combined score.

Eight new wells have recently been constructed (Table 12). Although constructed for a variety of reasons, the combined score values in the locations of these new wells are, fortuitously, all relatively high with the exception of C-2737 within the WIPP site and IMC-461 and SNL-9. C-2737 was sited to provide a monitoring location directly above the center of the WIPP disposal panels. IMC-461 was a “borehole of opportunity” with no DOE control over its location. SNL-9 was situated precisely where it was to verify the geologic model underlying the transmissivity fields used for this study.

5.3 Calculation Details

All calculations for the combined score maps are made in the *Monitoring_04\combine* subdirectory on the CD-ROM included as part of this analysis package. A single code, **combine**, was written to do the combined score calculations. This code was written and compiled under **Microsoft Visual Studio, Version 6.0** on a Pentium 4, 1.7-GHz processor PC running the MS Windows 2000 operating system. The compiled version of the combine code used here is located in the *Monitoring_04\combine\debug* subdirectory.

The **combine** program is run from the DOS command prompt and prompts the user to enter the names of three input files and writes a single output file. For the calculations done here, the input files are:

- 1) *kt3d.out*: the output file created by running the **kt3d** code in the *Monitoring_04\Geostat* subdirectory. This file has a four-line header and two columns of output. Only the estimation variance, in the second column, is used by the **combine** code.
- 2) *numbers.out*: the output file created by running the **locat** program in the *Monitoring_04\locat_triangle* subdirectory. This file has three columns: X, Y and total

number of acceptable three-point estimators when a new monitoring well is added at this X,Y location, and no header lines.

- 3) *sens.WTime_to_t.map* or *sens.WTime_to_h.map*: the output file created by the **vlsap** program run on the linux cluster. This file is a 307×224 matrix of numbers that are the Spearman rank correlation coefficients between travel time and either head or transmissivity depending on which input file is entered.

The **combine** code reads in the three files taking into account the different file formats and ordering and applies (Equation 19) to the input data. The output file is a 9-column file that has the X and Y coordinates, the raw values of the different maps, the rescaled values of the different maps and the final sum of the rescaled values. The combine source code, *combine.c*, and the executable, **combine.exe**, are located in the \Monitoring_04\combine\ subdirectory on the CD-ROM.

Results of the **combine** code can be verified by visual inspection of the output file and comparison of the rescaled maps (Figures 27, 28, 29 and 30) to the raw value maps (Figures 5, 14, 24 and 25). Additionally, for any row in the output file, the value in the 9th column must be the sum of the values in the 6th, 7th and 8th columns. The combine code was run twice, once with the third input file being *sens.WTime_to_t.map* and once with the third input file being *sens.WTime_to_h.map*. The two output files are *combine_T.xyz* and *combine_h.xyz* and are contained in the \Monitoring_04\combine\ subdirectory on the CD-ROM included with this analysis package.

6.0 Additional Monitoring Wells

Eight new wells have been added to the historical monitoring network to bring the total number of monitoring wells to 38. The effect of adding these new wells to the monitoring network is examined by recalculating the estimation variance map and the three-point estimator map. The main goal of this study is to identify optimal locations for the addition of future wells. The well removal calculations done previously on the original 30 well data set are not repeated here. The new wells have been drilled and developed, but they are not yet providing stable estimates of the heads in the Culebra. Therefore, the sensitivity of travel time to T and head values in these new wells cannot yet be calculated. The new estimation variance and three-point estimator maps are combined with the existing sensitivity maps to produce a set of updated maps for optimal placement of additional monitoring wells.

6.1 Expanded Data Set

The well locations and head data for the 30 wells in the historical data set are shown in Table 3. Eight new wells are added to this network and the locations of these wells and the heads at the wells estimated as the average of the heads across the 100 calibrated T fields (McKenna and Hart, 2003; Beauheim, 2003) are shown in Table 13.

Table 13. New monitoring wells and estimated heads

Integer ID	Well Name	X Coordinate (m)	Y Coordinate (m)	Estimated Freshwater Head (m)
31	C-2737	613597	3581401	921.93
32	IMC-461	606180	3582240	925.98
33	SNL-1	613782	3594302	943.58
34	SNL-2	609113	3586529	933.25
35	SNL-3	616103	3589047	938.59
36	SNL-5	611970	3587285	936.27
37	SNL-9	608705	3582238	927.41
38	SNL-12	613210	3572728	910.18

6.2 Variogram Calculation

The addition of eight wells to the monitoring network necessitates recalculation of the variogram defining the spatial correlation of the head data. The original variogram was calculated on the residuals between the measured head data and a best-fit plane through the data to remove the trend. With the addition of eight new wells, there appear to be enough head measurements to accurately estimate heads at unmeasured locations using ordinary kriging without first removing the trend from the data. Therefore the variogram for the updated monitoring network of 38 wells is calculated on the actual measured and estimated heads. This variogram is shown in Figure 33 and can be compared to the residual variogram in Figure 4.

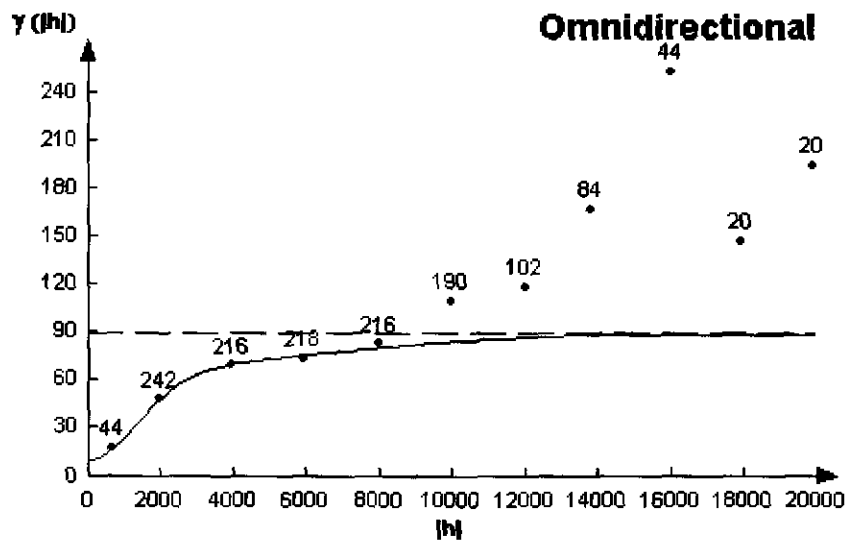


Figure 33. Experimental omnidirectional variogram (points) and analytical model variogram (line) fit to it. This variogram is for the actual measured and estimated heads.

This experimental variogram was fit with a nested model where a Gaussian model is used to fit the points at relatively low separation distances and a spherical model is used for points at the larger separation distances. The Gaussian model fit to the experimental variogram in Figure 33 has a nugget value of 10 m^2 , a sill of 50 m^2 and a range of 3300 m . The spherical model has a sill of 30 m^2 and a range of $15,000 \text{ m}$. The sum of the nugget and two sills was constrained to reach a maximum at the covariance of the residual data set, 90 m^2 , as shown by the horizontal dashed line in Figure 33. The numbers of data pairs that were used for the calculation of each point in the experimental variogram are also shown in Figure 33. As was done in the original data set, the calculation of the experimental variogram was done by considering combinations of pairs of data points in all directions, an “omnidirectional calculation”. Due to the limited number of head data, 38, it was not possible to calculate directionally dependent variograms that might show anisotropy in the spatial correlation of the residuals. The experimental variogram points beyond a separation distance of 9000 m and above the level of the covariance represent negative spatial correlation

A major difference between the variograms calculated with 30 and 38 data points is in how quickly they reach the final sill value. The variogram from the original 30 data (Figure 4) reaches 50 percent of the final sill value, or 29.1 m^2 , at a separation distance of 3800 meters . The variogram calculated on the 38 data (Figure 33) reaches a value of 50 percent of the final sill, a value of 45 m^2 , at a separation distance of approximately 1900 meters , or half the distance of the original variogram. This more rapid rise in the variogram model will result in more localized decreases in kriging variance around individual wells than were calculated for the original data set.

6.3 Estimation Variance Calculations

The same procedure and software used in the calculation of the estimation variance from the 30-well data set is also used here for the expanded data set. The resulting map of estimation variance for the expanded (38-well) monitoring network is shown in Figure 34. From Figure 34, the effect of the monitoring network configuration on the resulting estimates of variance is obvious. The lowest estimation variance values, the nugget value of 10.0, occur at the well locations and the highest values occur at locations that are beyond the distance of the largest variogram range, 15,000 meters, from the closest observation well. The minimum possible value of the kriging variance is the value of the nugget in the variogram model. Therefore, complete coverage of the site by the monitoring network would result in an estimation variance of 10.0 at all locations. Under ideal conditions, the maximum possible value of the kriging variance is equal to the total sill of the variogram, 90.0 m² in this case; however, in cases where data points are clustered, such as within the WIPP site, screening of some data by others can result in negative kriging weights that cause the kriging variance to increase above the level of the sill. The maximum kriging variance in these calculations is approximately 120 m².

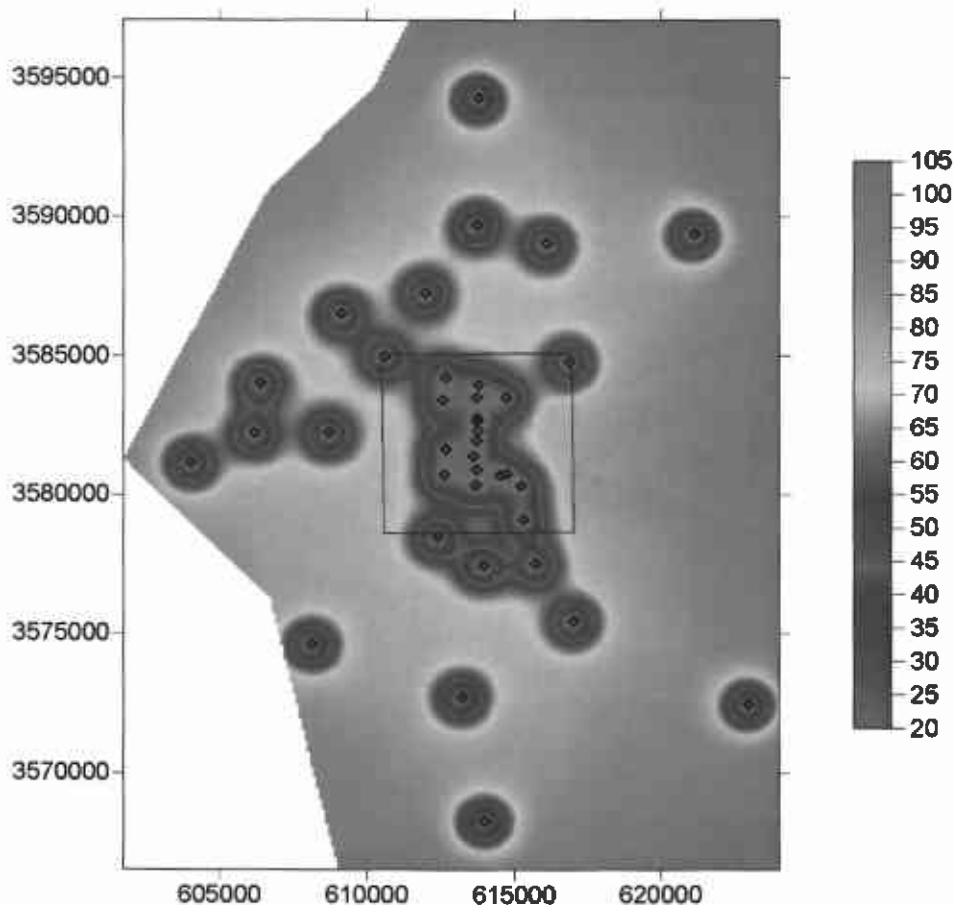


Figure 34. Kriging variance (m²) for estimation of the heads using the 38-well monitoring network.

From the map in Figure 34, it is obvious that there are many locations outside of the WIPP site where the addition of a well would have maximum impact on reducing the estimation variance. These locations are wherever a well could be located where its influence does not overlap on the region of decreased variance from an already existing monitoring well. Within the WIPP site, the estimation variance is already relatively low at all locations. In fact, given the small distances between some wells relative to the range of the variogram, it may be possible to remove some of the existing wells with only minimal increase in the estimation variance within the WIPP site boundary. The well removal calculations are not redone here, but given that only one of the eight new wells was located within the WIPP site, the kriging variance changes within the WIPP site as calculated in section 2.4 should remain relatively unchanged.

Figure 34 shows similar results to the calculation of estimation variance with the 30-well network in that many locations can be identified where a new monitoring well will have maximum impact on the reduction of the overall estimation variance. These areas are generally in the corners of the flow model domain and to the east of the WIPP site. Comparing Figures 5 and 34 shows the effect of adding the eight new wells to the monitoring network on the estimation variance.

6.4 Addition of New Monitoring Wells Using Three-Point Estimators

The local gradient estimator built on three wells is used to determine optimal locations for new wells to be added to the network. This analysis is the same as that done above with the exception that the existing network is now the expanded 38 well network. The number of acceptable three-point estimators produced by locating a new well at any location in the domain is calculated subject to the constraints on the shape of the estimator and the RHME as defined previously. The same set of 100 calibrated heads used previously is also used in this analysis.

The addition of a new well to the existing monitoring network can only increase the number of acceptable estimators. Without the shape or RHME criteria, the maximum possible number of estimators from 38 wells is 8436 (Equation 12). Addition of another well, 39 total wells, increases the maximum possible number of estimators to 9139, an increase of 703. If the additional well can be placed such that all additional estimators created from that well meet both criteria, then the increase in the number of acceptable estimators will be 703. This number serves as an upper bound on the possible number of new estimators.

On average, addition of a new well to the Culebra network creates a total of 4844 acceptable three-point estimators, or an increase of 2744 (131 percent) over the average of 2100 estimators created from adding an additional well to the 30-well network.

The results of the well-addition calculations are shown as a map in Figure 35. Locations where the addition of a well will increase the number of acceptable estimators the most are generally in the areas surrounding the outside of the WIPP site. A well added in these areas can take advantage of the large number of existing wells within the WIPP site to create estimators that meet both the shape and RHME criteria. Exceptions to these areas are locations between the WIPP site and locations where wells already exist. The areas of highest return do not extend all the way to the edges of the domain because either the no-flow region restricts the number of

triangles that can be created or, in the NE corner of the domain, the addition of a single new well is not enough to create a large number of triangles in the relatively isolated region of the site. A relative comparison of the effect of adding the 8 new wells to the monitoring network can be made by comparing the results in Figure 35 with those in Figure 14. The patterns in the two maps can be compared, but the absolute values cannot. There are some subtle changes in the shape of the map between the two monitoring networks, but the general areas outside of and surrounding the WIPP site with the largest return for a new well are similar. An additional well within the WIPP site will produce the smallest increase in the number of acceptable estimators as this area already has a large number of wells and the majority of the estimators created by an additional well within this area will not be large enough to achieve the necessary head drop to meet the RMHE criterion.

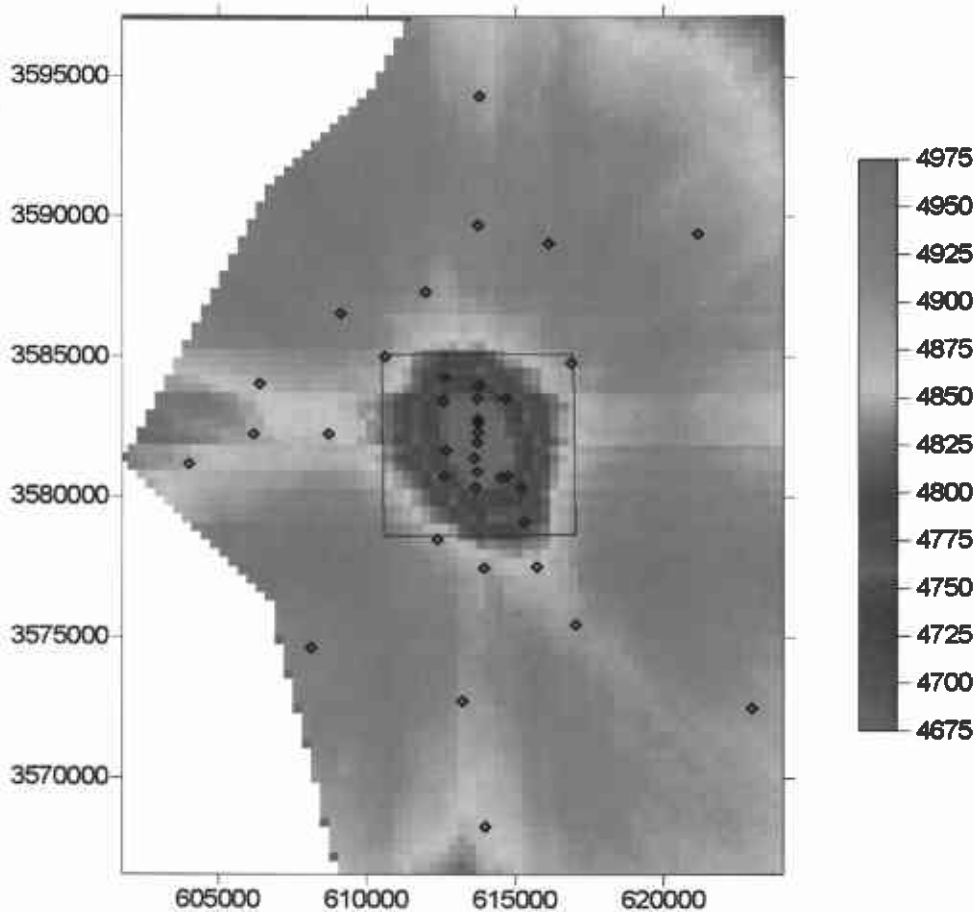


Figure 35. Number of acceptable local gradient estimators for a single new well placed at any location within the domain. Addition of a single well to the original 30-well network produces, on average, 2100 estimators.

6.5 Combining Monitoring Approaches

The same approach of normalizing the values of each map to a {0,1} scale and then adding the maps together to get a final combined score map is used with the results from the expanded

monitoring network. The maps showing the sensitivity of the travel time to both head and T have not changed and the scaled sensitivity maps in Figures 29 and 30 are used in this analysis. The scaled versions of the maps showing the estimation variance and the number of acceptable three-point estimators are shown in Figures 36 and 37, respectively. These figures can be compared to Figures 27 and 28 to see the effect of the additional eight wells in the monitoring network. It is especially interesting to compare the results in Figure 37 with those in Figure 28 for the northeast corner of the domain. The green region of smaller numbers of additional triangles due to an additional well in that area nearly disappears after the addition of the eight new wells. Addition of these new wells, especially SNL-1 and SNL-3, make this northeast corner of the domain a much more productive location for additional monitoring wells. The lack of wells near this corner in the 30-well network has been overcome, to some extent, by the addition of the 8 new wells, and an additional well in this northeast area would provide a significant number of acceptable three-point estimators.

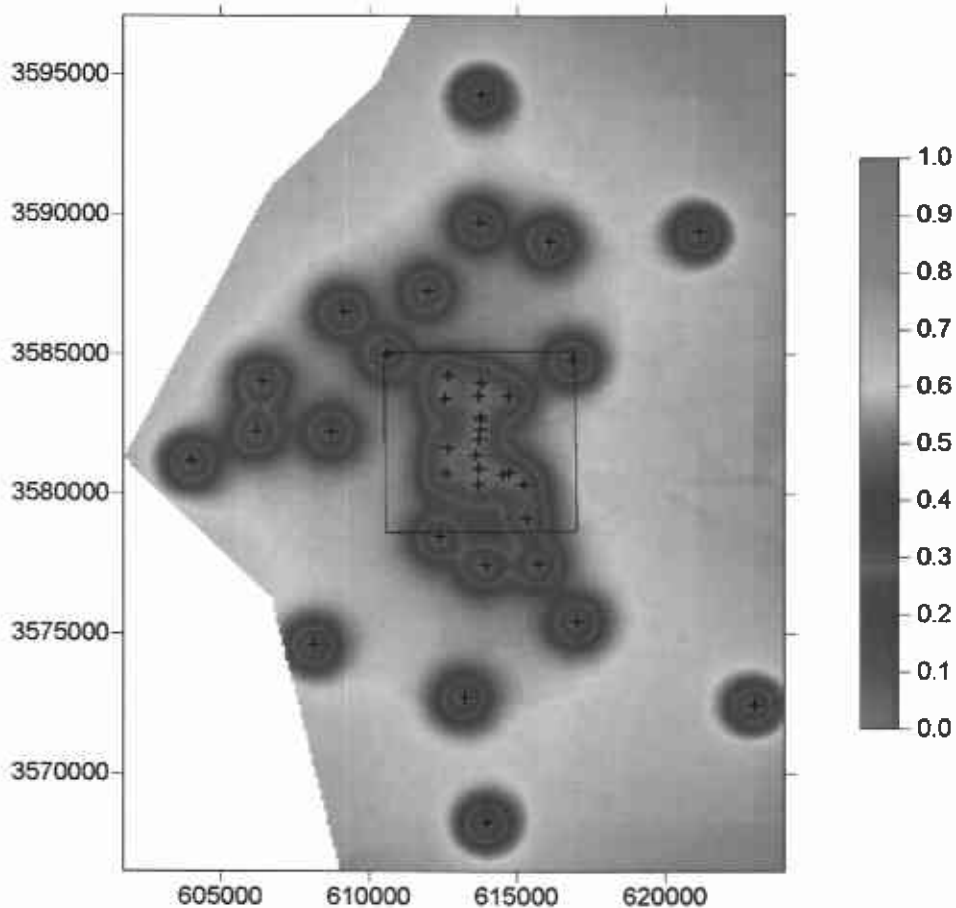


Figure 36. Rescaled [0,1] estimation variance map. The wells in the expanded monitoring network and the WIPP site boundary are shown.

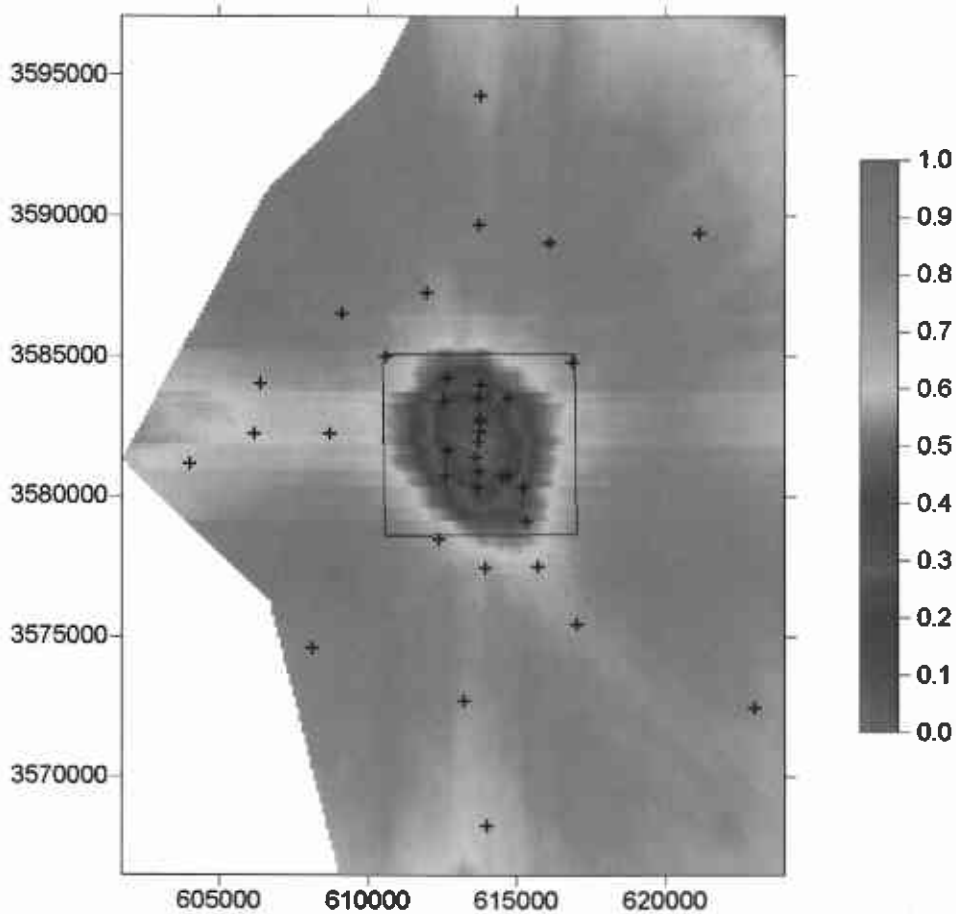


Figure 37. Rescaled [0,1] number of acceptable three-point estimators map. The wells in the expanded monitoring network and the WIPP site boundary are shown.

The final maps of the combined score values are shown in Figures 38 and 39. The theoretical minimum and maximum combined score values for any location are 0.0 and 3.0 respectively. The calculated minimum and maximum combined score values when the sensitivities of travel time to head are one of the components (Figure 38) are 0.1 to 2.4, respectively; when the sensitivity of travel time to transmissivity is included as a component (Figure 39), the maximum and minimum values are 0.10 and 2.2.

The combined score map that includes sensitivity of travel time with respect to head (Figure 38) shows the highest combined scores to the west, south and east of the WIPP site. The lowest scores occur within the WIPP site boundaries. These results are consistent with the results obtained using the historical monitoring network. The character of the three component maps is evident in the final combined score map, which is controlled mainly by the rescaled estimation variance map (Figure 36) and the rescaled sensitivity of the travel time to the estimated heads map (Figure 29). The area of high combined scores to the east of the site is to the east of the low transmissivity boundary. The high values of the combined score in this area are caused by high

values of all three components (Figures 36, 37, and 29), but it is noted that only one of these three components is directly based on solution of the groundwater flow model (Figure 29). The high component scores in this region east of the site for the estimation variance and the three-point estimators are due mainly to the paucity of monitoring wells in this area.

Relative to the results obtained using the historical monitoring network, the addition of the eight new wells to the monitoring network is readily apparent. The areas of lower combined score around each well in Figure 38 are smaller than those obtained using the historical network (Figure 31) and this is due mainly to the change in the variogram shape between the historical and expanded networks. The area directly south of the WIPP site has a very high combined score and the reduction of the estimation variance at the location of SNL-12 is relatively localized due to the large values of the number of acceptable estimators and high sensitivity of travel time to head at this location. The variogram calculated with the 38-well network makes the areas of combined score shown in green in Figure 38 thinner and less connected compared to the original 30-well network seen in Figure 31.

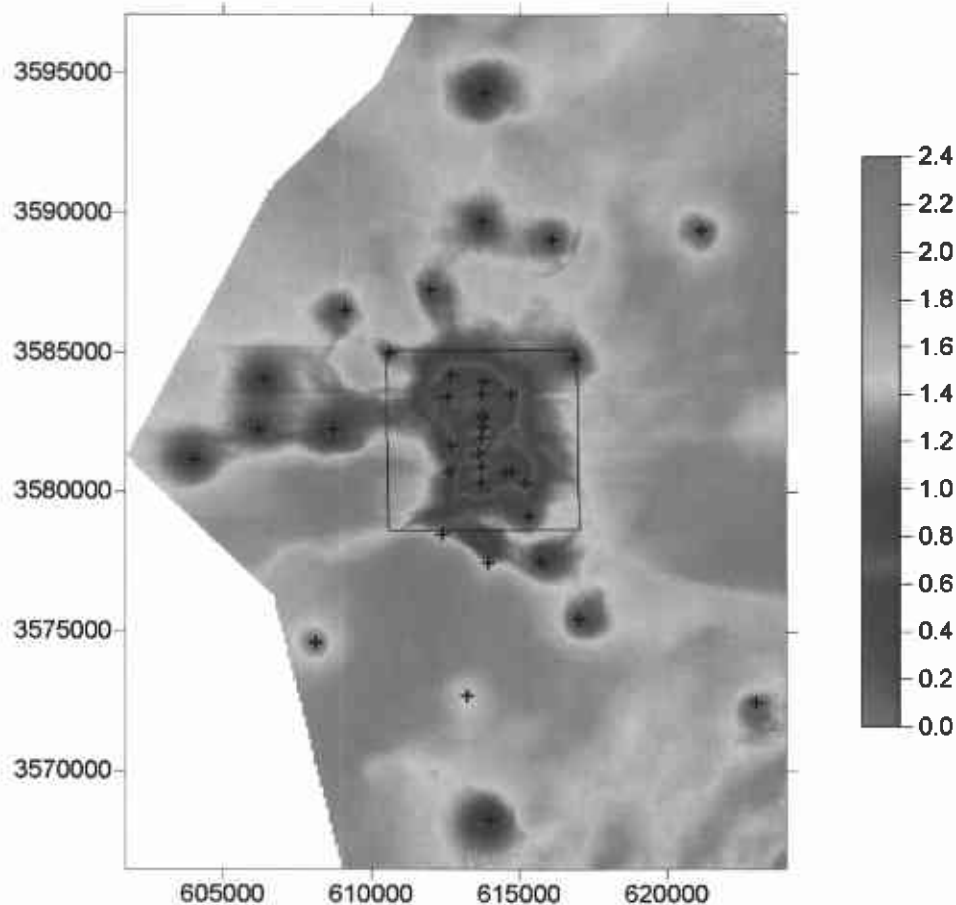


Figure 38. Combined score values map including estimation variance, number of three-point estimators and sensitivity of travel time to head. The wells in the expanded monitoring network are shown as plus signs.

The combined score map that includes the sensitivity of the travel time to the calibrated transmissivities (Figure 39) shows that the lowest combined scores occur in the center of the WIPP site and this area is not optimal for the location of additional monitoring wells. The locations with the highest combined scores are much more localized than are the results obtained when the sensitivity of the travel time to the estimated head is used. The rescaled sensitivity of travel time to T map (Figure 30) shows the highest sensitivities occurring directly south of the center of the WIPP site, directly south of the east side of the WIPP site and along the bottom of the model domain. Compared to the results for the original 30-well network, the 38-well network combined score results show that the effect of any single well is more localized and this is due to the different variogram shapes between the two data sets. The high score location just south of the center of the WIPP site is seen in both combined score maps (Figures 32 and 39).

Further characterization of the high sensitivity locations to the south of the WIPP site will directly address PA-driven monitoring goals. The area of high sensitivity along the southern boundary of the domain is most likely connected to the relationship between the assigned head boundary condition there and the calibrated T values in that area. This high sensitivity region indicates that calibrated T's in this area do have some level of control on travel times to the WIPP site boundary, most likely by controlling the direction that the particles take from the release point to the WIPP site boundary.

The two combined score maps, Figures 38 and 39, show somewhat similar results for the locations of the calculated regions of high and low scores. This result is not surprising given that two of the components in each map are identical: the estimation variance and number of three-point estimators (Figures 36 and 37). Therefore the differences in the combined score maps are due to differences in the travel time sensitivity maps (Figures 29 and 30).

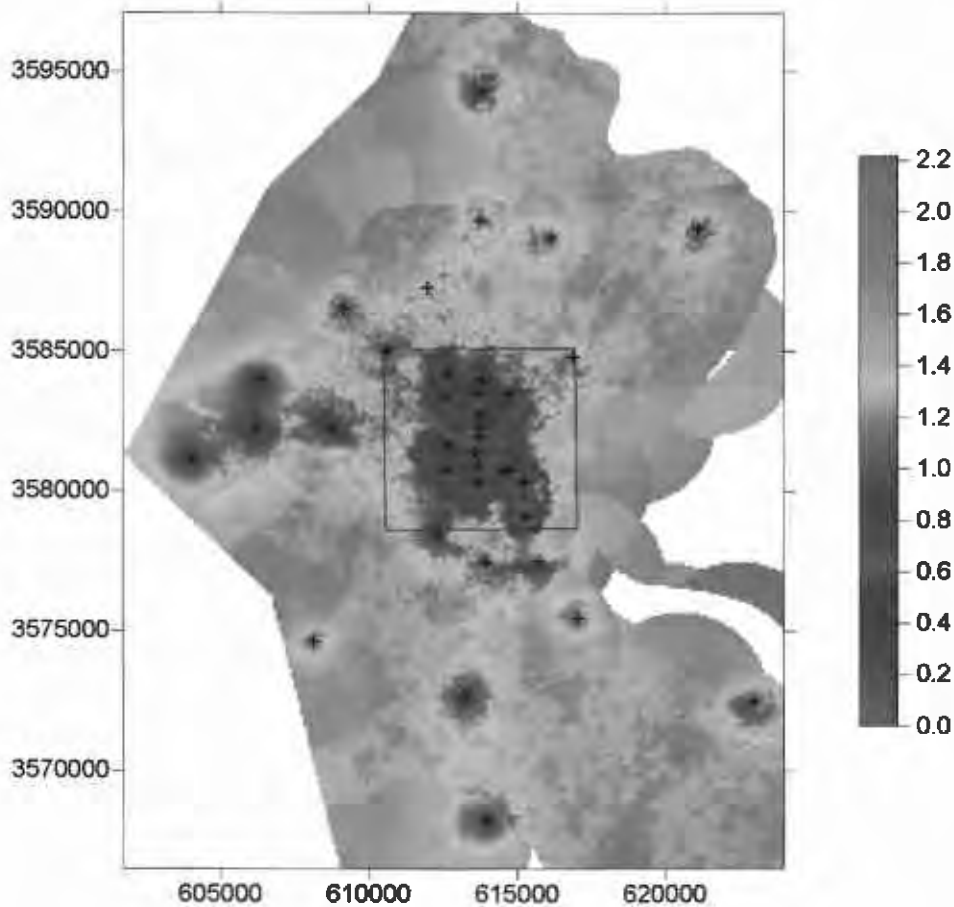


Figure 39. Combined score values map including estimation variance, number of three-point estimators and sensitivity of travel time to transmissivity. The wells in the expanded monitoring network are shown as plus signs.

6.6 Calculation Details

All calculations for the combined score maps are made in the *Monitoring_04\Add_8* subdirectory on the CD-ROM included as part of this analysis package. No new codes were written for these analyses. Existing codes used in the calculations on the historical data set were used for the same calculations on the expanded data set.

7.0 Conclusions

A set of 30 head monitoring wells in the Culebra within and surrounding the WIPP site provided head data at two time periods: August 2000 and August 2003. This head monitoring network provided the input data for three different approaches to optimizing the monitoring well network. Optimization is interpreted broadly here to include both the identification of new locations where wells could be added to the network to meet some objective and also identification of existing wells that could be removed from the monitoring network as they provide redundant information. The three different approaches to monitoring network optimization examined here are: 1) geostatistical variance reduction; 2) local gradient estimation using combinations of three wells; and 3) sampling-based spatial sensitivity coefficients.

7.1 Summary of Calculations

Geostatistical variance reduction is a fairly common optimization approach that exploits several properties of the kriging variance to identify new locations where a well could be added to an existing monitoring network to provide the greatest reduction in estimation variance. The same calculational approach can be used to determine existing wells that, upon removal from the monitoring network, provide the smallest increase in the overall estimation variance. Kriging provides an ideal approach to these calculations as the estimation variance calculated through kriging is only a function of the data configuration and not the data values. Therefore, the estimation variance reduction/increase for the addition/removal of a new well can be calculated prior to adding/removing that well from the network. This calculation assumes that the variogram calculated for the head, or residual, values in the network does not change with the addition/removal of a well.

Application of the geostatistical estimation variance calculations to the Culebra network shows that there are many locations where a well can be added to the network that will produce a maximum reduction in the average estimation variance. These locations are all outside of the WIPP site boundaries and the majority of these locations are to the north and to the east sides of the calculation domain. Adding new wells within the WIPP site boundary will not have a significant impact on the estimation variance. The geostatistical estimation variance calculations were also applied to the problem of determining which existing wells to remove from the network. Results for this problem can easily be calculated; however, for removal of more than one well at a time, it is necessary to know what combinations of wells need to be removed to make the problem tractable. Three different base cases were run here and the results show that simultaneous removal of the WIPP-12 and WIPP-22 wells makes an insignificant change in the estimation variance relative to the full 30-well network, while removal of the H-12 and P-17 wells has a significant impact. Beyond these results, some combination of the ERDA-9, H-3, WIPP-19 and WIPP-21 wells should be examined for removal. The largest increases in variance occur when AEC-7, H-5, WIPP-30, H-9 and H-10 are removed from the network. These wells, or replacements, are most important to keep in the monitoring network. The well removal calculations for three different base cases are summarized in Table 14.

Local gradient estimators have been employed previously to identify flow directions and magnitudes in aquifers from combinations of 3 wells. However, previous work has not identified the conditions under which these local gradient estimators give accurate results. Work in this report identified triangles with base to height ratios between 0.5 and 5.0 as giving the best results. Additionally, the size of the estimator necessary to limit the relative head measurement error in the Culebra monitoring program to less than two percent of the expected head drop across any estimator was determined. Using these two constraints to identify acceptable local gradient estimators reduces the number of combinations of three wells from 4060 to 1879. Two uses of local gradient estimators for long-term monitoring of gradients were developed. The first technique identifies changes in the orientation and magnitude of the local gradients over time. An example calculation was completed using the August 2000 and August 2003 water level data and the majority of changes in flow direction and orientation were found to be minimal. The three-point estimators exhibiting larger changes can now be examined in detail to identify a root cause of these changes. The second monitoring technique using local gradient estimators was designed to identify the best places to locate additional monitoring wells and the existing wells that could be removed from the network with the smallest impact on the ability of the network to detect changes in the gradient.

Results of the calculations to identify locations for additional monitoring wells show that new wells should be located outside of the WIPP site. With the exception of the northeast corner of the model domain and an area directly west of the WIPP site, locating a new well at almost any location outside of the WIPP site could provide nearly the same increase in the number of acceptable local gradient estimators. The recent addition of eight new wells to the monitoring network makes the northeast corner of the domain, a region where the geologic and hydrologic conceptual model is currently poorly constrained, a productive location for the siting of a new monitoring well. The hydraulic gradient in the region directly west of the WIPP site is already adequately constrained. The well removal calculations were done by removing one well at a time from each of three base case scenarios. Similar to the geostatistical estimation variance calculations, the removal of wells WIPP-12 and WIPP-22 from the original network of 30 wells has little impact on the monitoring network performance. Further removal of wells H-12 and P-17 does have a significant impact on the monitoring network. The next best wells to remove in terms of impacting the monitoring network in a minimal way are some combination of ERDA-9, WIPP-21, H-3, and WIPP-19. The wells that are most important for the continued operation of the monitoring network include WIPP-25, WIPP-30, H-7 and H-5. H-12 is also shown to be an important well to replace. The well removal results for the three different starting cases are summarized in the right-most three columns of Table 14.

Table 14. Relative importance of existing wells in the monitoring network. X = least important, O = most important. Blank boxes indicate moderate importance. Wells removed for the starting case are denoted “NA”.

Well	Geostatistical Variance Reduction			Three-Point Estimators		
	All Wells	2 Removed	4 Removed	All Wells	2 Removed	4 Removed
AEC-7	O	O	O			
DOE-1						
ERDA-9	X	X	X	X	X	X
H-2						
H-3	X	X	X		X	X
H-4			O			
H-5	O	O	O	O	O	O
H-6						
H-7				O	O	O
H-9	O	O				
H-10	O	O	O			
H-11						
H-12			NA	O	O	NA
H-17						O
P-17			NA			NA
WIPP-12	X	NA	NA	X	NA	NA
WIPP-13						
WIPP-19	X	X	X	X	X	X
WIPP-21	X	X	X	X	X	X
WIPP-22	X	NA	NA	X	NA	NA
WIPP-25				O	O	O
WIPP-26						
WIPP-30	O	O	O	O		O

The third approach to monitoring network optimization explored in this report is that of using spatial sensitivity coefficients to identify locations for new wells where some model output of interest (e.g., travel time) is most sensitive to the transmissivity or head at that location. This approach only provides locations for new wells – it does not examine removal of wells from the existing network. These sensitivity coefficients are calculated through a sampling-based technique across 100 calibrated transmissivity fields and are shown to be appropriate when compared to sensitivity coefficients calculated using a derivative-based approach for the overall calibration of the flow model to the observed heads. The sampling-based sensitivity coefficients are shown as a map of the sensitivity of the travel time from the repository to the WIPP site boundary with respect to head and transmissivity. The results with respect to head show a smoothly varying sensitivity field with large regions of positive and negative correlation between head and travel time. The results with respect to transmissivity have much more localized regions of positive and negative correlation with travel time being most sensitive to

transmissivity at a location directly south of the WIPP site boundary. It is noted that increased knowledge of the spatial variation of the Culebra transmissivity is not a goal of the long-term monitoring network, but transmissivity is an input to the T field calibration process used as input to further PA calculations.

As a final step, the results of the geostatistical estimation variance calculations, the local gradient estimation and the spatial sensitivity coefficients were combined into two “combined score” maps. These maps show, on a scale from 0.0 to 3.0, the best locations to locate new monitoring wells. In general, these areas are outside of the WIPP site. Eight new well locations are compared to these final combined score maps and the majority of these new locations are already in high combined score regions.

7.2 Reexamination of Monitoring Goals

The different purposes, goals and factors that must be taken into account in the design of the Culebra long-term monitoring network were stated in Section 1.2. These goals come from a variety of sources, mainly the state and federal regulatory bodies with WIPP oversight and the ability of the network to provide needed inputs to PA models. Practical factors impacting network design require that the total number of wells in the monitoring network be minimized and that certain wells be retained in the network. The monitoring network should also serve as a vehicle to provide new information to the hydrologic and geologic conceptual models.

The first monitoring network goal is to allow for *determination of the direction and rate of groundwater flow across the WIPP site*. Network optimization techniques using three-point estimators were developed specifically to meet this goal (Section 3.0). Independently obtained head measurements cannot by themselves determine the direction and magnitude of the hydraulic gradient. For a confined aquifer with a mainly two-dimensional flow pattern, head measurements at three separate locations are necessary to determine the orientation and magnitude of the gradient. The techniques developed and demonstrated in this work provide for: 1) determining what three-point estimators will give the best estimates of the gradient under the inherent water-level measurement error; 2) monitoring temporal changes in the gradient; 3) identifying where new wells would provide the most benefit; and, 4) identification of wells that are providing redundant information. Model studies done to assess the impact of aquifer heterogeneity indicate that good estimates of the flow direction and magnitude of the gradient on the WIPP site can be identified with three-point estimators contained fully, or partially, within the WIPP boundary that have areas between one-eighth of the size of the WIPP site and two and a half times the size of the WIPP site.

The second monitoring goal is to *provide data needed to infer causes of changes in water levels*. Detecting water level change can be done in a single well and an implicit requirement to meet this goal is that there are enough wells in key locations both within and around the WIPP site to detect any water level changes. Checking for the adequate distribution of wells in and around the WIPP site is accomplished using a geostatistical variance reduction approach (Section 2.0). These calculations identify where additional wells are needed and which existing wells can be removed from the network. After a change in water level is detected, the cause of that change must be inferred. There must be enough wells in the proper configuration to infer the cause of a change. The geostatistical variance reduction and three-point estimator approaches to

monitoring network design provide networks that maintain enough well density with the proper configurations to infer causes of changes. An example of detecting changes in the magnitude and orientation of the gradient from August 2000 to August 2003 at more than 1800 locations within the analysis domain is demonstrated in Section 3.0.

The third goal is that the *monitoring network must provide spatially distributed head data adequate to allow both defensible boundary conditions to be inferred for Culebra flow models and defensible calibration of those models*. This goal is related to the previous one in that a network that provides enough wells with the spatial distribution and configuration to detect and infer causes of changes in water levels should also provide the data necessary to infer boundary conditions and calibrate Culebra flow models. Therefore both the geostatistical variance reduction and the three-point estimator approaches and the data gaps and redundancies that they identify apply to this goal as well. Additionally, a third approach to monitoring network design based on sensitivity analysis was developed to explicitly incorporate the results of calibrated groundwater flow models directly into the monitoring network design. The set of calibrated groundwater models used as the basis of this third approach incorporates the latest geologic and hydrologic conceptual models. This approach to monitoring network design defines areas along the boundaries and within the groundwater flow model where the model results are most sensitive to the calibrated values of head and transmissivity. Regions of high sensitivity are targeted for future well locations.

In addition to meeting these three goals, a number of other factors were considered in the design of the monitoring network. These included preserving the locations of existing fiberglass and steel-cased wells, identifying wells that provide redundant information, incorporating current hydrologic and geologic conceptual models and identifying locations where questions in the conceptual models can be addressed and/or locations where the groundwater flow models used in PA calculations are sensitive to the local values of head and transmissivity. Both the geostatistically-based variance reduction approach and the three-point estimator approach to monitoring network design explicitly considered minimization of the number of wells in the monitoring network through removal of existing wells. Tradeoffs between the minimization of the wells in the network and the ability of the network to provide information on changes in heads were examined. The monitoring network design done here was focused on optimization approaches that are readily quantified into different objective functions. Meeting certain, less easily quantified, factors such as locations where conceptual model questions can be addressed is more difficult and the monitoring networks designed here did not explicitly address this factor.

The results of the calculations done to meet the monitoring goals and the other factors are combined into a series of maps that show the best locations for adding wells to the monitoring network. A table has also been created showing which existing wells are the most and least important to maintain within the monitoring network. Overall these maps and this table show that the WIPP Culebra program must move from a well network that is the result of a site characterization driven drilling program where the majority of the wells were located within the site boundary to a more process and conceptual model driven well network that can identify and quantify changes in the Culebra water levels.

8.0 References

- Beauheim, R.L. and S.A. McKenna, 2003, Analysis Plan for Optimization and Minimization of the Culebra Monitoring Network for the WIPP, AP-111, Revision 0, 22 pp, Sandia National Laboratories, Carlsbad, NM, WIPP Records Center.
- Beauheim, R.L., 2003, Analysis Report for AP-100, Task 1, Development and Application of Acceptance Criteria for Culebra Transmissivity (T) Fields, ERMS# 531136, Sandia National Laboratories, Carlsbad, NM, WIPP Records Center.
- Burgess, T.M., R. Webster and A.B. McBratney, 1981, Optimal Interpolation and Isarithmic Mapping of Soil Properties: IV Sampling Strategy, *Journal of Soil Science*, 32, pp. 643-659.
- Cole, B.E. and S.E. Silliman, 1996, Estimating the Horizontal Gradient in Heterogeneous Unconfined Aquifers: Comparison of Three-Point Schemes, *Ground Water Monitoring and Remediation*, Spring, pp. 84-91.
- Conover, W.J., 1980, *Practical Nonparametric Statistics*, Second Edition, John Wiley and Sons, New York, 493 pp.
- Conwell, P.M., S.E. Silliman and L. Zheng, 1997, Design of a Piezometer Network for the Estimation of the Sample Variogram of the Hydraulic Gradient: The Role of the Instrument, *Water Resources Research*, 33 (11), pp. 2489-2494.
- Deutsch, C.V. and A.G. Journel, 1998, *GSLIB: Geostatistical Software Library and User's Guide, Second Edition*, Oxford University Press, New York, 369 pp.
- Devlin, J.F., 2003, A Spreadsheet Method of Estimating Best-Fit Hydraulic Gradients Using Head Data From Multiple Wells, *Ground Water*, 41 (3), pp. 316-320.
- DOE (U.S. Department of Energy). 2004. *Title 40 CFR Part 191 Compliance Recertification Application for the Waste Isolation Pilot Plant, March 2004*. DOE/WIPP 2004-3231. Carlsbad, NM: US DOE Waste Isolation Pilot Plant, Carlsbad Field Office.
- DOE (U.S. Department of Energy). 2003. *Strategic Plan For Groundwater Monitoring at the Waste Isolation Pilot Plant*, DOE/WIPP 03-3230. Carlsbad, NM: U.S. DOE Waste Isolation Pilot Plant.
- Doherty, J., 2000, *PEST2000 Upgrade Notes*, Watermark Numerical Computing, Brisbane, Australia, 34 pp., <http://members.ozemail.com.au/~wnc/wnc.htm>.
- EPA (U.S. Environmental Protection Agency). 1996. "40 CFR Part 194: Criteria for the Certification and Re-Certification of the Waste Isolation Pilot Plant's Compliance with the

40 CFR Part 191 Disposal Regulations; Final Rule," *Federal Register*. 61(28):5224-5245, February 9, 1996. Washington, D.C.: Office of Radiation and Indoor Air.

Gilbert, R.O., 1987, *Statistical Methods for Environmental Pollution Monitoring*, Van Norstrand Reinhold, New York, 320 pp.

Goovaerts, P., 1998, *Geostatistics for Natural Resources Evaluation*, Oxford University Press, New York,.

Graettinger, A.J. and C.H. Dowding, 2001, Quantifying Exploration Sufficiency While Accommodating Judgment, *Mathematical Geology*, 33 (2), pp. 133-154.

Helton, J.C., and M.G. Marietta (editors). 2000. The 1996 Performance Assessment for the Waste Isolation Pilot Plant, Special Issue of: *Reliability Engineering and System Safety*, Vol 69, No. 1-3.

Helton, J.C., J.E. Bean, J.W. Berglund, F.J. Davis, K. Economy, J.W. Garner, J.D. Johnson, R.J. MacKinnon, J. Miller, D.G. O'Brien, J.L. Ramsey, J.D. Schreiber, A. Shinta, L.N. Smith, D.M. Stoelzel, C. Stockman, and P. Vaughn. 1998. *Uncertainty and Sensitivity Analysis Results Obtained in the 1996 Performance Assessment for the Waste Isolation Pilot Plant*. SAND98-0365. Albuquerque, NM: Sandia National Laboratories.

Helton, J.C. and F.J. Davis, 2000, Sampling-Based Methods for Uncertainty and Sensitivity Analysis, SAND99-2240, Sandia National Laboratories, Albuquerque, New Mexico, 101 pp.

James, B.R., and S.M. Gorelick, 1994, When Enough is Enough: The Worth of Monitoring Data in Aquifer Remediation Design, *Water Resources Research*, 30 (12), pp. 3499-3513.

Jones, S.B. 2003. Transmittal of the Water Level Data for August 2003. Letter to Dr. Dave Kessel, Sandia National Laboratories, August 31, 2003. WRES:03:601, UFC:5480.00. Carlsbad, NM: Washington Regulatory and Environmental Services.

Loaiciga, H., 1989, An Optimization Approach for Groundwater Quality Monitoring Network Design, *Water Resources Research*, 25, pp. 1771-1782.

McKenna, S.A. and D.B. Hart, 2003, Analysis Report, Task 4 of AP-088, Conditioning of Base T Fields to Transient Heads, ERMS# 531124. Sandia National Laboratories, Carlsbad, NM, WIPP Records Center.

Meyer, P., A.J. Valocchi and J.W. Eheart, 1994, Monitoring Network Design to Provide Initial Detection of Groundwater Contamination, *Water Resources Research*, 30(9), pp. 2647-2659.

Mizell, S.A., 1980, Stochastic Analysis of Spatial Variability in Two-Dimensional Groundwater Flow with Implications for Observation Well Network Design, unpublished dissertation, New Mexico Institute of Mining and Technology, Socorro, New Mexico, 133 pp.

- NMAC (New Mexico Administrative Code), 2000, 20.4.1 NMAC, Subpart V, §264.13, and Subpart VIII, §268.35(d).
- Olea, R.A., 1984, Sampling Design Optimization for Spatial Functions, *Mathematical Geology*, 16 (4), pp. 369-392.
- Olea, R.A., 1999, *Geostatistics for Engineers and Earth Scientists*, Kluwer Academic Publishers, Netherlands, 324 pp.
- Pannatier, Y., 1996, *VarioWin: Software Spatial Analysis in 2D*, Springer, New York, 91 pp.
- Rouhani, S., 1985, Variance Reduction Analysis, *Water Resources Research*, 21 (6), pp. 837-846.
- Ruskauff, G.J., and J.O. Rumbaugh III, 1996. Incorporating ground water flow direction and gradient into flow model calibration. In Proceedings of 1996 ModelCARE, Golden, CO, pp. 71-81.
- Silliman, S.E., and C. Frost, 1998, Monitoring Hydraulic Gradient Using Three-Point Estimator, *Journal of Environmental Engineering*, June, pp. 517-523
- Silliman, S.E. and G. Mantz, 2000, The Effect of Measurement Error on Estimating the Hydraulic Gradient in Three Dimensions, *Ground Water*, 38 (1), pp. 114-120.
- Storck, P., J.W. Eheart and A.J. Valocchi, 1997, A Method for the Optimal Location of Monitoring Wells for Detection of Groundwater Contamination in Three-Dimensional Heterogeneous Aquifers, *Water Resources Research*, 33 (9), pp. 2081-2088.
- Supriyasilp, T., A. J. Graettinger and S. R. Durrans, 2003, Quantitatively Directed Sampling for Main Channel and Hyporheic Zone Water-Quality Modeling, *Advances in Water Resources*, 26, pp. 1029-1037.
- Taylor, J.R., 1996, *An Introduction to Error Analysis: The Study of Uncertainties in Physical Measurements, Second Edition*, University Science Books, Sausalito, California, 327 pp.
- Tuckfield, R.C., E.P. Shine, R.A. Hiergesell, M.E. Denham, S. Reboul and C. Beardsley, 2001, Using Geoscience and Geostatistics to Optimize Groundwater Monitoring Networks at the Savannah River Site, WSRC-MS-2001-00145, Available from the Office of Scientific and Technical Information website: <http://www.osti.gov/bridge> , 18pp.
- Wagner, B.J., 1995, Sampling Design Methods for Groundwater Modeling Under Uncertainty, *Water Resources Research*, 31 (10), pp. 2581-2591.
- WTS, 2003, Washington TRU Solutions Water-Level Data Package, ERMS# 525178.

**Appendices for Analysis Report
AP-111
Culebra Water Level Monitoring Network Design**

**(AP-111: Analysis Plan for Optimization and Minimization of the
Culebra Monitoring Network for the WIPP)**

Task Number 1.4.1.1

Report Date: October 28th, 2004

Sean A. McKenna, Geohydrology Department (6115)

Table Of Contents

Table Of Contents	2
List of Figures	3
List of Tables	4
Appendix 1. Results of Fitting Planar Equation to 2003 Heads Using SigmaPlot Version 8.0	5
Appendix 2. kt3d Parameter File	9
Appendix 3. Well Removal Batch File (<i>krig_min.bat</i>).....	10
Appendix 4: HeadGrad Program	13
Description of HeadGrad Program	13
Execution	13
Input and Output	14
Algorithm and Calculations	15
Verification of the Flux-Weighted Average Gradient	17
Verifying the flux of a grid triangle calculation	18
Verifying the gradient calculation	19
Verifying whether a grid triangle is inside a well triangle.....	21
Verifying the flux-weighted average gradient calculation.....	22
Verification of Well Triangle Gradient Using Nearest Model Cells	23
Reference:	23
Appendix 5. Median_HeadGrad Program	24
Description of Median_HeadGrad Program	24
Execution	24
Input and Output	25
Algorithm and Calculations	25
Verification of Median_HeadGrad	26
Appendix 6. Test of the RHME program.....	27
Appendix 7. Testing the main code for evaluating the effects of estimator shape and gradient orientation.	28
Appendix 8. Test Problem for Well Removal Gradient Estimation	30
Appendix 9. Test Problem for Well Addition Gradient Estimation	36
Appendix 10. Test Problem for Spatial Sensitivity Coefficients.....	41
ParseTestProblem.sh shell file	43
RunTestProblem.sh shell file	43

List of Figures

Figure 1. Visual diagram of the grid triangle flux 19

Figure 2. Grid triangles inside well triangle 244 (*GridTriangles_244.plt*)..... 21

Figure 3. Input file for the main test problem..... 29

Figure 4. Contour map of the regional head field used in this test problem. The units of head are arbitrary..... 32

Figure 5. Locations of the six wells used in the test problem. The well located at (200,490) is removed for the five well test problem. 33

Figure 6. Contour map of the regional head field used in this test problem. The units of head are arbitrary..... 37

Figure 7. Locations of the six wells used in the test problem (diamonds) and the grid of calculated heads used to estimate the number of new triangles from the addition of a single new well at the center of each cell. 39

Figure 8. Comparison of Spearman rank correlation coefficients calculated by vlsap and Excel across all 100 cells in the test problem. 42

List of Tables

Table 1. HeadGrad input and output files 14

Table 2. Extract of *GridTri_Flux_d01r07_263.out*, processed by Excel 19

Table 3. Extract of *WellTri_Grad.out* 20

Table 4. Extract of *GridTri_Grad_d01r07_263.plt* 22

Table 5. Extract of *Weighted_d01r07.pl* 23

Table 6. Median_HeadGrad input and output files 25

Table 7. ID's, locations and head values at the six wells in the test problem. Units of X, Y and head are arbitrary. 32

Table 8. Results of the local gradient estimator for the six well test problem 34

Table 9. Results of the local gradient estimator for the five well test problem. 35

Table 10. ID's, locations and head values at the six wells in the test problem. Units of X, Y and head are arbitrary. 38

Appendix 1. Results of Fitting Planar Equation to 2003 Heads Using SigmaPlot Version 8.0

Nonlinear Regression

[Variables]

x = col(2)

y = col(3)

z = col(4)

reciprocal_z = 1/abs(z)

reciprocal_zsquare = 1/z^2

'Automatic Initial Parameter Estimates

F(q,r)=ape(q,r,1,0,1)

[Parameters]

y0 = F(x,z)[1] "Auto {{previous: -5007.74}}

a = F(x,z)[2] "Auto {{previous: 0.000198097}}

b = F(y,z)[2] "Auto {{previous: 0.00162289}}

[Equation]

f=y0+a*x+b*y

fit f to z

"fit f to z with weight reciprocal_z

"fit f to z with weight reciprocal_zsquare

[Constraints]

[Options]

tolerance=0.000100

stepsize=100

iterations=100

R = 0.77477928 Rsqr = 0.60028293 Adj Rsqr = 0.57067426

Standard Error of Estimate = 6.0868

	Coefficient		Std. Error	t	P
y0	-5007.7353	949.8531	-5.2721	<0.0001	
a	0.0002	0.0003	0.6225	0.5389	
b	0.0016	0.0003	6.3670	<0.0001	

Analysis of Variance:

	DF	SS	MS	F	P
Regression2	1502.2790	751.1395	20.2739	<0.0001	
Residual27	1000.3392	37.0496			
Total 29	2502.6181	86.2972			

PRESS = 1311.9035

Durbin-Watson Statistic = 1.2512

Normality Test: K-S Statistic = 0.1222 Significance Level = 0.7332

Constant Variance Test: Passed (P = 0.7888)

Power of performed test with alpha = 0.0500: 0.9997

Regression Diagnostics:

Row	Predicted	Residual	Std. Res.	Stud. Res.	Stud. Del. Res.
1	940.4779	-7.1179	-1.1694	-1.4273	-1.4566
2	924.6207	-8.1307	-1.3358	-1.3632	-1.3863
3	926.9594	-4.7094	-0.7737	-0.7875	-0.7818
4	926.2529	0.8771	0.1441	0.1468	0.1441
5	925.2531	-7.3231	-1.2031	-1.2237	-1.2356
6	921.0591	-5.3991	-0.8870	-0.9106	-0.9076
7	932.2024	4.9176	0.8079	0.8468	0.8422
8	931.2947	3.2153	0.5282	0.5516	0.5443
9	913.9456	-0.3556	-0.0584	-0.0655	-0.0643
10	904.7887	6.4913	1.0664	1.2921	1.3091
11	913.4044	8.6556	1.4220	1.7864	1.8668
12	922.6894	-7.2394	-1.1894	-1.2173	-1.2288
13	917.0599	-0.0399	-0.0066	-0.0070	-0.0068
14	920.1462	-2.1562	-0.3542	-0.3660	-0.3601
15	925.1058	-6.8058	-1.1181	-1.1383	-1.1448
16	919.7149	-5.9249	-0.9734	-1.0017	-1.0017
17	929.5036	6.3164	1.0377	1.0614	1.0640
18	930.4658	4.7142	0.7745	0.7959	0.7904
19	928.3052	10.2848	1.6897	1.7233	1.7926
20	927.5545	-0.4345	-0.0714	-0.0727	-0.0714
21	928.0958	5.4942	0.9026	0.9202	0.9175
22	928.8705	3.2695	0.5371	0.5959	0.5887
23	923.7496	-2.4996	-0.4107	-0.4875	-0.4805
24	939.5304	-1.3004	-0.2136	-0.2338	-0.2296
25	929.1186	7.1714	1.1782	1.2062	1.2169
26	930.2453	8.8047	1.4465	1.4829	1.5183
27	929.6872	6.2828	1.0322	1.0576	1.0601
28	925.2293	-6.7793	-1.1138	-1.1345	-1.1408
29	924.3491	-6.4691	-1.0628	-1.0814	-1.0850
30	924.7601	-3.8101	-0.6260	-0.6379	-0.6307

Influence Diagnostics:

Row	Cook'sDist	Leverage	DFFITS
1	0.3325	0.3287	-1.0193
2	0.0257	0.0399	-0.2824
3	0.0075	0.0348	-0.1484
4	0.0003	0.0368	0.0282

5	0.0172	0.0334	-0.2296
6	0.0149	0.0510	-0.2105
7	0.0236	0.0898	0.2645
8	0.0092	0.0828	0.1636
9	0.0004	0.2051	-0.0327
10	0.2604	0.3188	0.8955
11	0.6149	0.3663	1.4194
12	0.0235	0.0455	-0.2682
13	0.0000	0.1110	-0.0024
14	0.0030	0.0635	-0.0937
15	0.0157	0.0352	-0.2185
16	0.0197	0.0556	-0.2431
17	0.0173	0.0441	0.2285
18	0.0119	0.0532	0.1873
19	0.0398	0.0386	0.3594
20	0.0001	0.0362	-0.0138
21	0.0111	0.0379	0.1821
22	0.0273	0.1876	0.2829
23	0.0324	0.2903	-0.3073
24	0.0036	0.1647	-0.1020
25	0.0233	0.0459	0.2669
26	0.0373	0.0484	0.3426
27	0.0186	0.0475	0.2368
28	0.0161	0.0362	-0.2209
29	0.0138	0.0342	-0.2041
30	0.0052	0.0370	-0.1237

95% Confidence:

Row	Predicted	Regr. 5%	Regr. 95%	Pop. 5%	Pop. 95%
1	940.4779	933.3175	947.6384	926.0817	954.8741
2	924.6207	922.1274	927.1140	911.8851	937.3563
3	926.9594	924.6299	929.2889	914.2548	939.6639
4	926.2529	923.8577	928.6481	913.5361	938.9696
5	925.2531	922.9717	927.5345	912.5573	937.9489
6	921.0591	918.2379	923.8804	908.2553	933.8630
7	932.2024	928.4601	935.9447	919.1646	945.2402
8	931.2947	927.7000	934.8893	918.2985	944.2909
9	913.9456	908.2892	919.6019	900.2352	927.6559
10	904.7887	897.7372	911.8402	890.4463	919.1310
11	913.4044	905.8453	920.9635	898.8058	928.0030
12	922.6894	920.0265	925.3523	909.9195	935.4593
13	917.0599	912.8983	921.2215	903.8956	930.2242
14	920.1462	916.9999	923.2925	907.2668	933.0256
15	925.1058	922.7640	927.4476	912.3990	937.8126
16	919.7149	916.7693	922.6605	906.8831	932.5467
17	929.5036	926.8807	932.1265	916.7420	942.2652

18	930.4658	927.5862	933.3453	917.6490	943.2826
19	928.3052	925.8501	930.7602	915.5770	941.0333
20	927.5545	925.1785	929.9306	914.8414	940.2677
21	928.0958	925.6649	930.5267	915.3723	940.8193
22	928.8705	923.4611	934.2798	915.2602	942.4808
23	923.7496	917.0204	930.4787	909.5629	937.9362
24	939.5304	934.4612	944.5995	926.0517	953.0091
25	929.1186	926.4430	931.7941	916.3460	941.8911
26	930.2453	927.4965	932.9942	917.4572	943.0334
27	929.6872	926.9642	932.4102	916.9046	942.4698
28	925.2293	922.8546	927.6041	912.5164	937.9423
29	924.3491	922.0397	926.6585	911.6482	937.0500
30	924.7601	922.3574	927.1628	912.0419	937.4783

Appendix 2. kt3d Parameter File

Parameters for KT3D

START OF PARAMETERS:

```
aug_03_resid.dat      \file with data
1  2  0  4  0        \  columns for X, Y, Z, var, sec var
-1.0e21  1.0e21      \  trimming limits
0                    \option: 0=grid, 1=cross, 2=jackknife
xvk.dat              \file with jackknife data
1  2  0  3  0        \  columns for X,Y,Z,vr and sec var
1                    \debugging level: 0,1,2,3
kt3d.dbg             \file for debugging output
kt3d.out             \file for kriged output
224  601750.0  100.0 \nx,xmn,xsiz
307  3566550.0  100.0 \ny,ymn,ysiz
1  0.5  1.0         \nz,zmn,zsiz
1  1  1             \x,y and z block discretization
0  12              \min, max data for kriging
3                  \max per octant (0-> not used)
15000.0  15000.0  20.0 \maximum search radii
0.0  0.0  0.0      \angles for search ellipsoid
1  2.302           \0=SK,1=OK,2=non-st SK,3=exdrift
0 0 0 0 0 0 0 0 0 \drift: x,y,z,xx,yy,zz,xy,xz,zy
0                  \0, variable; 1, estimate trend
extdrift.dat        \gridded file with drift/mean
4                  \  column number in gridded file
1  13.0            \nst, nugget effect
3  45.2  0.0  0.0  0.0 \it,cc,ang1,ang2,ang3
          9000.0 9000.0 10.0 \a_hmax, a_hmin, a_vert
```

Appendix 3. Well Removal Batch File (*krig_min.bat*)

```
copy aug_03_resid.dat input.dat
c:\tools\gslib2\bin\kt3d.exe
calc_var.exe
copy kt3d.out aug_03_resid.out

copy aug_03_resid_min_aec7.dat input.dat
c:\tools\gslib2\bin\kt3d.exe
calc_var.exe
copy kt3d.out aug_03_resid_min_aec7.out

copy aug_03_resid_min_doe1.dat input.dat
c:\tools\gslib2\bin\kt3d.exe
calc_var.exe
copy kt3d.out aug_03_resid_min_doe1.out

copy aug_03_resid_min_erda9.dat input.dat
c:\tools\gslib2\bin\kt3d.exe
calc_var.exe
copy kt3d.out aug_03_resid_min_erda9.out

copy aug_03_resid_min_h2.dat input.dat
c:\tools\gslib2\bin\kt3d.exe
calc_var.exe
copy kt3d.out aug_03_resid_min_h2.out

copy aug_03_resid_min_h3.dat input.dat
c:\tools\gslib2\bin\kt3d.exe
calc_var.exe
copy kt3d.out aug_03_resid_min_h3.out

copy aug_03_resid_min_h4.dat input.dat
c:\tools\gslib2\bin\kt3d.exe
calc_var.exe
copy kt3d.out aug_03_resid_min_h4.out

copy aug_03_resid_min_h5.dat input.dat
c:\tools\gslib2\bin\kt3d.exe
calc_var.exe
copy kt3d.out aug_03_resid_min_h5.out

copy aug_03_resid_min_h6.dat input.dat
c:\tools\gslib2\bin\kt3d.exe
calc_var.exe
copy kt3d.out aug_03_resid_min_h6.out

copy aug_03_resid_min_h7.dat input.dat
c:\tools\gslib2\bin\kt3d.exe
calc_var.exe
copy kt3d.out aug_03_resid_min_h7.out

copy aug_03_resid_min_h9.dat input.dat
c:\tools\gslib2\bin\kt3d.exe
calc_var.exe
```

```
copy kt3d.out aug_03_resid_min_h9.out

copy aug_03_resid_min_h10.dat input.dat
c:\tools\gslib2\bin\kt3d.exe
calc_var.exe
copy kt3d.out aug_03_resid_min_h10.out

copy aug_03_resid_min_h11.dat input.dat
c:\tools\gslib2\bin\kt3d.exe
calc_var.exe
copy kt3d.out aug_03_resid_min_h11.out

copy aug_03_resid_min_h12.dat input.dat
c:\tools\gslib2\bin\kt3d.exe
calc_var.exe
copy kt3d.out aug_03_resid_min_h12.out

copy aug_03_resid_min_h17.dat input.dat
c:\tools\gslib2\bin\kt3d.exe
calc_var.exe
copy kt3d.out aug_03_resid_min_h17.out

copy aug_03_resid_min_p17.dat input.dat
c:\tools\gslib2\bin\kt3d.exe
calc_var.exe
copy kt3d.out aug_03_resid_min_p17.out

copy aug_03_resid_min_w12.dat input.dat
c:\tools\gslib2\bin\kt3d.exe
calc_var.exe
copy kt3d.out aug_03_resid_min_w12.out

copy aug_03_resid_min_w13.dat input.dat
c:\tools\gslib2\bin\kt3d.exe
calc_var.exe
copy kt3d.out aug_03_resid_min_w13.out

copy aug_03_resid_min_w19.dat input.dat
c:\tools\gslib2\bin\kt3d.exe
calc_var.exe
copy kt3d.out aug_03_resid_min_w19.out

copy aug_03_resid_min_w22.dat input.dat
c:\tools\gslib2\bin\kt3d.exe
calc_var.exe
copy kt3d.out aug_03_resid_min_w22.out

copy aug_03_resid_min_w25.dat input.dat
c:\tools\gslib2\bin\kt3d.exe
calc_var.exe
copy kt3d.out aug_03_resid_min_w25.out

copy aug_03_resid_min_w26.dat input.dat
c:\tools\gslib2\bin\kt3d.exe
calc_var.exe
copy kt3d.out aug_03_resid_min_w26.out
```

```
copy aug_03_resid_min_w30.dat input.dat
c:\tools\gslib2\bin\kt3d.exe
calc_var.exe
copy kt3d.out aug_03_resid_min_w30.out
```

Appendix 4: HeadGrad Program

Description of HeadGrad Program

The **HeadGrad** program compares observed water levels at wells in the Culebra to levels calculated by calibrating 100 groundwater models using the **Modflow2000** code to match the observed levels. **HeadGrad** inputs a set of acceptable triangles formed by combinations of three wells, along with the hydraulic gradients of these “well triangles.” It also inputs a **Modflow** grid and the head and flux values for each of the 100 calibration runs. **HeadGrad** organizes the grid into a set of small triangles, and using the heads, calculates a gradient for each “grid triangle” for each run. **HeadGrad** determines which grid triangles are inside each well triangle. For each well triangle, **HeadGrad** calculates a flux-weighted gradient of the average gradient over all grid triangles inside the well triangle. For each run, **HeadGrad** writes a file listing the average flux-weighted gradient for each well triangle. **HeadGrad** also writes a file listing the gradient for each well triangle calculated from the heads of the model cells nearest the well locations. Both sets of files are post-processed with the **Median_HeadGrad** program.

Execution

The **HeadGrad** program is written in Compaq Visual Fortran Version 6.6.

It was executed on a PC running Microsoft Windows 2000 with an AMD Athlon processor.

HeadGrad is controlled by files and parameters supplied on the command line. The primary execution of **HeadGrad** was run with the following command line parameters:

```
rhme_100_runs.txt rhme_100_runs.log d01r07 0
```

<i>rhme_100_runs.txt</i>	Run command file (described under Input Files), specifying the 100 Modflow models to be examined.
<i>rhme_100_runs.log</i>	Log file (described under Output Files).
<i>d01r07</i>	The run to be examined for verification.
<i>0</i>	The well triangle to be examined in detail for verification. “0” indicates that no verification files will be written.

The run command file (*rhme_100_runs.txt*) lists the 100 **Modflow** runs to be compared, as follows:

d01r02	d01r04	d01r07	d01r10	d02r02	d03r01	d03r03	d03r06
d03r07	d03r08	d03r09	d04r01	d04r02	d04r03	d04r04	d04r05
d04r06	d04r07	d04r08	d04r10	d05r03	d05r07	d06r02	d06r03
d06r04	d06r05	d06r06	d06r07	d06r10	d07r01	d07r02	d07r05
d07r06	d07r07	d07r08	d07r09	d07r10	d08r01	d08r02	d08r03
d08r04	d08r05	d08r06	d08r07	d09r02	d09r03	d09r04	d09r05
d09r06	d09r07	d09r08	d09r09	d09r10	d10r02	d10r03	d10r04
d10r06	d10r07	d10r08	d10r09	d10r10	d11r01	d11r02	d11r06
d11r07	d11r08	d11r09	d11r10	d12r01	d12r02	d12r03	d12r05
d12r06	d12r07	d12r08	d12r09	d13r01	d13r02	d13r03	d13r05
d13r06	d13r07	d13r08	d13r09	d21r01	d21r02	d21r03	d21r04
d21r05	d21r06	d21r07	d21r10	d22r02	d22r03	d22r04	d22r06
d22r07	d22r08	d22r09	d22r10				

Input and Output

Table 1 describes the input and output files for **HeadGrad**. **HeadGrad** outputs several files that are used to verify calculations or to visualize data sets. Only the verification files that are actually used for verification, as described in the Verification sections below are listed in the table.

Table 1. HeadGrad input and output files.

INPUT FILES	
<i>rhme_100_runs.txt</i>	<p>The run command file contains the following information:</p> <ul style="list-style-type: none"> Well data file name Well triangle data file name Modflow budget (flux) file name template Modflow head file name template Primary flux-weighted gradient output file name template Secondary well triangle gradient output file name template Directory for verification files Run identifier <i>dnnrnn</i> (one per line for each run) <p>The file name is formed from a template by replacing any occurrence of the character “#” with the run identifier. Lines starting with character “!” are ignored.</p>

<i>Aug_2003_wells.in</i>	The well data file contains the following information for each well: the well number, the well coordinates, and the head value.
<i>Aug_2003_shape_rhme_10.out</i>	The well triangle data file has one header row, then it contains the following information for each well triangle: the well numbers of the three wells forming the well triangle, its area, and its gradient (magnitude and flow direction).
<i>/Input/dnnrnn/dnnrnn.bud</i>	The binary Modflow budget data file for each run contains the x,y fluxes for the grid cells. The Modflow output format is described in the Modflow2000 User Guide (Harbaugh, et al., 2000).
<i>/Input/dnnrnn/steady.bin.head</i>	The binary Modflow head data file for each run contains the head values for the grid cells. The Modflow output format is described in the Modflow2000 User Guide (Harbaugh, et al., 2000).
OUTPUT FILES	
<i>rhme_100_runs.log</i>	The log file contains some basic information about the execution. It shows that each run completed successfully rather than aborting.
<i>/Output/Weighted_rhme_dnnrnn.plt</i>	The set of primary output files (one for each run) contains the well triangle gradient information. After some header lines, each file contains one line of information for each well triangle. The information includes: the input well triangle gradient, the number of grid triangles inside the well triangle, the average unweighted and flux-weighted gradients over the grid triangles inside the well triangle. The gradient is always calculated as magnitude and flow direction, but the corresponding x,y vector components is output for plotting.
<i>/Output/Nearest_rhme_dnnrnn.plt</i>	The set of secondary output files (one for each run) contains well triangle gradient information in the same format as the primary output files. The information includes the input gradient for the well triangle and the gradient calculated using the coordinates and Modflow head data from the grid points nearest the wells forming the well triangle.

Algorithm and Calculations

The basic algorithm of the **HeadGrad** program is explained below. This section describes the calculations performed by the **HeadGrad** program. The specific routine within the code that performs an action is listed in square brackets.

Read the run command file name from the command line. Read in the file name templates for all runs from the run command file.

Read the well data (coordinates, head) from the well data file [Read_Wells]. Read the well triangle data (wells forming triangle, gradient magnitude and flow direction) from the well triangle data file [Read_WellTriangles].

Set the grid sizing and coordinates as described by McKenna and Hart (2003) outlining the transmissivity field calibrations [Set_Grid]. The grid consists of 100×100m² cells that range from x = 601,700 to 624,000 (224 columns) and y = 3,566,500 to 3,597,100 (307 rows).

Determine which grid points are inside any well triangle, because grid triangles are only defined if they have at least two vertices inside any well triangle [Find_GridPoints_Within_WellTriangles]. Set up the grid triangles [Setup_GridTriangles]. Each grid triangle is an isosceles triangle, with a height and base of 2 grid cells (200 m). A picture of the grid triangle setup is provided in Figure 1.

Determine which grid point is nearest to each well forming the well triangle [Find_Nearest_GridPoint_for_Wells].

For each run listed in the run command file, do the steps below.

Read the fluxes from the **Modflow** budget data file (.bud) for this run [Read_Grid_Fluxes].

Read the head data from the **Modflow** head data file (.hed) for this run [Read_Grid_Heads].

Calculate the flux for each grid triangle by summing the absolute value of the flux across the perimeter of the 3x3 cell square that encloses the grid triangle and dividing by 2 [Calc_GridTriangle_Fluxes]. The division by 2 is necessary as the sum of the absolute fluxes includes fluxes directed both into and out of the triangle.

Calculate the gradient for each grid triangle [Calc_GridTriangle_Gradients]. The routines that perform the gradient calculation are in file *Gradient_calculations.f90*. They include modified versions of routines ludcmp, lubksb, and dpythag from *Numerical Recipes in C* by Press et al. (1992) and rewritten in FORTRAN.

For each well triangle, compute and output a flux-weighted gradient for all grid triangles inside the well triangle [Calc_Gradients_Within_WellTriangle]. First, determine which grid triangles are inside the well triangle, defined as a grid triangle having two or more vertices inside the well triangle [Point_Inside_Triangle]. For each grid triangle, multiply the calculated gradient magnitude and flow direction by the flux to get the flux-weighted values. Calculate the mean and standard deviation for the flux-weighted and unweighted gradient magnitude and flow direction over all grid triangles inside the well triangle [Calc_Gradients_Within_Single_WellTriangle].

The calculations of the unweighted mean and standard deviation are simply calculated with the standard equations for the mean and variance of a sample:

$$\bar{x} = \frac{1}{n} \sum_{i=1}^n x_i \quad (1)$$

$$s^2 = \text{var} = \frac{\sum_{i=1}^n (x_i - \bar{x})^2}{n} = \frac{n \sum_{i=1}^n x_i^2 - \left(\sum_{i=1}^n x_i \right)^2}{n^2} \quad (2)$$

where n is the number of grid triangles within well triangle and x_i is either the gradient magnitude or direction for an individual grid triangle. The weighted calculations are done using the fluxes within each grid triangle as a weight for the calculated magnitude and orientation calculated for each grid triangle. The weighted mean is:

$$\bar{x} = \frac{\sum_{i=1}^n f_i x_i}{\sum_{i=1}^n f_i} \quad (3)$$

and the weighted variance is:

$$s^2 = \text{var} = \frac{n \sum_{i=1}^n f_i x_i^2 - \left(\sum_{i=1}^n f_i x_i \right)^2}{n^2} \quad (4)$$

where f_i is the flux through grid triangle 'i' as demonstrated in Figure 1. In these calculations, direction is the angle measured in degrees clockwise from North. For the mean orientation calculation, the difference between maximum and minimum flow direction angles should be less than 180 degrees. For example, the mean of 1° and 359° is 180° instead of 0. In the analyses done in this report, the vast majority of flow direction angles are between 90 and 270 degrees.

It is noted that the **HeadGrad** program actually calculates variance but labels it standard deviation.

Note that the input and calculated flow directions range from -180..180, with 0 as north, with most values around 180 or -180. These flow directions are converted to a 0..360 coordinate system, with 0 as north, for the averaging, and converted back for output.

For each well triangle, compute and output a gradient using the head data from the grid points nearest its wells [Calc_Gradients_Nearest_WellTriangle].

Verification of the Flux-Weighted Average Gradient

The verification execution of **HeadGrad** was done before the final selection of the well triangles. It was done with the following command parameters:

```
valid_100_runs.txt valid_100_runs.log d01r07 263
```

Run command file *valid_100_runs.txt* uses the same well and **Modflow** input data, but it uses well triangle data file *Aug_2003_wells.out*.

Output file *Weighted_dnnrnn.plt* contains the flux-weighted average gradient (and the unweighted average gradient) for each well triangle for run *dnnrnn*. To verify the calculation of the flux-weighted average gradient, it must be shown that:

- the flux of a grid triangle is being calculated correctly,
- the gradient of a triangle is being calculated correctly,
- the grid triangles inside a well triangle are being correctly identified, and
- the flux-weighted average gradient over the grid triangles is being calculated correctly.

The calculations are verified by examining files written for this purpose. Most of the calculations are simple, but involve a large amount of data. For this reason, most of the verification files contain data for a single well triangle (263) and a single run (d01r07). Well triangle 263 is a very narrow triangle with a small number of grid triangles (57). It corresponds to well triangle 261 defined in the well triangle file *Aug_2003_shape_rhme_10.out*.

The verification files that are included in this text are modified to focus on the values needed to verify the calculation. For example, columns of data used only for plotting might be deleted. Descriptive titles might be modified or added. The data are never modified.

Verifying the flux of a grid triangle calculation

The flux for each grid triangle is calculated by summing the absolute value of the flux across the perimeter of the smallest rectangle of grid cells that encloses the grid triangle (in this case, a 3×3 cell square) and dividing the sum by 2 to account for having calculated by inflows and outflows. Figure 1 shows a graphical representation of the flux calculation for grid triangle 7279 (the second triangle on the verification file). File *GridTri_Flux_d01r07_263.out* lists the X, Y fluxes for the grid cells that make up the 57 grid triangles inside well triangle 263, and the calculated grid triangle flux. The flux calculation was verified by repeating the calculation in **Microsoft Excel** on the first two grid triangles. The result is listed in Table 2. The table only lists the perimeter fluxes that should be summed; the interior fluxes and fluxes outside the box are excluded. The SUM line lists the **Excel**-calculated sum of the listed flux absolute values for each column. The flux calculated in **Excel** is the sum of the five column sums divided by 2 and is listed in the SUM “Flux” column. The flux on the grid triangle title line is the **HeadGrad** calculated flux (from the verification file). In each case, the flux value calculated in **Excel** matches the value calculated by **HeadGrad**, verifying that the flux calculation is correct.

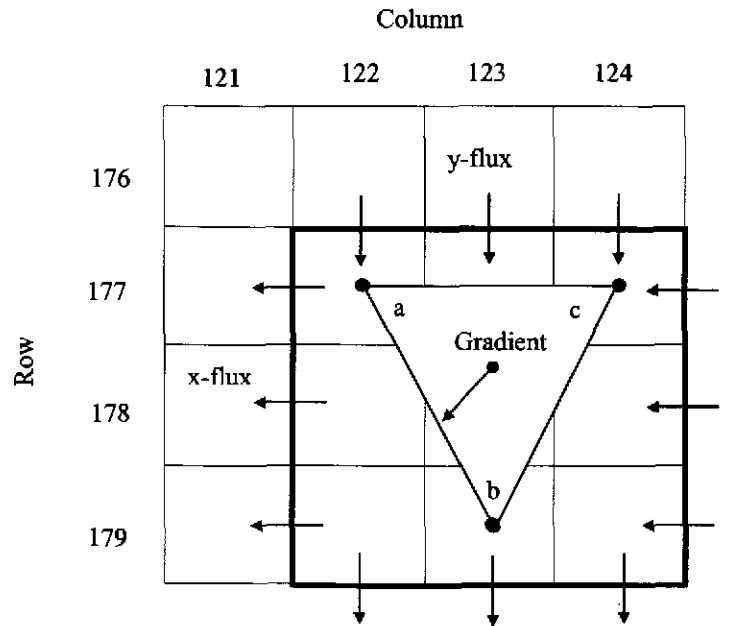


Figure 1. Visual diagram of the grid triangle flux

Table 2. Extract of *GridTri_Flux_d01r07_263.out*, processed by Excel

		X flux to be summed			Y flux to be summed			Flux
Grid Triangle 7278 (179,121); (177,122); (179,123)								6.32841E-07
Row	Col 120		Col 123		Col 121	Col 122	Col 123	
176					205.541E-9	185.912E-9	154.188E-9	
177	-78.964E-9		-25.874E-9					
178	-79.947E-9		-30.034E-9					
179	-77.281E-9		-31.292E-9		148.937E-9	133.368E-9	114.345E-9	
SUM	236.192E-9		87.200E-9		354.478E-9	319.279E-9	268.533E-9	6.32841E-07
Grid Triangle 7279 (177,124); (177,122); (179,123)								5.21549E-07
Row	Col 121		Col 124		Col 122	Col 123	Col 124	
176					185.912E-9	154.188E-9	118.364E-9	
177	-58.729E-9		-20.102E-9					
178	-60.882E-9		-19.134E-9					
179	-59.977E-9		-23.849E-9		133.368E-9	114.345E-9	94.249E-9	
SUM	179.587E-9		63.085E-9		319.279E-9	268.533E-9	212.613E-9	5.21549E-07

Verifying the gradient calculation

The gradients for the grid triangles are calculated with the algorithm that was used to calculate the gradients for the well triangles that are input in the well triangle data file. To verify the

HeadGrad implementation of this algorithm, the gradients for the well triangles were calculated in **HeadGrad** and compared to the input gradients. The comparison is found in file *WellTri_Grad.out*. The magnitudes and flow directions on the well triangle data file have six significant digits, so the verification file lists exactly six digits. Table 3 lists the verification file output for well triangles that differed in either the magnitude or flow direction. (The output that differs is flagged with “***” in the validation file.) The input and calculated magnitudes match exactly for all well triangles. In 8 of the 1660 well triangles, the input and calculated flow directions differ by one in the 6th digit. In these eight cases, the difference is always 5E-4 or 5E-5, indicating that when roundoff is considered, the difference is actually in the 7th or later significant digit. This verifies that the gradient calculation is correct.

Table 3. Extract of *WellTri_Grad.out*

Tri#	Wells			input_magn	calc_magn	dif_magn	input_fdir	calc_fdir	dif_fdir
201	1	19	24	6.62171E-04	6.62171E-04	-3.11E-10	8.53443E+01	8.53442E+01	5.34E-05
275	2	6	26	5.84913E-03	5.84913E-03	-3.88E-09	1.49171E+02	1.49172E+02	-5.02E-04
457	4	5	14	1.79228E-02	1.79228E-02	5.84E-09	5.92217E+01	5.92216E+01	5.25E-05
519	4	12	19	7.99311E-03	7.99311E-03	5.90E-10	-1.59967E+02	-1.59966E+02	-5.01E-04
628	5	14	22	3.04847E-03	3.04847E-03	-3.42E-09	5.89846E+01	5.89845E+01	5.22E-05
650	6	7	22	3.23688E-03	3.23688E-03	1.20E-09	-1.75803E+02	-1.75802E+02	-5.02E-04
731	6	13	23	3.30002E-03	3.30002E-03	-2.60E-09	2.88745E+01	2.88744E+01	5.05E-05
1517	14	15	22	2.06598E-03	2.06598E-03	-4.48E-09	7.19122E+01	7.19121E+01	5.00E-05
	MAX Diff					4.80E-08			5.02E-04

Verifying whether a grid triangle is inside a well triangle

By definition, a grid triangle is inside a well triangle if two or more of the grid triangle vertices are inside the well triangle. To verify the selection of the appropriate grid triangles that are inside the well triangles, **HeadGrad** was executed using a single-run command file (*run_d01r07.txt*) to write a validation file describing the 222 grid triangles that are inside well triangle 244. (Well triangle 244 corresponds to well triangle 246 defined in the well triangle file *Aug_2003_shape_rhme_10.out*.) Note that well triangle 263 used above to verify fluxes is not used here as it is difficult to determine whether or not grid triangles fit within the long and narrow well triangle 263. File **GridTriangles_244.plt** is input into the **Tecplot** plotting program to create the plot of the well triangle 244 and the 222 grid triangles identified by **HeadGrad** as being inside the well triangle. The resulting plot is shown in Figure 2. By examining this figure, it can be seen that all grid triangles drawn have at least two vertices inside the well triangle. Further, none of the missing grid triangles along the perimeter of the well triangle would have two vertices in the well triangle. This verifies that **HeadGrad** is correctly identifying the grid triangles that are inside the well triangle.

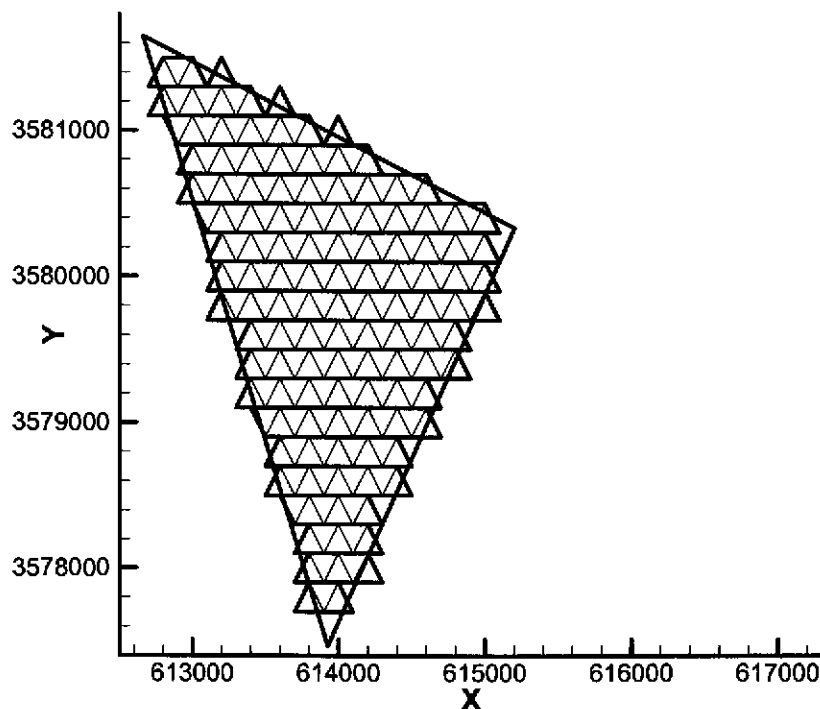


Figure 2. Grid triangles inside well triangle 244 (*GridTriangles_244.plt*)

Verifying the flux-weighted average gradient calculation

The calculation of the unweighted and the flux-weighted average gradient is verified by examining file *GridTri_Grad_d01r07_263.plt*, which contains the values for run d01r07 for the 57 grid triangles inside well triangle 263. This file is contained within the */Monitoring_04/Heterogeneity/HeadGrad_a.zip* file. Table 4 is an extract of this file. The flux-weighted magnitude is the flux multiplied by the magnitude; the flux-weighted flow direction is the flux multiplied by the flow direction. The weighted values have been verified with **Microsoft Excel**. The last row in the table, the “average” row lists the total number of grid triangles used in the calculations, the average flux, the unweighted average gradient magnitude and flow direction, and the flux-weighted average magnitude and flow direction. Each entry in the rows of the “Flux-weighted Magnitude” column (Table 4) is the product of the “Flux” and “Magnitude” entries in the same row. The value in the final row is the flux weighted average magnitude. This value is, following Equation 3, the sum of the entries in rows of the Flux-weighted Magnitude column divided by the sum of the entries in the “Flux” column. The sum of the entries in the “Flux” column is not shown in Table 4. The bottom row of the “Flux-weighted Flow dir” column is the flux-weighted orientation and it is calculated the same way as the flux weighted magnitude using the sum of the “Flow dir” column. The verification file was input into **Microsoft Excel**, and the flux weighted values and the averages was recalculated and found to be identical to the values in the file. This verifies that the flux-weighted average gradient is being calculated correctly.

Table 4. Extract of *GridTri_Grad_d01r07_263.out*

Grid Triangle		Flux	Magnitude	Flow dir (0..360)	Flux-weighted Magnitude	Flux-weighted Flow dir (0..360)
7278	1	6.328413E-07	1.889983E-03	200.877	1.196059E-09	1.271233E-04
7279	2	5.215488E-07	1.643617E-03	192.383	8.572265E-10	1.003373E-04
7280	3	4.156517E-07	1.622406E-03	195.738	6.743559E-10	8.135889E-05
7614	4	8.862974E-07	2.873802E-03	204.145	2.547044E-09	1.809335E-04
7615	5	8.273217E-07	2.833331E-03	203.472	2.344076E-09	1.683372E-04
...						
10009	56	3.039102E-05	9.856566E-04	107.161	2.995511E-08	3.256745E-03
10010	57	3.520128E-05	7.340560E-04	103.892	2.583971E-08	3.657125E-03
Average	57	1.147523E-05	1.491925E-03	179.630	5.118185E-04	144.502

The unweighted and flux-weighted magnitude and flow direction appear in the output file *Weighted_d01r07.plt* for well triangle 263. This file is contained within the */Monitoring_04/Heterogeneity/HeadGrad_a.zip* file. An extract of this file is shown in Table 5. The unweighted and flux-weighted magnitude and flow direction exactly match the averages output in file *GridTri_Grad_d01r07_263.out*. Note that the flow direction is 0° to 360° in Table 4, and -180° to 180° in Table 5. Thus, if the average flow direction was greater than 180°, it would be converted to -180°.

Table 5. Extract of *Weighted_d01r07.plt*

WellTri	nInsTri	avgMagn,_Fdir180	avgWtMagn,_Fdir180	avgFlux		
263	57	1.491925E-03	179.630	5.118185E-04	144.502	1.147523E-05

Verification of Well Triangle Gradient Using Nearest Model Cells

Output file *Nearest_dnnrnn.plt* contains the well gradient calculated using the coordinates and the head values of the grid cells nearest the three wells forming each well triangle for run *dnnrnn*. To verify the calculation of this well gradient, it must be shown that:

- **HeadGrad** selects the nearest grid cell to each well, and
- the triangle gradient is being calculated correctly.

To verify that **HeadGrad** is selecting the nearest grid cell for each well, file *Nearest_XY.plt* is examined. This file lists the (x,y) position of each well and its nearest grid cell and the difference between the two. Because each grid cell is $10 \times 10 \text{m}^2$ square, the difference between the well position and its nearest grid cell must be less than ± 50 in both the x and y . This is true for all 30 wells. The gradient calculation was verified above. This verifies that the well gradients in output file *Nearest_dnnrnn.plt* are correct.

Reference:

Harbaugh, A. W., E.R. Banta, M.C. Hill and M.G. McDonald, 2000, MODFLOW-2000, the U.S. Geological Survey Modular Ground-Water Model – User Guide to Modularization Concepts and the Ground-Water Flow Process, U.S. Geological Survey.

Appendix 5. Median_HeadGrad Program

Description of Median_HeadGrad Program

The **Median_HeadGrad** program reads data from the files written by the **HeadGrad** program, and yields statistics, including the mean, median, and quantiles for the flux-weighted averages for each well triangle over all runs. It also calculates statistics for the unweighted averages. Statistics are also calculated for the well gradients calculated using the **Modflow** data at the grid cells nearest the well.

Execution

The **Median_HeadGrad** program is written in **Compaq Visual Fortran** (Version 6.6).

It was executed on a PC running Microsoft Windows 2000 with an AMD Athlon processor.

Median_HeadGrad is controlled by files and parameters supplied on the command line. The primary execution of **Median_HeadGrad** was run with the following command line parameters:

```
rhme_100_runs.txt Median_Unwt_rhme.plt Median_Wt_rhme.plt 5 0
```

Median_HeadGrad was executed a second time with the following command line:

```
rhme_100_runs.txt Median_Near_rhme.plt NEAR 5 0
```

<i>rhme_100_runs.txt</i>	Run command file (described under Input Files), specifying the 100 output files to be examined.
<i>Median_Unwt_rhme.plt</i>	The output file with statistics for the unweighted averages.
<i>Median_Near_rhme.plt</i>	The output file with statistics for the well gradients calculated using Modflow data from the nearest grid points.
<i>Median_Wt_rhme.plt</i>	The output file with statistics for the flux-weighted averages.
NEAR	This parameter indicates that Median_HeadGrad should read the data from the Nearest_rhme_dnnrnn.plt files output by HeadGrad . No file will be written with statistics for the flux-weighted averages.
5	Output quantiles at 5% and 95%.
0	The well triangle to be examined in detail for verification.
	“0” indicates that no verification file will be written.

Input and Output

Table 6 describes the input and output files for **Median_HeadGrad**.

Table 6. Median_HeadGrad input and output files

INPUT FILES	
<i>valid_100_runs.txt</i>	The run command file is the same file used for the HeadGrad execution. Only the HeadGrad output file name templates and the run identifiers are used; the HeadGrad input file names are ignored.
<i>/Output/Weighted_rhme_dnrnn.plt</i>	These HeadGrad output files (one for each run) contain the unweighted and flux-weighted average gradient for each well triangle. These files are input for the primary execution of Median_HeadGrad .
<i>/Output/Nearest_rhme_dnrnn.plt</i>	These HeadGrad output files (one for each run) contain the well triangle gradient calculated using the Modflow data from the grid points nearest the wells forming the well triangle. These files are input for the second execution of Median_HeadGrad .
OUTPUT FILES (in /Output)	
<i>Median_Unwt_rhme.plt</i>	This output file contains the statistics for the unweighted average well triangle gradient. The statistics are the mean, median, 5% quantile, and 95% quantile of the magnitude and flow direction over all runs for each acceptable well triangle.
<i>Median_Wt_rhme.plt</i>	This output file contains the statistics for the flux-weighted average well triangle gradient.
<i>Median_Near_rhme.plt</i>	This output file, generated by the second execution of Median_HeadGrad , contains the statistics for the well triangle gradient calculated using the Modflow data from the nearest grid points.

Algorithm and Calculations

The **Median_HeadGrad** program calculates statistics for magnitude and flow direction over 100 runs for each well triangle. The statistics are mean, median, 5% quantile, and 95% quantile. The mean calculation is self-evident. The quantile statistics are calculated by sorting the 100 values, then selecting value 51 for the median, value 5 for the 5% quantile, and value 96 for the 95% quantile.

Note that the input flow directions range from -180..180, with 0 as north, with most values around 180 or -180. These flow directions are converted to a 0..360 coordinate

system, with 0 as north, for all statistic calculations and are output in the 0..360 coordinate system.

Verification of Median_HeadGrad

Median_HeadGrad is verified using the verification data from **HeadGrad**. The verification execution of **Median_HeadGrad** was run with the following command line parameters:

```
valid_100_runs.txt Median_Unweighted.plt Median_Weighted.plt 5 263
```

The calculations performed by **Median_HeadGrad** are simple, but they involve a large amount of data spread over 100 data files. For this reason, **Median_HeadGrad** writes a verification file, *Median_263.out*, with the input magnitude and flow direction (0..360) for well triangle 263 over all 100 runs, and the calculated statistics. The verification file contains the 100 values for the unweighted averages, followed by the values for the flux-weighted averages. The verification file was input to **Microsoft Excel**. The unweighted average gradient magnitudes were sorted, and the appropriate quantile data were selected from the sorted data, and compared to the calculated statistics on the verification file. The mean was calculated and compared to the calculated mean. This process was repeated for the unweighted average gradient flow direction and the flux-weighted average gradient magnitude and flow direction. In each case, the **Excel**-calculated statistics matched the **Median_HeadGrad** calculations, verifying that the statistics are being calculated correctly.

It was also verified that the correct magnitudes and flow directions from the appropriate input file were written to the verification file (for run *d01r07* only). (If the input flow direction is negative, the verification file lists the flow direction as 360 plus the input flow direction.) The calculated statistics for well triangle 263 are written correctly to output files *Median_Unweighted.plt* and *Median_Weighted.plt*.

Appendix 6. Test of the RHME program

The program **RHME** is used to determine the amount of error in the actual estimates of the orientation and magnitude of the gradient from as obtained from a local gradient estimator when there is error in the head measurements. Results can be obtained for any ratio of RHME desired. This program is contained in the file *RHME.cpp* and makes use of the supporting source codes *triangle.cpp* and *nrutil.cpp* and also uses the header files *triangle.h* and *nrutil.h*.

This program is tested by assigning the RHME value to be zero and generating 5000 realizations of the measured heads. To accomplish this test, the global variable `ERR_TO_DROP` on line 30 of the *RHME.cpp* is set to equal 0.000. The test criteria are:

- 1) The output file must contain the requested number of lines, one for each sampling realization. For this test problem, the output file must contain 5000 lines.
- 2) The estimated magnitude of the gradient must equal that of the true magnitude. For this test problem, the true magnitude of the gradient is 0.001.
- 3) The estimated orientation of the gradient must equal that of the true orientation. For this test problem, the true orientation of the gradient is 180 degrees (due south).

The output file name is specified on line 32 of *RHME.cpp* as *mserr_test.out* for this test problem. The code is compiled and run from a DOS window by typing *debug\rhme.exe* at the command prompt.

The results of the test problem are contained in the output file. There are five columns in the file: the error ratio, the actual gradient, the estimated gradient, the actual orientation and the estimated orientation. All three of the test criteria are met: there are 5000 lines in the output file, each line correctly identifies 0.001 as the true gradient and each line correctly identifies 180 as the true orientation.

Appendix 7. Testing the main code for evaluating the effects of estimator shape and gradient orientation.

The code **main** is used to estimate the magnitude and orientation of the hydraulic gradient from a series of three head measurements. This code is used with synthetically generated data to test the ability of three wells to identify the true gradient in the presence of measurement error. This code reads in an input file that has the coordinates of the three wells on the first line in $X1, Y1, X2, Y2, X3, Y3$ order and then has a series of head measurements in $h1, h2, h3$ order on each line. Each set of head measurements is designed to produce a different orientation in the true gradient. In the calculations done for this report, these orientations are for roughly every 15 degrees around the 360° circle (24 gradient orientations).

The **main** code adds a random number drawn from a zero mean Gaussian distribution with the appropriate variance for the specified measurement error to each of the head measurements for a different orientation and does this “NUM_MSMTS” times for each orientation of the gradient. Here, NUM_MSMTS is set to 2000. These calculations can be done for any level of RHME as defined with the ERR_TO_DROP variable in the code.

The output of the code is a text file with five columns:

- 1) The value of RHME (will be constant for all lines in the output file)
- 2) The true value of the gradient magnitude calculated from the input values with no measurement error.
- 3) The estimated value of the gradient magnitude calculated from the input values with simulated measurement error.
- 4) The true value of the gradient orientation calculated from the input values with no measurement error.
- 5) The estimated value of the gradient orientation calculated from the input values with simulated measurement error.

Five test criteria are set for the **main** code:

- 1) The code must be able to read in a previously defined text formatted input file.
- 2) The code must produce the correct number of output records as defined by the variable NUM_MSMTS for each orientation of the gradient.
- 3) The code must produce results for the correct number of gradient orientations in the input file.
- 4) For a specified value of ERR_TO_DROP equal to zero, the code must produce the correct magnitude of the gradient for all output.
- 5) For a specified value of ERR_TO_DROP equal to zero, the code must produce the correct magnitude of the gradient for all output.

All input and output files for the test of the main code, as well as the source code files are in the *Monitoring_04\Test_Problems\shape_test* subdirectory. The test problem is run using the input file for the 41-degree triangle, *41_cases.txt*. This input file is reproduced in Figure 3. The top line of this files gives the X, Y coordinates for each of the wells used to calculate the gradient.

The next 24 lines specify the head measurements to create 24 different orientations of the gradient at roughly 15-degree intervals.

```
0.00 0.00 200.00      0.00 100.00      87.30
10.0707      10.0707      9.92929
10.0941      10.0339      9.96613
10.0996      10.0094      9.99059
10.0999      9.99607      10.0039
10.099      9.98591      10.0141
10.0969      9.97513      10.0249
10.0949      9.96835      10.0316
10.0911      9.95885      10.0412
10.0861      9.9491       10.0509
10.075      9.93387      10.0661
10.0509      9.91393      10.0861
9.99372      9.9002       10.0998
9.92929      9.92929      10.0707
9.90591      9.96613      10.0339
9.90044      9.99059      10.0094
9.90005      10.0031      9.99686
9.90089      10.0133      9.98669
9.90241      10.0218      9.97819
9.90489      10.0309      9.9691
9.90854      10.0404      9.95957
9.91393      10.0509      9.9491
9.92447      10.0655      9.93446
9.94708      10.0849      9.91515
9.99686      10.1 9.90005
```

Figure 3. Input file for the main test problem.

The test problem is run by typing *debug\main* at the DOS command prompt in the *Monitoring_04\Test_Problems\shape_test* subdirectory. The output file is *mserr41_000.out*. The values of NUM_MSMSTS and ERR_TO_DROP are set to 2000 and 0.000 respectively.

Examination of the output file shows that the code did produce 2000 output lines for each of the 24 different orientations. For all output lines, the estimated magnitude and orientation match the true magnitude and orientation exactly. The test run met all the criteria of the test problem and therefore the code is satisfactory for use in these calculations.

Appendix 8. Test Problem for Well Removal Gradient Estimation

The software to determine the local gradient given three sets of wells consists of three C++ source codes and two header (*.h) files. The two header files *nrutil.h* and *triangle.h*, as well as the source files *triangle.cpp* and *nrutil.c*, remain fixed for all applications in this work. The final file, *estimate_Remove.cpp*, is similar to other files used in this analysis package but has been edited and recompiled specifically for this well removal application. All of these source and header files are compiled into a single executable using the Microsoft Visual C++ (version 6.0) compiler on a 1.7GHz Pentium 4 PC running the Microsoft Windows 2000 operating system. The final compiled executable, **estimate_Remove**, is referred to as the “removal program” in the discussion below.

A simple test problem with six wells is developed to test the ability of the removal program to determine the magnitude and orientation of the hydraulic gradient from a limited number of wells. This test problem is run from the *\Monitoring_04\Test_Problems\Removal_test* subdirectory contained on the CD-ROM accompanying this report. The problem is run twice, once with six wells and once with five wells. The five well case is created by removing one of the original six wells.

Four criteria are selected to evaluate the removal program to correctly determine that local gradients have been established. These criteria must be met for both the six and five well cases:

- 1) The program must return the correct number of local gradient estimates from the input number of wells. This number is calculated as:

$$mCn = \frac{m!}{n!(m-n)!} \quad (5)$$

where *m* equals the total number of wells in the monitoring network, six for this example and *n* equals the number of wells in the estimator, three.

- 2) The calculated areas of each triangle must match those calculated using the X and Y coordinates of each point defining the triangle in the matrix equation for the area of a triangle:

$$Area = \pm 0.5 \begin{vmatrix} x_1 & y_1 & 1 \\ x_2 & y_2 & 1 \\ x_3 & y_3 & 1 \end{vmatrix} = \pm 0.5(x_1y_2 + y_1x_3 + y_3x_2 - y_2x_3 - y_1x_2 - x_1y_3) \quad (6)$$

- 3) Given that the test problem represents a homogeneous aquifer and the head measurements are error-free, the removal program must return the exact estimates of the magnitude of the underlying true hydraulic gradient

- 4) Given that the test problem represents a homogeneous aquifer and the head measurements are error-free, the removal program must return the exact estimates of the orientation of the hydraulic gradient.

The test problem is created by defining a regional planar gradient with the flow direction to the SE, or a direction of 135 degrees clockwise from north and a magnitude of 0.021213. Heads for any point in X, Y space can be determined by:

$$H(x, y) = Ax + By + C \quad (7)$$

Where coefficient values of $A = -0.015$, $B = 0.015$ and $C = 1000$ create the specified orientation and magnitude of the gradient. These coefficients are related to the orientation and the magnitude of the gradient by:

$$magnitude = \sqrt{A^2 + B^2} \quad (8)$$

$$orientation = \arctan\left(\frac{B}{A}\right) \quad (9)$$

The C coefficient can be thought of as an intercept on the head axis and the head across the middle of the domain perpendicular to the flow direction is equal to the value of C . A contour plot of the head field is given in Figure 4.

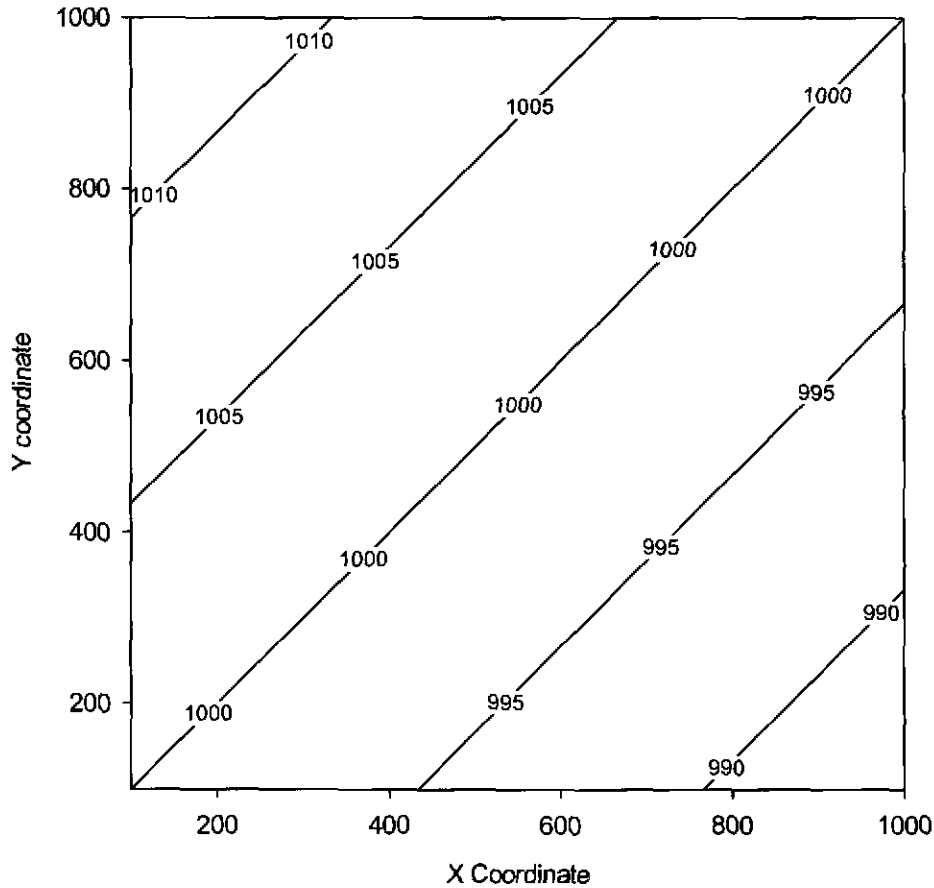


Figure 4. Contour map of the regional head field used in this test problem. The units of head are arbitrary.

Six well locations are chosen within the domain (Figure 5) and the head is calculated at each location using Equation 7 with the correct coefficients. These six locations serve as the head monitoring locations. The well locations along with the head values and the well ID's are shown in Table 7. Table 7 contains all of the information needed as input to the estimator. This information is copied into the text file *test6wells.in* for use in this test problem.

Table 7. ID's, locations and head values at the six wells in the test problem. Units of X, Y and head are arbitrary.

Well ID	X-Coordinate	Y-Coordinate	Head
1	190	90	998.50
2	790	110	989.80
3	200	490	1004.35
4	800	510	995.65
5	210	890	1010.20
6	810	910	1001.50

The local gradient estimations are calculated by typing `debug\estimate.exe` at the DOS command prompt from within the `\Monitoring_04\Test_Problems\Remove_test` subdirectory.

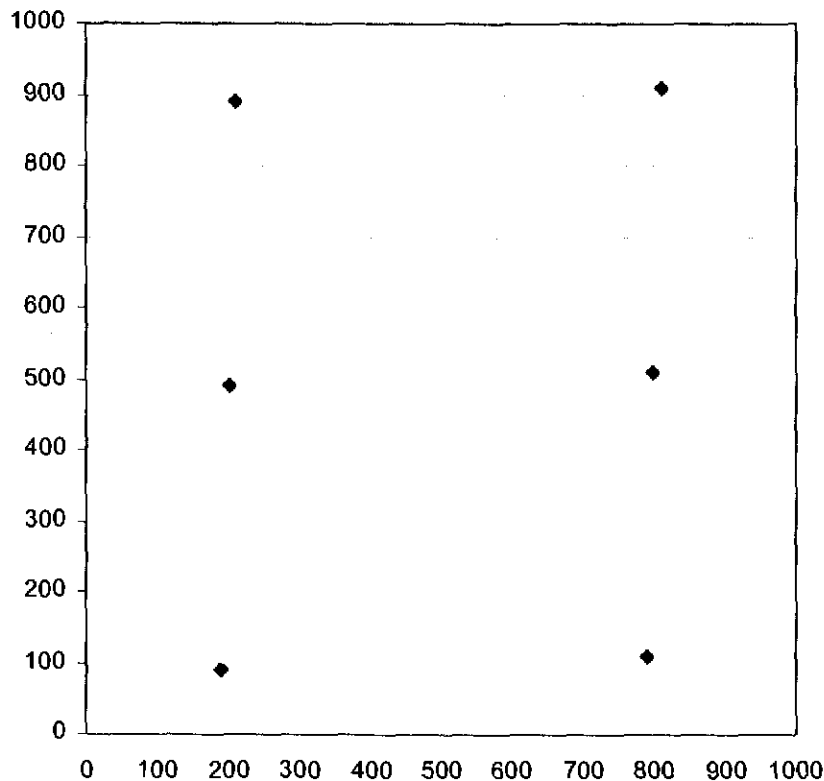


Figure 5. Locations of the six wells used in the test problem. The well located at (200,490) is removed for the five well test problem.

The five well case test problem is created by removing well number 3 at location (200,490) from the six well configuration. The five well case input file is: `test5wells.in`. The two test cases are run in a single call to the model. This call is “`debug\estimate_Remove`” from a DOS command prompt in the `\Monitoring_04\Test_Problems\Remove_test\` subdirectory.

Results of the calculations made by the removal program are given in Tables 8 and 9. The information in these two tables comes directly from the output files of the removal program: `test6wells.out` and `test5wells.out`. Each of the criteria used to determine the accuracy of this program are evaluated using the results in Table 8. The results of this evaluation are also contained in the `remove_test.xls` Excel spreadsheet file in the `\Monitoring_04\Test_Problems\Remove_test` subdirectory.

- 1) For the six well configuration, the removal program identified a total of 20 triangles. Solution of (5) using $m=6$ and $n=3$ results in 20 triangles and therefore this criterion is met exactly. For the five well configuration, the removal program identified a total of 10

triangles. Solution of (5) using $m=5$ and $n=3$ results in 10 triangles and therefore this criterion is met exactly.

- 2) The calculated areas of each triangle are shown in the 4th column from the left in Tables 8 and 9. The areas of the triangles were also calculated using (6) and the X and Y coordinates of the triangles as identified by the removal program. These calculations are documented in *remove_test.xls* spreadsheet. The areas calculated by the removal program and (6) are an identical match. By design, in the six well test, the combinations of wells 2, 4 and 6 and 1, 3 and 5 form two different straight lines and therefore the area enclosed by the “triangle” made up from either set of these three points is zero. The removal program correctly identified both of these zero area triangles.
- 3) The magnitude of the regional gradient, 0.212132, is correctly identified for every triangle in both cases by the removal program with the exception of the two zero area triangles. These two sets of three points do not make a valid triangle for estimation and these results are disregarded.
- 4) The orientation of the regional gradient, 135 degrees clockwise from the north, is correctly identified for every triangle in both cases by the removal program with the exception of the two zero area triangles. These two sets of three points do not make a valid triangle for estimation and are disregarded.

Table 8. Results of the local gradient estimator for the six well test problem.

Well ID 1	Well ID 2	Well ID 3	Area	Magnitude	Orientation
1	2	3	119900	0.0212132	135
1	2	4	119900	0.0212132	135
1	2	5	239800	0.0212132	135
1	2	6	239800	0.0212132	135
1	3	4	119900	0.0212132	135
1	3	5	0	5.31255	-88.7256
1	3	6	119900	0.0212132	135
1	4	5	239800	0.0212132	135
1	4	6	119900	0.0212132	135
1	5	6	239800	0.0212132	135
2	3	4	119900	0.0212132	135
2	3	5	119900	0.0212132	135
2	3	6	239800	0.0212132	135
2	4	5	119900	0.0212132	135
2	4	6	0	1.25536	-89.2352
2	5	6	239800	0.0212132	135
3	4	5	119900	0.0212132	135
3	4	6	119900	0.0212132	135
3	5	6	119900	0.0212132	135
4	5	6	119900	0.0212132	135

Table 9. Results of the local gradient estimator for the five well test problem.

Well ID 1	Well ID 2	Well ID 3	Area	Magnitude	Orientation
1	2	4	119900	0.0212132	135
1	2	5	239800	0.0212132	135
1	2	6	239800	0.0212132	135
1	4	5	239800	0.0212132	135
1	4	6	119900	0.0212132	135
1	5	6	239800	0.0212132	135
2	4	5	119900	0.0212132	135
2	4	6	0	1.25536	-89.2352
2	5	6	239800	0.0212132	135
4	5	6	119900	0.0212132	135

In summary, the removal program produces results on the test problem that are correct for all four of test criteria identified prior to testing.

Appendix 9. Test Problem for Well Addition Gradient Estimation

The software to determine the local gradient given three sets of wells consists of three C++ source codes and two header (*.h) files. The two header files *nrutil.h* and *triangle.h*, as well as the source files *triangle.cpp* and *nrutil.c* remain fixed for all applications in this work. The final file, *locat.cpp*, is similar to other files used in this analysis package but has been edited and recompiled specifically for this well addition application. All of these source and header files are compiled into a single executable using the Microsoft Visual C++ (version 6.0) compiler on a 1.7GHz Pentium 4 PC running the Microsoft Windows 2000 operating system. The final compiled executable, *locat*, is referred to as the “addition program” in the discussion below.

A simple test problem with six well measurements and then an additional 100 estimated or “average” heads on a 10 × 10 grid is developed to test the ability of the addition program to determine the magnitude and orientation of the hydraulic gradient from a limited number of wells. This test problem is run the *Monitoring_04\Test_Problems\add_test* subdirectory contained on the CD-ROM accompanying this report. The problem is run twice, once with six wells and once with five wells.

Four criteria are selected to evaluate the addition program to correctly determine the total number three-point estimators created by the addition of a single well:

- 1) The program must return the correct number of local gradient estimates from the input number of wells. This number is calculated as:

$$mCn = \frac{m!}{n!(m-n)!} \quad (10)$$

where *m* equals the total number of wells in the monitoring network, six for this example and *n* equals the number of head measurement locations in the estimator, three.

- 2) The addition program must determine the total number of estimators created for each of the 100 different wells on the 10 × 10 grid. This criterion is met if the output file has 100 lines.
- 3) The program must be able to correctly interpret a -999 as a missing data value. For any grid location with a -999 for the average head estimate, the program must return -999 for the number of estimators created by add a well at that location
- 4) The output file must contain the correct coordinates for the locations of the added well.

The test problem is created by defining a regional planar gradient with the flow direction to the SE, or a direction of 135 degrees clockwise from north and a magnitude of 0.021213. Heads for any point X,Y space can be determined by:

$$H(x, y) = Ax + By + C \quad (11)$$

Where coefficient values of $A = -0.015$, $B = 0.015$ and $C = 1000$ create the specified orientation and magnitude of the gradient. These coefficients are related to the orientation and the magnitude of the gradient by:

$$\text{magnitude} = \sqrt{A^2 + B^2} \tag{12}$$

$$\text{orientation} = \arctan\left(\frac{B}{A}\right) \tag{13}$$

The C coefficient can be thought of as an intercept on the head axis and the head across the middle of the domain perpendicular to the flow direction is equal to the value of C . A contour plot of the head field is given in Figure 6.

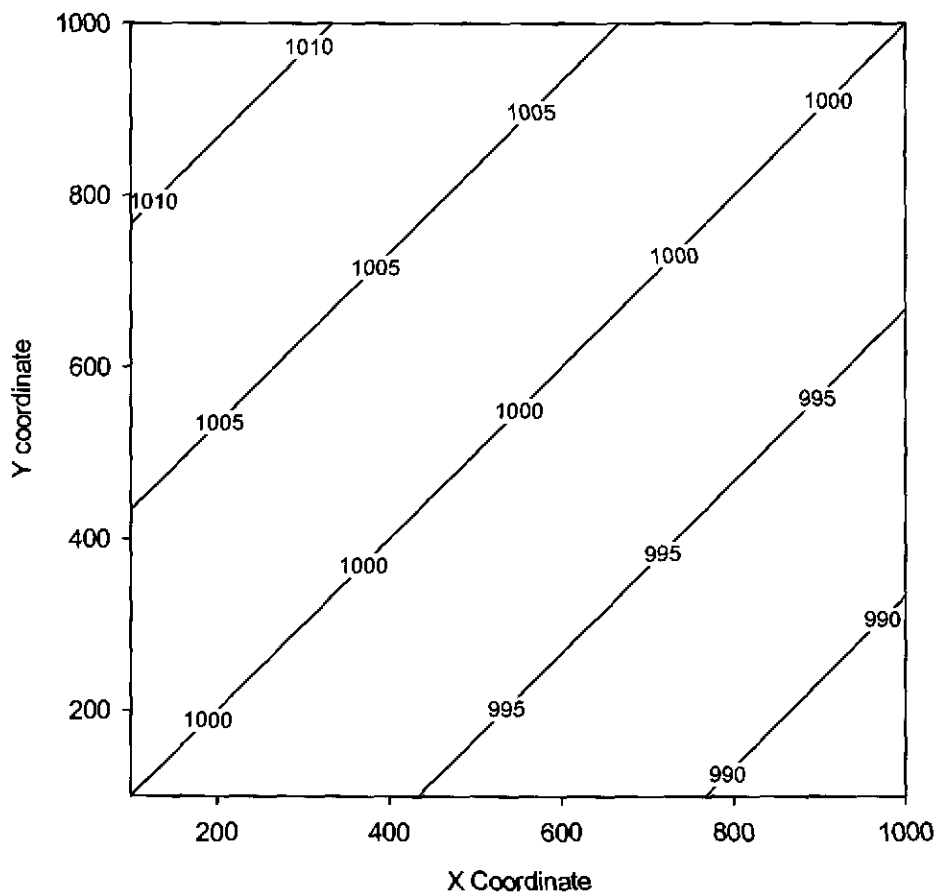


Figure 6. Contour map of the regional head field used in this test problem. The units of head are arbitrary.

Six well locations are chosen within the domain (Figure 7) and the head is calculated at each location using Equation 11 with the correct coefficients. These six locations serve as the head monitoring locations and are given in the *add_test.xls* file. The well locations along with the head values and the well ID's are shown in Table 10. The additional input file for this test problem contains values of average head as calculated on a grid. These values are also calculated using (11) and are contained in the *add_test.xls* file. The information in Table 10 is copied into the text file *test6wells.in* for use in this test problem. The heads on the grid points are copied into the file: *head_grid_data.txt*. A five line header, corresponding to the header used by the **Surfer** (version 8.0) software is added to the top of this text file. The 5-line header contains a keyword (DSAA), the number of X and Y cells in the grid, the minimum and maximum X coordinates, the minimum and maximum Y coordinates, a min and max head value. The keyword and the range of head values are not used by the addition program.

Table 10. ID's, locations and head values at the six wells in the test problem. Units of X, Y and head are arbitrary.

Well ID	X-Coordinate	Y-Coordinate	Head
1	190	90	998.50
2	790	110	989.80
3	200	490	1004.35
4	800	510	995.65
5	210	890	1010.20
6	810	910	1001.50

The local gradient estimations are calculated by typing *debug\locat.exe* at the DOS command prompt from within the *\Monitoring_04\Test_Problems\add_test* subdirectory. The program prompts the user for the name of the triangle output file, *triangles.out*, was used in the test problem and the name of the file containing the heads on the grid, *head_grid_data.txt*. An additional output file containing one line with information on the regional gradient is also written. This file is *test6wells.out*. The information in this output file is not germane to the problem and is not used in any further analyses.

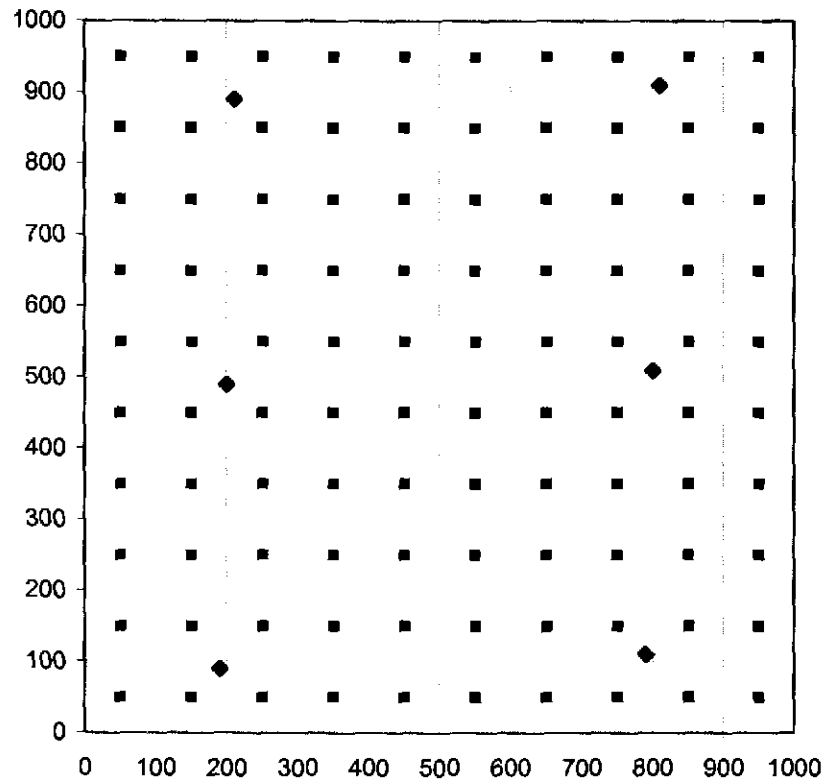


Figure 7. Locations of the six wells used in the test problem (diamonds) and the grid of calculated heads used to estimate the number of new triangles from the addition of a single new well at the center of each cell.

Results of the calculations made by the estimator program are contained in the *triangles.out* file. This file contains 100 lines and each line comprises the X and Y coordinates for the added well and the total number of triangles given the 6 original wells and the added well. Each of the criteria used to test this program are evaluated using the results in *triangles.out*.

- 1) For all points on the grid with a valid, not -999, head value, the addition program returns 35 triangles. Solution of (10) using $m=7$ and $n=3$ yields 35 triangles and therefore this criterion is met exactly.
- 2) There are 100 lines in the *triangles.out* file. Therefore, the addition program calculated the total number of estimators once and only once for each well added to the configuration.
- 3) Four locations in the input file *head_grid_data.txt* were assigned -999 as the head value. These four values define missing data in the NW region of the grid. The output file, *triangles.out*, shows the number of estimators for each of these locations to be -999. The program is able to read a missing data flag and return that flag for the locations with missing data.

- 4) Visual inspection of the *triangles.out* file and comparison with the X and Y coordinates of the grid in the *add_test.xls* file show that the addition program returns the correct coordinates for each well added to the monitoring configuration.

In summary, the estimator program produces results on the test problem that are correct for all four of test criteria identified prior to testing.

Appendix 10. Test Problem for Spatial Sensitivity Coefficients

The software to determine the spatial sensitivity coefficient as the Spearman rank correlation coefficient at every point in a model domain given a set of realizations of a spatially variable property is called **vlsap**. The **vlsap** program reads in a model output with one entry for every stochastic run of the model and a series of input files where each input is the realization of property values that created each single entry in the output file. **vlsap** then calculates the Spearman rank correlation coefficient between all outputs and all inputs for each spatial cell in the model.

The test problem for **vlsap** was built in an Excel spreadsheet: *sens_test_problem.xls*. This spreadsheet contains both the input for the test problem and the results from running the test problem. The test problem consists of a “domain” that is 1 cell wide and 100 cells long. In each cell is an integer between 1 and 100. There are a total of 100 realizations of these values for the domain. In the *sens_test_problem.xls* file, columns B through CW contain the different realizations. The test problem “model output” is the same as the cell number, 1 through 100, and these are stored in column A of the *sens_test_problem.xls* file. For any cell, the correlation between the model output and the values in the cell across all realizations is calculated and shown in column CY in the spreadsheet. For example, the correlation of cell 1 with the model output is calculated by comparing the values in column A with those in row 3. The resulting correlation is -1.00 . Because the values in the output and in the cells are from 1 to 100, they not only represent input and outputs measured in some arbitrary units, but they are also the direct ranks of the input and output data and therefore the correlation coefficient calculated in column CY is the Spearman rank correlation coefficient.

The test problem for the **vlsap** program was run on the Albuquerque linux cluster: lylin102 in the directory */h/wipp/sensitivity/steady-state/QAd/test/*. The **vlsap** executable and source code are located in */h/wipp/sensitivity/steady-state/QAd/source*. The values in the *sens_test_problem.xls* file were written to a text file *sens_test_problem.txt* and a bash shell was written to extract the output and the inputs in the different realizations into separate text files. The bash shell used for this extraction is *parseTestProblem.sh* and a listing of this shell is included at the end of this appendix. The results of running this shell are 100 files for each realization and each file contains the 100 values across the cells for that realization. These files are named *test.#.map* where the # is the realization number and the inputs to the **vlsap** program. The output, column A from the spreadsheet, is stored in the text file *test.res* and is the other input into **vlsap**.

The **vlsap** program is run using the bash shell: *runTestProblem.sh*. **vlsap** is executed and inputs and outputs are defined with a single command line statement as captured in the *runTestProblem.sh* file. The listing of the *runTestProblem.sh* file is given at the end of this appendix.

The single criterion for determining whether or not **vlsap** performs correctly is to compare the Spearman rank correlation coefficients calculated in column CY of the spreadsheet with those calculated by **vlsap**. The test problem was specifically designed to cover the entire range of

correlation coefficients from -1.0 to $+1.0$ depending on the cell in the model. This range of correlation coefficients was achieved by altering the order of the input values across the realizations. The **vlsap** output needs to match the results in column CY to the second decimal as this is all the resolution that would be used in mapping sensitivity within the Culebra.

The Spearman rank correlation coefficients calculated by **vlsap** are output to *test.map.out*. This file is then copied into column DI of the *sens_test_problem.xls* file and compared to the Excel results in column CY. The comparison results are shown in column DK. None of the 100 correlation coefficients calculated by **vlsap** deviates by more than 0.0005 from the Excel results indicating that **vlsap** has met the requirements for this test problem. The results of comparing the Excel correlation coefficients to those calculated by **vlsap** are shown in Figure 8.

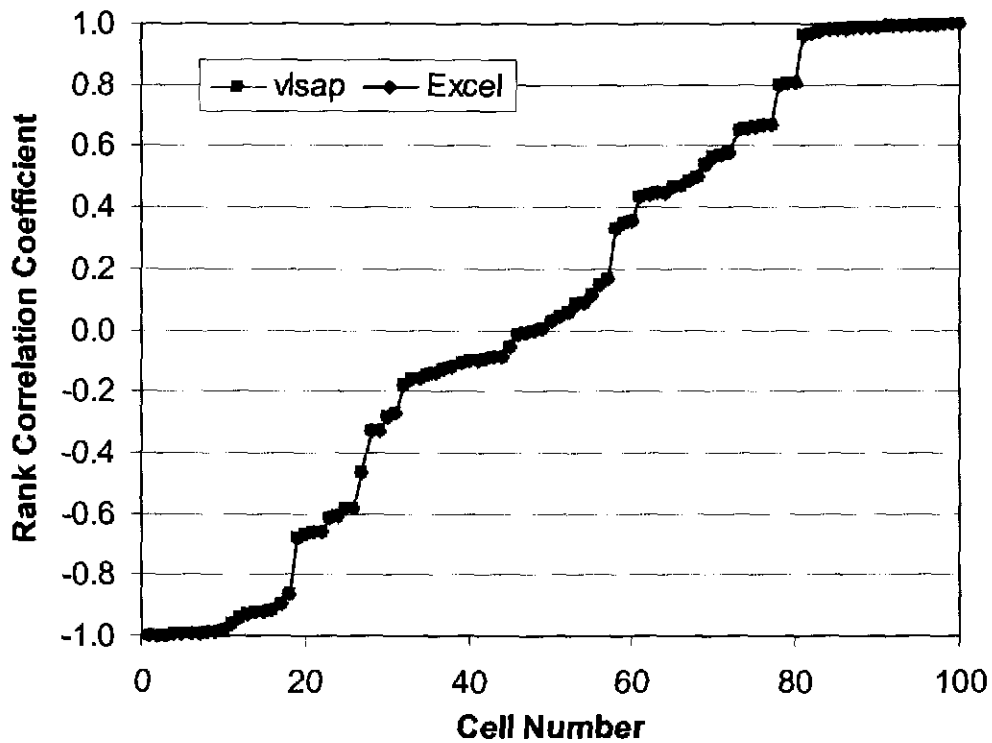


Figure 8. Comparison of Spearman rank correlation coefficients calculated by **vlsap** and Excel across all 100 cells in the test problem.

ParseTestProblem.sh shell file

```
#!/bin/bash -x

N=1
COL=2

while (( $N <= 100 ))
do
    tail -n 100 sens_test_problem.txt | awk "c=$COL { print \$c }" >
    test.$N.map
    COL=$((COL+1))
    N=$((N+1))
done

./runTestProblem.sh
```

RunTestProblem.sh shell file

```
#!/bin/bash

EXEC=/h/wipp/sensitivity/steady-state/QAd/source/vlsap

$EXEC -p test -x 1 -y 100 -r test.res -f 100 -o test.out.map
```